

Development of new storage phosphors for thermal neutron detection

Andrei Sidorenko

157
1963
11/11

TR 4318

**Development of new storage phosphors
for thermal neutron detection**



Development of new storage phosphors for thermal neutron detection

Proefschrift

ter verkrijging van de graad van doctor
aan de Technische Universiteit Delft,
op gezag van de Rector Magnificus prof.dr.ir. J.T. Fokkema,
voorzitter van het College voor Promoties,
in het openbaar te verdedigen

op maandag 1 november 2004 te 13:00 uur

door

Andrei SIDORENKO

Magister Fiziki
St.-Petersburg State Polytechnical University, Rusland
geboren te St.-Petersburg, Rusland



Dit proefschrift is goedgekeurd door de promotor:
Prof. dr. ir. C.W.E. van Eijk

Toegevoegd promotor: Dr. P. Dorenbos

Samenstelling promotiecommissie:

Rector Magnificus,	voorzitter
Prof. dr. ir. C.W.E. van Eijk,	Technische Universiteit Delft, promotor
Dr. P. Dorenbos,	Technische Universiteit Delft, toegevoegd promotor
Prof. P.A. Rodnyi,	St.-Petersburg State Polytechnical University, Russia
Prof. dr. A. Meijerink,	Universiteit Utrecht
Prof. dr. I.M. de Schepper,	Technische Universiteit Delft
Prof. dr. L.D.A. Siebbeles,	Technische Universiteit Delft
Dr. A.J.J. Bos,	Technische Universiteit Delft

Published and distributed by: DUP Science

DUP Science is an imprint of
Delft University Press
P.O. Box 98
2600 MG Delft
The Netherlands
Telephone: +31 15 27 85 678
Telefax: + 31 15 27 85 706
E-mail: info@library.tudelft.nl

ISBN 90-407-2540-3

Keywords: neutron storage phosphor / photostimulated luminescence / spectroscopy of rare-earth ions / radiation induced defects / thermoluminescence

Copyright © 2004 by A. Sidorenko

All rights reserved. No part of the material protected by this copyright notice may be reproduced or utilised in any form or by any means, electronic or mechanical, including photocopying, recording or by any information storage and retrieval system, without written permission from the publisher:

Delft University Press

Printed in the Netherlands

Contents

1	Introduction.....	1
2	Defining the characteristics of neutron storage phosphors and selection of materials.....	3
2.1	Known X-ray and neutron storage phosphors.....	3
2.2	Physical processes in scintillators and storage phosphors.....	5
2.2.1	<i>Interaction of ionising radiation with matter</i>	5
2.2.2	<i>Multiplication and thermalization of electron- hole pairs, energy transport to luminescence centre and electron/hole traps</i>	7
2.2.3	<i>Photostimulated luminescence</i>	8
2.3	Possible electron/hole traps. Examples of known storage phosphors.....	8
2.3.1	<i>Lattice defects in alkali-halides</i>	8
2.3.2	<i>Impurity ions</i>	10
2.3.3	<i>Lattice defects in borates</i>	13
2.4	Requirements for neutron storage phosphors.....	14
2.4.1	<i>Neutron absorption</i>	14
2.4.2	<i>γ-ray sensitivity</i>	15
2.4.3	<i>Stimuleability and spatial resolution</i>	16
2.4.4	<i>Detective quantum efficiency (DQE)</i>	17
2.4.5	<i>Fading</i>	19
2.5	Selection of materials.....	19
2.5.1	<i>Two approaches</i>	19
2.5.2	<i>Choice of compounds</i>	21
3	Experimental techniques.....	25
3.1	Introduction.....	25
3.2	Samples.....	25
3.3	Characterisation of spectroscopic properties.....	25
3.4	Characterisation of storage properties.....	26
3.4.1	<i>Thermally stimulated luminescence</i>	26
3.4.2	<i>Photostimulated luminescence (PSL)</i>	27
3.4.3	<i>Performance comparison of different storage phosphors</i>	29
3.5	EPR technique.....	31

4 Luminescence and Thermoluminescence of $Sr_2B_5O_9X:Ce^{3+},A^+$ ($X=Cl,Br, A=Na^+,K^+$) phosphors	33
4.1 Introduction.....	33
4.2 Materials.....	34
4.3 Results.....	34
4.3.1 <i>Optical properties of Ce^{3+} in $Sr_2B_5O_9Br$ and $Sr_2B_5O_9Cl$</i>	34
4.3.2 <i>EPR spectra of Ce^{3+} ions.....</i>	37
4.3.3 <i>Thermoluminescence</i>	39
4.3.4 <i>Emission spectra upon thermal stimulation</i>	41
4.4 Discussions.....	43
4.5 Conclusions.....	44
5 Complex study of radiation induced defects in $Sr_2B_5O_9Br:Ce^{3+}$ storage phosphor	47
5.1 Introduction.....	47
5.2 Results.....	47
5.2.1 <i>EPR measurements on irradiated pure $Sr_2B_5O_9Br$.....</i>	47
5.2.2 <i>Radiation induced optical absorption spectra of irradiated pure and Ce^{3+} doped $Sr_2B_5O_9Br$.....</i>	49
5.2.3 <i>Luminescence and TL of Eu, Yb and Sm doped $Sr_2B_5O_9Br$.....</i>	50
5.2.4 <i>Thermoluminescence after UV-illumination.....</i>	52
5.3 Discussions.....	53
5.3.1 <i>Room temperature stable defects and high temperature TL peak.....</i>	53
5.3.2 <i>Low temperature TL peak.....</i>	55
5.4 Conclusions.....	56
6 Storage properties of Ce^{3+} doped haloborate phosphors enriched with ^{10}B isotope	57
6.1 Introduction.....	57
6.2 Experimental procedures.....	57
6.2.1 <i>Standard TL and PSL read-out system</i>	58
6.2.2 <i>Read out with the commercial BAS scanner.....</i>	58
6.2.3 <i>Read out with the Risø-PSL single-grain reader</i>	58
6.3 Results.....	59
6.3.1 <i>TL and PSL study of haloborates with natural abundance of ^{10}B (18.8%)</i>	59
6.3.2 <i>TL and PSL study of haloborates with enriched abundance (99%) of ^{10}B isotope</i>	62
6.3.3 <i>Quantitative comparison of the studied haloborates (natural abundance of ^{10}B) with Gd-IP after cold neutron irradiation and read-out with the commercial BAS-scanner.....</i>	63
6.3.4 <i>Quantitative comparison of the studied haloborates with $BaFBr:Eu^{2+}xGd_2O_3$ after thermal neutron irradiation and read-out with the Risø-PSL single-grain reader.....</i>	64

6.4 Discussions.....	66
6.4.1 <i>The difference between S_n/S_γ (haloborates) and S_n/S_γ ($BaFBr:Eu^{2+}xGd_2O_3$)</i>	66
6.4.2 <i>Absorption of PSL light in the phosphor layer</i>	67
6.5 Conclusions.....	69
7 Spectroscopic and storage properties of $LiLnSiO_4:Ce^{3+},Sm^{3+}$	71
7.1 Introduction.....	71
7.2 Infrared Stimulable Phosphors (ISP).....	71
7.3 Synthesis of silicates.....	72
7.4 Spectroscopic properties of $LiLnSiO_4$ doped with rare-earth.....	73
7.4.1 <i>X-ray excited luminescence of $LiLnSiO_4:Ce,Sm, Ln=Y,Gd,La,Lu$</i>	73
7.4.2 <i>X-ray excited luminescence of $LiLnSiO_4, Ln=Y,Lu$ doped with Ce^{3+} and Eu^{3+}</i>	75
7.4.3 <i>Excitation spectra of Ce^{3+} in $LiLnSiO_4, Ln=Y,Lu$</i>	75
7.4.4 <i>Excitation spectra of Eu^{3+} in $LiLnSiO_4, Ln=Y,Lu$</i>	77
7.4.5 <i>Excitation spectra of Sm^{3+} in $LiLnSiO_4, Ln=Y,Lu$</i>	78
7.5 Thermoluminescence of $LiLnSiO_4, Ln=Y, Lu$ doped with rare-earth.....	79
7.5.1 <i>Thermoluminescence of $LiLuSiO_4:Ce^{3+}, Tb^{3+}$ or Sm^{3+}</i>	79
7.5.2 <i>Trap-filling spectrum of $LiLuSiO_4:1\%Ce^{3+}$</i>	81
7.6 Photostimulated luminescence of $LiLuSiO_4:Ce^{3+},Sm^{3+}$ and $LiYSiO_4:Ce^{3+},Sm^{3+}$	83
7.6.1 <i>PSL stimulation spectra of $LiLuSiO_4:Ce^{3+},Sm^{3+}$ and $LiYSiO_4:Ce^{3+},Sm^{3+}$</i>	83
7.6.2 <i>PSL of $LiLuSiO_4:Ce^{3+},Sm^{3+}$ and $LiYSiO_4:Ce^{3+},Sm^{3+}$</i>	83
7.7 Discussions.....	85
7.8 Remarks.....	90
7.9 Quantitative comparison with commercial storage phosphors.....	90
7.10 Conclusions.....	92
Concluding remarks	95
Summary	97
Samenvatting	101
List of publications	105
Curriculum vitae	107
Acknowledgements	109



1 Introduction

The use of thermal neutrons in crystallography started in 1947 [1]. Since that time position sensitive detectors for thermal neutrons became of increasing importance for various applications such as small angle scattering, neutron reflection and diffraction studies as well as radiography and tomography.

In the last decades a new type of a position sensitive detector, which is based on photo stimulated luminescence (PSL) in a phosphor (or storage phosphor) was developed. Today Image Plates (IP) containing PSL phosphors are widely used for X-ray imaging. However, the use of IPs for thermal neutron detection has just started.

An Image Plate is a flexible image sensor in which a thin layer of very small crystals (grain size about 3 μm) of photo stimuable phosphor is uniformly coated on a polyester support film. The composite structure of the IP is shown in Figure 1.1.

The functional principle of the detector, based on IP is as follows: during irradiation particles (γ -ray quanta, neutrons) are absorbed in the active layer of the IP, which consists of storage phosphor material mixed with organic binder material. Secondary particles transfer their energy primarily by ionisation, thus generating electron-hole pairs. Contrary to scintillators, where the energy of electron-hole pairs is promptly transferred to luminescence centres, in storage phosphors part of the electrons and holes are trapped. Thus, the profile of irradiation is formed by the spatial pattern of filled electron and hole traps. Next, a read out procedure takes place, in which the IP is optically stimulated pixel-by-pixel employing a focused laser beam. During stimulation the trapped electrons and/or holes transfer their energy to luminescence centres followed by light emission. Emitted photons are detected by a photomultiplier (PMT) and the signal is proportional to the amount of radiation absorbed in that pixel. Thus, a complete profile of irradiation can be reconstructed.

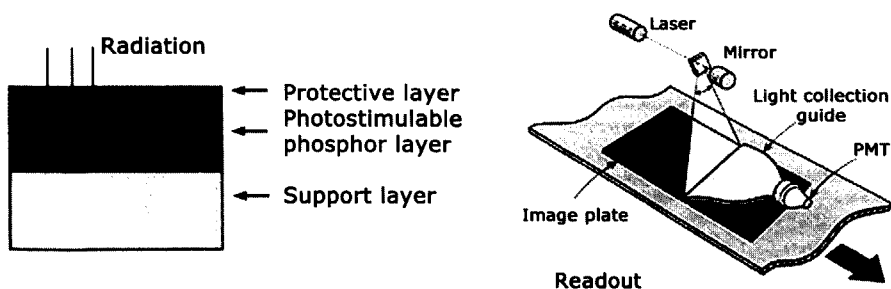


Figure 1.1: Cross section of an IP and schematic of a read out setup.

For clarity let us consider a type of experimental setup for thermal neutron application. In Figure 1.2 a schematic view of the setup for neutron crystallography is shown. The small sample is placed in the centre of a drum, which is covered by a neutron IP. The neutron beam from a nuclear reactor is directed to the sample and scattered neutrons are absorbed in the IP. The duration of an experiment usually is about 24 hours, which is caused by the low neutron flux (typically 10^6 n/cm²/s on the sample) and small neutron scattering cross-section of the sample. When the irradiation is finished, the drum starts to rotate and by moving the stimulating laser beam parallel to the central axis along the drum, the PSL can be detected by the PMT and information can be read-out. Thus a diffraction pattern can be obtained.

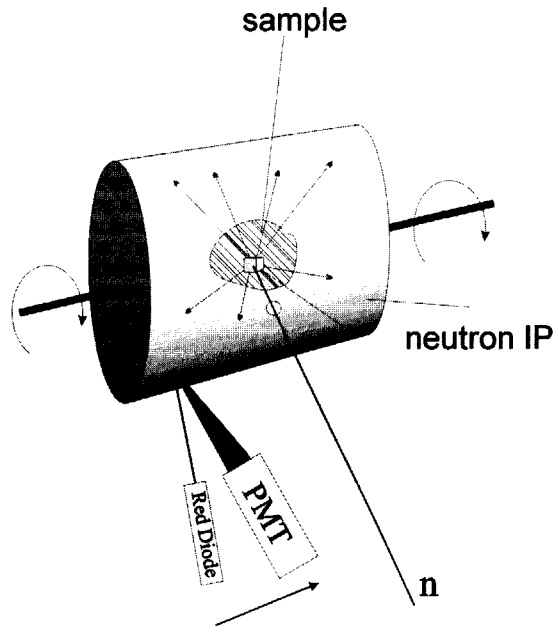


Figure 1.2: Sketch of the setup for neutron crystallography

Since the system is operated at a nuclear reactor, the neutron IP must be sensitive to γ -rays as low as possible, as these can deteriorate the image quality. In order to reduce the influence of γ -ray background the system is often placed far from the nuclear reactor, which leads to reduction of the neutron flux and consequently an increase of the duration of the experiment. Available neutron IPs from FujiFilm have a large atomic number, which makes them very sensitive to γ -rays!

The aim of this research is to develop a new neutron IP with better (lower) γ -ray sensitivity than used nowadays. This will increase the variety of applications of thermal neutrons and neutron IPs.

[1] Zinn W. H., Phys. Rev. 71 (1947) 752–757

2 Defining the characteristics of neutron storage phosphors and selection of materials

2.1 Known X-ray and neutron storage phosphors

To determine the performance of an X-ray storage phosphor a read-out experiment must be performed (Figure 2.1). After irradiation at room temperature a sample is stimulated continuously with an appropriate stimulation light source. A PMT detects the resulting PSL versus time. Continuous photostimulation leads to a decrease of the number of PSL-active centres. Consequently, the PSL intensity decays under continuing stimulation. The area below the PSL curve is proportional to the absorbed irradiation dose. In a commercial system a laser beam is used to read out the information stored in the phosphor screen point by point and line by line. The information should be read-out in the shortest time possible. To describe the characteristics of a storage phosphor the quantities “conversion efficiency” (CE) and “stimulation energy” (SE) are introduced. CE is defined as the PSL light yield per absorbed dose in [$\text{pJ}\cdot\text{mm}^{-2}\cdot\text{mR}^{-1}$]. The stimulation energy (SE) is defined, as the energy required for reduction of the PSL intensity to 1/e of its initial value in unit area of the IP [$\mu\text{J}\cdot\text{mm}^{-2}$].

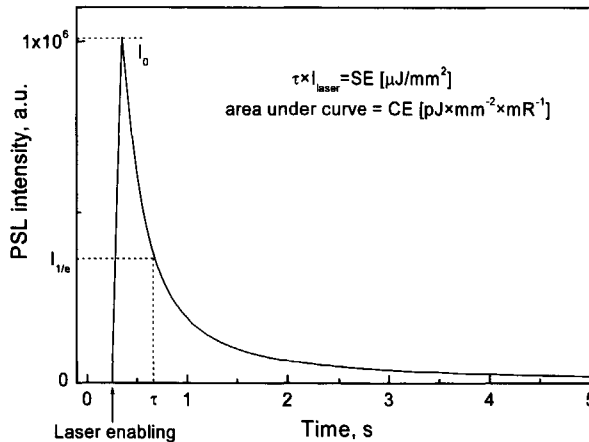


Figure 2.1: A PSL decay curve of an X-ray storage phosphor $\text{BaFBr}:\text{Eu}^{2+}$ under continued stimulation with 550 nm photons. I_{laser} is the power delivered by the laser per unit time.

The sensitivity of an X-ray storage phosphor is proportional to the stored energy and inversely proportional to the energy required for the read-out. Therefore, the sensitivity is given by the ratio CE/SE.

The same considerations can be applied to neutron storage phosphors. An additional parameter, which must be taken into account, is the γ -ray sensitivity. Due to the broad energy range of γ -rays in a background the quality " γ -ray sensitivity" can not be expressed in a single value. This will be discussed in [2.4.2].

The best X-ray storage phosphor known so far is BaFBr doped with Eu^{2+} as activator [1]. The family of phosphors $\text{Ba}_{1-x-y}\text{Ca}_x\text{Sr}_y\text{FH}:\text{Eu}^{2+}$ where H can be any of the halogens Cl, Br or I (or an arbitrary mixture of them) has been extensively studied. Each company, like Fuji, Konica and Agfa utilises a slightly different modification of this phosphor in their commercial systems. In spite of many works dedicated to the mechanisms of the information storage and the read-out process in this phosphor, no complete understanding has been achieved.

Other known storage phosphors are based on alkali halides doped with ns^2 (mercury like) ions. RbBr:TI⁺ phosphor, has in principle, very good storage properties. However the stored image fades away at room temperature within seconds, so a very fast read out process has to be initiated immediately after irradiation. Konica has used this material in integrated readers of computed radiography, where IP can be rapidly read out *in situ* immediately after the termination of exposure. Another interesting phosphor, is an elpasolite $\text{Cs}_2\text{NaYF}_6:\text{Ce}^{3+}$ [2].

The performances of known X-ray storage phosphors in comparison with the standard BaFBr:Eu²⁺ is given in Table 2.1. Additionally, some information is presented on conventional X-ray phosphors, i.e. those used in screen-film combinations.

Concerning the commercial neutron storage phosphors, they are based on a mixture of X-ray storage phosphor material with a neutron converter, like $^{157}\text{Gd}_2\text{O}_3$ or ^6LiF . Their properties will be discussed in [2.5.1].

Table 2.1: Physical properties of storage phosphors after [2-4]. Z is the effective atomic number of a compound. CE and SE values are given for specific stimulation wavelength of 680 nm. In the last column values for Light Yield are given in photons/ 50 keV. For conventional phosphors this is the direct light emitted and for storage phosphors it is CE.

Phosphor	Z_{eff}	CE ($\text{pJ}\cdot\text{mm}^{-2}\cdot\text{mR}^{-1}$)	SE ($\mu\text{J}\cdot\text{mm}^{-2}$)	CE/SE (10^3R^{-1})	Optimal Stimulation (nm)	LY (photons/ 50 keV)
BaFBr:Eu ²⁺	56	14.4	28.0	0.51	550	140
RbBr:In ⁺	37	1.9	25.0	0.077	700	-
RbBr:Ga ⁺	37	5.6	3.9	1.47	705	-
CsBr:In ⁺	55	3.0	23.0	0.140	700	-
CsBr:Ga ⁺	55	5.4	4.3	1.37	685	-
$\text{Cs}_2\text{NaYF}_6:\text{Ce}^{3+}$		4.3	115	0.038	550	-
CsI:TI ⁺	55					2500
$\text{Gd}_2\text{O}_2\text{S}:\text{Tb}^{3+}$	64					2500

2.2 Physical processes in scintillators and storage phosphors

There are several similarities between storage phosphors and scintillators. Scintillation and PSL processes can be represented as a sequence of the following stages [5]:

1. *In scintillators and storage phosphors*: absorption of the ionising radiation (X-rays, γ -rays, electrons or heavy charge particles), production of secondary particles and their absorption, creation of energetic primary electrons and holes.
2. *In scintillators and storage phosphors*: production of numerous secondary electrons and holes, and their subsequent thermalization resulting in a number of e-h pairs with energies roughly equal to the band-gap energy.
3. *In scintillators*: energy transfer from electron-hole pairs to the luminescent centres
4. *In storage phosphors*: partly energy transfer from electron-hole pairs to the luminescent centres and partly trapping of e-h pairs by defects, either induced during irradiation or contained in the material prior to irradiation.
5. *In scintillators and storage phosphors*: radiation emission by luminescence centres
6. *Only in storage phosphors*: photostimulation of trapped electrons and/or holes with further recombination with luminescence centres, resulting in PSL.

Let us consider all the stages more in details.

2.2.1 Interaction of ionising radiation with matter

Absorption of X-rays and γ -rays

For photon energies of 50 keV – 10 MeV there are three main processes through which γ -rays transfer their energy: *photoelectric* absorption, *Compton* absorption and *pair production* [6].

The *photoelectric* process is the predominant mode of interaction for X-rays and γ -rays of relatively low energy. The process is enhanced for absorber materials of relatively high atomic number Z . No single analytical expression is valid for the cross-section σ of photoelectric absorption per atom over all ranges of E_γ and Z , but a rough approximation is $\sigma \sim Z^n / E_\gamma^{3.5}$, where n varies between 4 and 5 over the γ -ray energy region of interest.

The probability of *Compton scattering* depends on the number of electrons available as scattering targets and therefore increases linearly with Z . The dependence on γ -ray energy can be estimated as $E_\gamma^{-0.5}$, i.e. probability falls down with the increase of energy. Obviously, the photoelectric effect is very important for absorbing Compton scattered photons.

If the γ -ray energy exceeds 1.02 MeV the process of *pair production* can occur. The magnitude of this process varies approximately as the square of the atomic number and rises sharply with E_γ .

The energy dependence of the γ -ray interaction processes in $\text{Ca}_2\text{B}_5\text{O}_9\text{Cl}$ and $\text{BaFBr} \times \text{Gd}_2\text{O}_3$ is shown in Figure 2.2. Often only the photoelectric effect is counted for as the main interaction mechanism. In this case Z_{eff} is used as a measure of X-ray and γ -ray sensitivity, defined by $Z_{\text{eff}} = \sqrt[4]{\sum_i W_i Z_i^4}$, where W_i is the weight fraction and Z_i is the atomic

number of element i in a compound. However, as it is seen in Figure 2.2 for the compound with low atomic number, the Compton effect is dominating over the whole energy range of

interest. It is also seen from Figure 2.2 that for γ -ray energies higher than 800 keV there is no difference in γ -ray sensitivity between high Z BaFBr \times Gd₂O₃ and low Z Ca₂B₅O₉Cl. Thus, the statement "Because of high γ -ray background neutron storage phosphors with low Z are needed" is not completely true, if the energy spectrum of the γ -ray background is not known. This will be discussed more in details in [2.4.2].

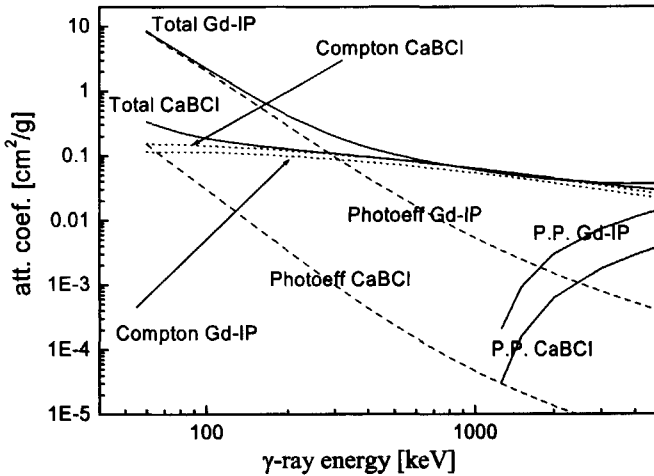


Figure 2.2: The linear photon attenuation coefficient μ as a function of the γ -ray energy for Gd-IP, containing BaFBr:Eu²⁺ and Gd₂O₃ with molar ratio 1:1, and Ca₂B₅O₉Cl, noted as CaBCl. The total attenuation coefficient is summed up out of photoelectric process (Photoeff), Compton and pair production (P.P.).

Neutron absorption

Neutron absorption in matter is controlled by the neutron absorption cross-section of the elements. In Table 2.2 cross-sections are listed of several isotopes which can be used for the conversion of thermal neutron radiation into different types of secondary radiation. With the decrease of neutron energy the cross sections increase. The types of secondary particles and the released energy are different for each converter. In the neutron reaction of ⁶Li and ¹⁰B two particles are emitted into opposite directions because of the conservation of momentum, while after neutron capture by Gd - conversion electrons and γ -rays are emitted and different cascades of deexcitation of the excited Gd nuclei are possible [7-8]. The absorbed energy from γ - rays and conversion electrons can differ in each Gd decay.

Table 2.2: The neutron captures reaction cross sections at a neutron energy 25 meV (1.8 Å).

Reaction	Secondary radiation (MeV)	Cross section (barn)	Natural abundance
${}^6\text{Li} + {}^1_0\text{n}$	$\rightarrow \alpha(2.05) + {}^3\text{H}(2.74)$	940	7.5%
${}^{10}\text{B} + {}^1_0\text{n}$	$\rightarrow \alpha + {}^7\text{Li} + 2.78 \text{ MeV (7\%)}$	3837	18.8%
	$\rightarrow \alpha + {}^7\text{Li}^* + 2.3 \text{ MeV (93\%)}$		
	↓ $\alpha + {}^7\text{Li} + \gamma (0.48 \text{ MeV})$		
${}^{\text{nat}}\text{Gd}$	Conversion electron (0.03→0.2 MeV), γ -rays (up to 7.5 MeV)	48890	100%

Interaction of the secondary particles with matter

After neutron capture the secondary particles, i.e. electrons and heavy charged particles, in their passage through matter dissipate their kinetic energy by excitation and ionisation of atoms. The mean ionisation loss of a charged particle is determined by the well-known Bethe-Bloch formula [6]. The energy loss per unit length of a heavy charged particle track is much greater than the ionisation loss of electrons with the same energy. Therefore a heavy charged particle creates a high-density ionisation track. It is well known that the light output of a scintillator depends not only on the input energy but also on the ionisation density. The light output of a scintillator from a heavy particle will be less than from an electron of the same energy. The measure of the difference depends strongly on the material [5].

2.2.2 *Multiplication and thermalization of electron-hole pairs, energy transport to luminescence centre and electron/hole traps*

After absorption of ionising radiation, the created high-energy primary electrons and holes generate secondary electrons and holes and so on. This avalanche continues until electrons and holes are not able to produce further ionisation. The excess of the energy is lost by thermalization. The reviewed and discussed theories of this process can be found in [9]. The time scale of thermalization is believed to be in the order of few picoseconds.

After thermalization, the electrons and holes must transfer their energy to the luminescence centres. A direct electron-hole capture by luminescence centres is possible, and it is called recombination luminescence. Also the electrons and holes may form excitons. These excitons can transfer their energy to a luminescence centre, however this process is less probable than recombination luminescence [9].

Various defects and impurities in a lattice can play the role of electron/hole trap. For example, anion vacancies in ionic crystals act as effective capture centres of free electrons. An anion vacancy captured electron is a stable electronic defect, an F-centre.

In materials with mainly ionic bonding, valence holes can be localised at distinct anions. The polarisation of the environment can result in sharing of this hole between the two neighbouring halide anions forming X_2^{2-} , known as V_k centre [10]. This V_k centre is mobile and can be involved in recombination with luminescence centres. Also a V_k centre can capture a free electron forming an excited $(X_2^{2-})^*$ molecule or self-trapped exciton (STE), which can emit a photon with a decay time of about 1 μ s.

It was suggested in [11,12] that non-radiative annihilation or dissociation of an STE can form a pair of F and H ($(X)_2^-$ molecules occupying single halide sites) centres. After creation of an unstable F-H pair, the H centre, which is mobile at room temperature, can migrate towards or away from the F-centre. Thus one can expect immediate F-H recombination or creation of stable separated F and H defects. To be stable at room temperature it is important for a hole trap centre to avoid recombination with an F-centre. The latter depends strongly on the matrix, as will be shown in [2.3.1].

2.2.3 Photostimulated luminescence

For the most known storage phosphors the laser wavelength, used for stimulation of trapped carries, is separated from the emission spectrum of PSL, located at shorter wavelength. For example, in BaFBr:Eu²⁺ the Eu²⁺ emission locates at 390 nm, while stimulation of trapped charges created after the irradiation is most efficient at about 600 nm. After the read-out and optical bleaching procedure the image profile is erased and experiments can start over.

In [13] the reverse situation was reported for NaCl (Me) and LiF (Me) substances. After irradiation, the PSL with emission wavelength at 530-560 nm must be stimulated with 365 nm photons. The image profile can not be erased optically, but only by heating for 0.5 h at 400 °C. Obviously, such storage phosphor would be very difficult to apply in any experimental setup.

Therefore, the optimal luminescence centre in a storage phosphor must have a high quantum yield, have an emission in the 300-400 nm region for better stimulation – emission wavelength separation and have a decay time constant not longer than several microseconds [2.4.3]. Depending on the matrix ns² ions, like Tl⁺, In⁺, Bi³⁺ or lanthanides, like Ce³⁺ or Eu²⁺ can be used.

2.3 Possible electron/hole traps. Examples of known storage phosphors

2.3.1 Lattice defects in alkali-halides

There is a general agreement that ionising radiation generates F-centres as stable electron traps. It is the simplest and most studied centre in alkali-halides, consisting of one electron trapped at a halide vacancy [14]. The F-centre is paramagnetic, therefore its structure can be studied by EPR and double-resonance techniques. In addition, F-centres exhibit characteristic absorption and luminescence bands. Both bands correspond to transitions between the ground 1s and the first excited 2p states. Replacement of a halogen ion by an electron in the site

suggests that there is a strong localisation of the electron density within the vacancy and thus the F-centre is a close analogy of an electron in a box. Then for the trapped electron the main absorption band energy corresponds to an excitation from 1s to 2p, defined as $E = 3\pi^2 \hbar^2 / 2ma^2$, where a is the width of the potential well. Thus the position of the absorption band depends mostly on the spatial size of the halogen site and varies between 5.1 eV for LiF and 1.71 eV for RbI.

In BaFBr, which has the maltockite structure [15], the creation of two types of F centres is possible: F(Br⁻) and F(F⁻) centres. In order to create an F-centre with electron-hole pairs a halide vacancy needs to be present in the crystal before irradiation or it must be generated during the irradiation. Let us consider as an example two types of BaFBr:Eu²⁺ storage phosphors, noted as stoichiometric and non-stoichiometric BaFBr (BaF_{1.1}Br_{0.9}). For both of them the PSL active electron trap centres are F(Br⁻) and F(F⁻) centres [16,17].

In stoichiometric BaFBr three different types of unavoidable oxygen impurities were assigned to O_F²⁻, O_{Br}²⁻ and molecular O₂²⁻ on unknown site, though the number of O_F²⁻ centres is dominating [18-20]. For charge compensation an anion vacancy is needed. It was shown in [21] that these vacancies are Br⁻ centres. The generation of F(Br⁻) centres in oxygen-contaminated BaFBr can be considered as:

$V_{Br}^- + O_F^{2-} \xrightarrow{UV, X\text{-ray}} F(Br^-) + V_K(Br_2^-) + O_F^{2-} \xrightarrow{>120K} F(Br^-) + O_F^-$ [22]. Therefore the generation of F(Br⁻) centres is impurity limited, and the number of F(Br⁻) centres is saturating at high irradiation doses. The mechanism leading to F(F⁻) generation remains unclear [22].

The role of O_F²⁻ centres in stoichiometric BaFBr is certainly that they capture holes and form O_F⁻ [19,20,22]. However it is still not known whether they are active in the PSL process [1].

No oxygen impurities have been found in non-stoichiometric BaFBr [17]. It was shown [17] that in non-stoichiometric BaFBr, 10% fluorine "anti-sites" (fluorine ion on a bromine site) are present. The F(Br⁻) centres generation occurs via F-H process between the fluorine and bromine⁻ sublattices, according to the reaction $F_{Br} \xrightarrow{X\text{-ray}} F(Br^-) + F_{2,F}^-$, i.e. an electron trap centre is formed in the Br⁻ sublattice and the room temperature stable H centre is formed in the F⁻ sublattice [17]. Apparently in a non-stoichiometric BaFBr very few F(F⁻) are generated in comparison to F(Br⁻) centres. No F-H processes within one sublattice were observed. This is in agreement with results on stoichiometric BaFBr, where no H centres have been found.

It is not possible to investigate F(Br⁻) and H centres in non-stoichiometric BaFBr:Eu²⁺ by EPR due to the very high signal from Eu²⁺ [17]. Thus it is not known whether H centres are the hole trapping centres active in the PSL process.

In alkali-halide storage phosphors, like KBr:In⁺ and RbI:Tl⁺, F centres, which are stable at room temperature, are generated probably via electron capture by existing Br⁻ vacancies [23]. All F centres generated via F-H pairs recombine above 70 K.

Together with stable electron trapping centres there must exist stable hole trapping centres. However no hole trapping centres belonging to the lattice defects, which are stable at room temperature (apart from O_F²⁻ in stoichiometric BaFBr) have been found in alkali-halides. Therefore impurity ions must play the role of hole trapping centres.

2.3.2 Impurity ions

ns² type ions

It is well known that some activators, used in scintillators can co-exist in different valence states. The ion tendency to capture a hole or an electron depends on the energy position of the ground state relative to the host bands.

A good example is the Tl^+ ion in NaI. According to the theoretical calculations performed in [24], the ground state of the Tl^+ ion is located in the forbidden gap. It can trap an electron or a hole created by ionising radiation as well as a relaxed hole (V_k centre) or electron released from a trap. EPR and optical absorption techniques can detect Tl^{2+} and Tl^0 centres [25-27].

Stability (or lifetime) of Tl^0 centres is determined by the position of the ground state relative to the conduction band and the mobility of V_k hole centres (mobile holes). In other words the additional electron in a Tl^0 centre can be thermally activated to the conduction band or Tl^0 can recombine with a mobile hole (V_k centre).

As an example, let us consider the RbI: Tl^+ storage phosphor. After X-ray irradiation at liquid nitrogen temperature F, V_k and Tl^0 centres are generated, and only few Tl^{2+} centres are directly formed [28]. Upon annealing to 150 K V_k centres become mobile [29], they recombine with Tl^+ centres and the number of Tl^{2+} centres increases [28]. At 180 K Tl^0 centres become unstable and the released electrons are captured by the Tl^{2+} centres. Consequently, almost 95% of the Tl^{2+} centres disappear at 220 K [28]. Therefore only the residual number of Tl^{2+} centres plays a role as PSL active hole trapping centres.

The storage and read-out processes of known perspective alkali-halides doped with ns^2 type ions, like KBr:In⁺, RbI:Tl⁺, RbBr:Ga⁺ and CsBr:Ga⁺ can be explained by simple pair mechanisms: upon X-irradiation F centres are generated as electron traps and the activator itself as a complementary hole trap [1].

An interesting feature was observed in Ga⁺ doped materials [30,31]. Two different types of Ga^{2+} hole trap centres were observed: $(Ga^{2+})^I$ and $(Ga^{2+})^{II}$ centres. Type I is an isolated Ga^{2+} ion on a Rb⁺ or Cs⁺ site, whereas type II is a complex of Ga^{2+} on a Rb⁺ or Cs⁺ site and a nearest neighbouring cation vacancy. Only $(Ga^{2+})^I$ centres take part in the PSL process. It is explained by the lower Coulomb attraction of electrons by neutral, charged compensated $(Ga^{2+})^{II}$ centres. A similar feature has been observed in Ce³⁺ doped haloborates [5.3.2].

Lanthanide activators

The main valence state of a lanthanide activator in an ionic compound is determined by the valence of the replaced cation and the synthesis conditions (firing atmosphere). The rare-earth ions are stabilised usually in trivalent state when they replace trivalent cations. However, such ions like Ce or Tb can be easily converted to the stable tetravalent state (for example by irradiation).

As was already mentioned that an ion tendency to capture a hole or an electron, i.e. to become stabilised in a different valence state, depends on the energy position of its ground state. The prediction of the absolute energy position of the ground states of rare earth ions relative to the valence band is not possible up to now. However, there are several sets of works on lanthanides, which in combination partly can answer this question.

The empirical model for determination of 4f electron energies relative to the host bands has been proposed in [32]. It is based on results of resonant photoemission of lanthanides. Using this technique the binding energies of 4f electrons in lanthanides in gallium and

aluminum garnets relative to the valence band maximum were determined (Figure 2.3). The staircase pattern of binding energies through lanthanides remains the same in gallium and aluminum garnets. The only difference is the shift of the whole pattern in aluminum garnet towards lower binding energies. It was considered [32] that due to the chemical similarity of the lanthanide ions and the non-bonding character of 4f electrons, the *net shift* of binding energy is similar for all lanthanide ions in a particular material. The lattice potential raises the energy of electrons, resulting in a corresponding decrease in their binding energy. Thus the staircase character in lanthanide series remains the same for all the materials, however the whole curve will be shifted down- or upwards, depending on the material. In another terminology, it is possible to say that the maximum of the valence band is shifted to lower or higher binding energy, depending on the compound [32].

It is clearly seen from Figure 2.3 that the binding energy for Ce^{3+} and Tb^{3+} is negative relative to the position of the valence band maximum in gallium and aluminum garnets. The valence state of these ions in as-grown material will be determined by the synthesis conditions (firing atmosphere). Thus Ce^{3+} and Tb^{3+} are the easiest ions to be converted to the tetravalent states. Pr and Dy can also be stabilised in tetravalent state in some materials, however this state will be less stable than in case of Ce and Tb. From Figure 2.3 it is also clearly seen that the binding energy of 4f electrons in Sm, Eu, Gd and Yb is so high, that it would be very difficult to make them stable in 4+ state. Indeed, no data in literature can be found on Sm, Eu, Gd or Yb in tetravalent states.

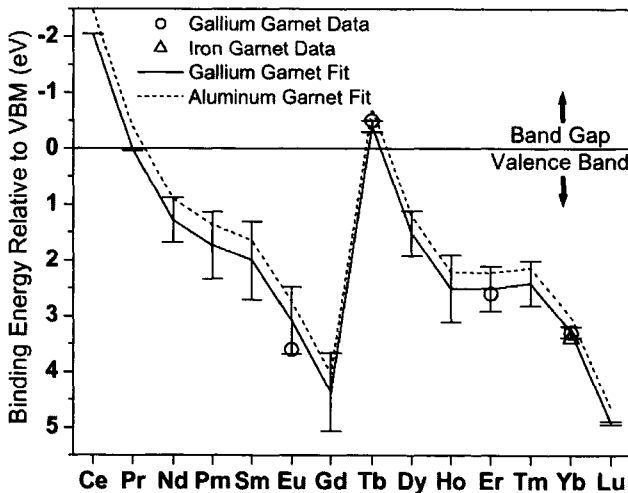


Figure 2.3: (from [32]): Systematic behaviour of 4f binding energies relative to the valence band maximum (VBM) in garnets. Circles represent measured binding energies relative to the VBM (at 8.3 eV) for 4f electrons in gallium garnets; negative binding energies are within the band gap and positive binding energies are below the VBM. The solid line is the fit of the two-parameter model [32] to the experimental data and error bars represent the uncertainty in the values of the free-ion ionisation potentials. The dotted line is the fit of the model to 4f binding energies in the aluminium garnets.

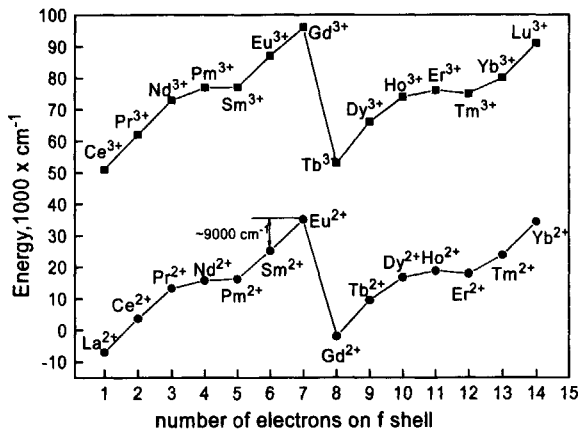


Figure 2.4: $f \rightarrow d$ transition energies for the free tri- and di-valent lanthanides, taken from [34].

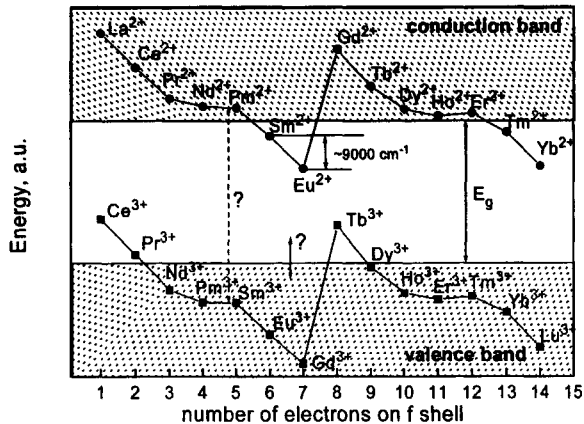


Figure 2.5: Schematic representation of $4f$ ground state energy positions of lanthanides relative to the valence and conduction band. The net shift between the two curves is not known, since the effect of the lattice potential on $5d$ electrons in the di- and tri-valence state can be different. The absolute position of the $4f$ ground state relative to the valence band is known only for gallium and aluminium garnet [32]. For other compounds this value can vary.

From Figure 2.3 it is not possible to estimate the stability of lanthanides in divalent states. The staircase pattern of $4f$ binding energy shown in Figure 2.3 is very similar to the

pattern of $f \rightarrow d$ transition energies of free tri- and divalent lanthanides, predicted by Dorenbos in [34] and Brewer in [35] (Figure 2.4). The patterns in Figures 2.3 and 2.4 appear to be mirror-reflected along a horizontal line. Such a behaviour can bring to the conclusion that for a particular valence state in a particular material 5d levels are located at the same energy relatively to valence band for all lanthanide ions, with the error corresponding to the uncertainty of the free-ion potential determination (Figure 2.3). Thus, aligning the 5d energies of all lanthanide ions in a particular material, one can get the positions of ground state energies of tri- and divalent lanthanides relatively to each other (Figure 2.5). A ground state energy position determined in such a way is not an absolute value relative to the valence band maximum, as it can be shifted down- or upwards depending on the material. Also the clearance between two patterns for tri- and -divalent lanthanides is not known, since the difference in the effect of the lattice potential on 5d levels in case of tri- and divalent states remains unknown. Therefore, it is not possible to predict for a particular compound, whether "abnormal" valent states of a lanthanide ion will be stable.

In spite of the number of uncertainties several important conclusions can be made from Figures 2.3 and 2.5:

- Ce^{3+} and Tb^{3+} are the best candidates for hole trapping centres. When these ions are used as activators and replace a trivalent cation there is a large probability that the ground states of these levels will be located above valence band.
- Dy^{3+} and Pr^{3+} are also possible candidates for hole trapping centres, however it is more likely that the ground states of these lanthanides are located in the valence band (or very close to it).
- It can be seen from Figure 2.5 that Eu, Sm, Tm and Yb ions are the best candidates for electron trapping centres, since there is a high probability that the ground states of these divalent lanthanides will not be located in conduction band.
- In a matrix, where Ce or Tb can become stable in the four-valent state and Eu, Sm, Tm or Yb in di-valent state the double co-doping with these lanthanides can provide hole and electron traps respectively.

It was shown recently in [36] that the ground state of divalent lanthanides could be predicted with an accuracy of about 0.5 eV from the position of the charge transfer band. The more detailed discussion of this point will be presented in Chapter 7.

2.3.3 Lattice defects in borates

About 65% of the known borate compounds have crystallochemical structures characterised by BO_3 triangles, which are either isolated or joint with each other [37]. These anionic units form ionic bonds with metal cations. Such structures are typical for ortho-, pyro-, and methaborates. About 50 % of borate compounds exhibit a crystal structure including polyanions (B_nO_m). In polyborates, the triangles are joined both with each other and with tetrahedrons by a common oxygen atom. In the latter case, the number of possible combinations is very large.

A number of works were dedicated to the investigation of radiation damage in boron glasses [38-43]. Boron is frequently placed in tetrahedral co-ordination in complex oxide glasses, although it also occurs in planar triangular units. The most commonly observed defect in irradiated complex oxide glasses is a boron-oxygen hole centre (BOHC). These defects are stable at 400-500 K [38]. Griscom suggested [38] that BOHC represents a hole on

the oxygen bridging between a three-coordinated boron and four-coordinated boron. This suggestion was argued in [43], where EPR results suggested that all variants of BOHC are holes trapped on the non-bridging oxygen in a BO_3^- unit. If the hypothesis of Griscom is true in haloborates the formation of BOHC centres is very likely, since jointed BO_3 and BO_4 groups form the polyanion (B_5O_9).

As an example, in pure LiB_3O_5 crystal after irradiation the defect associated with the oxygen hole trapping centre was observed [44]. The model suggests that non-paired spin is localised on the π_z -level of oxygen, which bridges two boron ions, one three-coordinated and another four-coordinated, with substantial delocalisation into the p_z orbital of the trigonal boron.

Oxygen vacancies also can play a role of electron trapping defects. For example in crystalline $\text{Zn}_4\text{B}_6\text{O}_{13}$ a room temperature stable radiation induced defect, associated with an electron trapped on an oxygen vacancy, belonging to the borate group has been found [45].

The electron trapping centres like a boron-electron centre (BEC), which is probably an electron trapped on an overcoordinated oxygen (O_3^+ defect) [43], and alkali-electron centres (AEC) are less characterised.

The real nature of these defects is still argued. The presence of each type of defect in borate phosphors seems to be dependent on the type of crystallochemical structure. EPR techniques can serve as a probe for identification of paramagnetic defects.

2.4 Requirements for neutron storage phosphors

2.4.1 Neutron absorption

The neutron capture cross-section of a neutron converter and the molar ratio of a neutron converter in a phosphor determine the neutron absorption efficiency of the storage phosphor. *Not only the probability of the neutron to be absorbed in the phosphor layer, but also the spatial distribution of absorbed neutrons is of main importance in a storage phosphor, because of their polycrystalline nature.* In contrast to crystals, the stimulation laser photons as well as PSL photons suffer from the number of scatterings from the surface of phosphor grains [46]. If the phosphor represents even a very low-absorbing substrate for stimulation or emitted light, the probability for a photon to be absorbed is much higher than in a crystal. *Thus the neutron absorption efficiency of a storage phosphor must be as high as possible to generate PSL defects close to the surface of the image plate.* The probability for the neutron to be absorbed in a phosphor layer with thickness x can be found from the well-known formula:

$$\text{Absorb}(x) = 1 - \exp\left(-\rho \cdot \frac{w}{M} \cdot N_A \cdot \sigma \cdot x\right) \quad (2.1)$$

where ρ – is the density of the material (g/cm^3), M - the molar mass of the absorbing element ($\text{g}\cdot\text{mol}^{-1}$), N_A - Avogadro constant (mol^{-1}), w - the weighting factor of the absorbing element in the phosphor, σ – cross-section for thermal neutron capture. Equation (2.1) can be considered also as a neutron absorption profile [6.4.1].

2.4.2 γ -ray sensitivity

As an example, the γ -ray background spectra in the experimental hall of the ILL/EMBL nuclear reactor measured with a Ge-semiconductor detector are shown in Figure 2.6. The spectra were recorded at two beam lines: D19 and LADI/T17 when the neutron beam was open and closed. It is seen that a significant part of the γ -rays comes from the neutron beam line. The γ -ray background at T17 is much lower than at D19, which is achieved by extra γ -ray shielding and the quite remote location of T17 line from the reactor. *Both of these factors dramatically decrease the neutron flux, which leads to a longer duration of diffraction experiments.* Presently the Laue diffractometer based on Gd-IP is located at T17 beam line. It is seen from Figure 2.6 that most of the γ -rays exist in the low energy region, even after γ -ray shielding. The main contribution to the low energy region of the spectrum after shielding is coming from Compton scattered high-energy γ -rays.

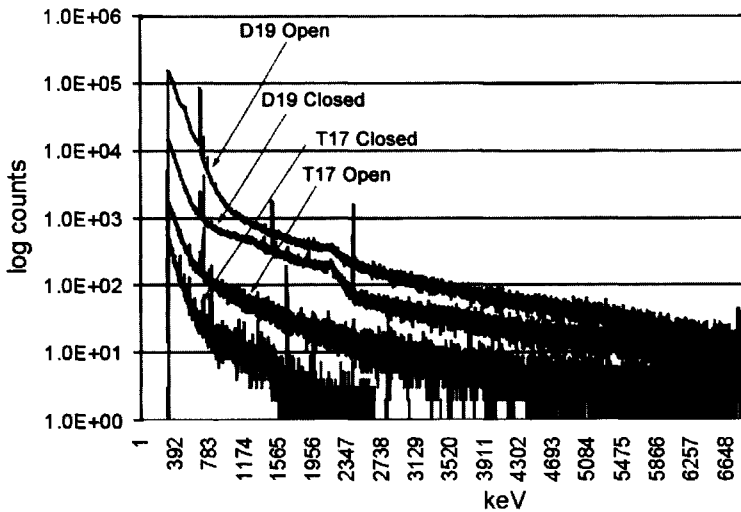


Figure 2.6: The γ -ray background spectrum recorded at two neutron beam lines of the ILL/EMBL reactor, D19 and T17. The background was measured when the neutron beam was switched on and off. The neutron beam of line T17 is used in diffraction experiments.

Therefore, the main priority for optimisation of the neutron IP is to reduce the γ -ray sensitivity. There are two ways to reduce the γ -sensitivity.

In the first approach the neutron converter is chosen in such a way, that the PSL yield from incident neutrons is much higher than that from γ -rays. For example, if ${}^6\text{Li}$ is used the energy deposition in the phosphor by secondary particles after neutron capture, which is about 4.8 MeV, is much higher than the energy deposition by captured γ -rays with energies of several hundreds of keV.

The second approach implies that Z of the material (storage phosphor and neutron converter) is chosen as low as possible. In Figure 2.2 the cross sections of the γ -ray

interaction processes in $\text{Ca}_2\text{B}_5\text{O}_9\text{Cl}$ and $\text{BaFBr}:\text{Gd}_2\text{O}_3$ are shown against the γ - energy. For a γ - ray of energy below 800 keV the probability of interaction is very dependent on Z of material. The γ -ray backgrounds in the experimental hall and in the neutron beam are mainly determined by γ -ray energies below 1 MeV. Thus a search of new neutron storage phosphors must be done among low Z materials.

When both the approaches are combined, i.e. low- Z material and a ^{10}B or ^6Li neutron converter are used, the lowest γ -ray sensitivity is expected.

2.4.3 Stimulability and spatial resolution

The typical size of the sensitive area of a diffractometer is $80 \times 40 \text{ cm}^2$ [47]. Taking a pixel size of $200 \times 200 \mu\text{m}^2$ and a read-out time of the whole area of 5 min one can get that the speed of the read-out process is $8 \cdot 10^6$ pixels per 5 min, which is about $40 \mu\text{s}$ per pixel [47].

It was shown in [48] that it takes about one second to reduce the PSL signal "e" times for the commercial ST III image plate (Fuji) using a laser with a power density of $I=0.189 \text{ mW/cm}^2$. Thus, characterisation of the PSL signal with two parameters - CE and SE can not reflect the behaviour of the PSL signal in the first tens of microseconds. Some extra parameters apart from CE and SE must be considered.

Assume that the electron traps are filled by irradiation and photons of proper energy are applied for stimulation. If the stimulating light intensity is constant then PSL signal would be formed in two stages: "1" - photo excitation of trapped electrons; and "2" - recombination of electrons with holes at a recombination or luminescence centre.

Considering stage "2", i.e. the process of charge transfer to the luminescence centre, the same process in scintillators usually takes much less than microseconds [5]. For storage phosphors the decay time constants of prompt luminescence and PSL after short-pulsed stimulation have about the same value [2,3]. Thus we can assume that the stage "2" in storage phosphors is very fast in comparison with the decay times of the luminescence centres.

If the emission of a luminescence centre has a decay time in the order of hundreds of microseconds, the greater part of the luminescence centres will not be able to give rise to PSL within the first $40 \mu\text{s}$ time window. *Thus luminescent centres with emission decay longer than several hundreds of microseconds can not provide the required read-out speed.* The emission decay of luminescence centres is at most $0.1 \mu\text{s}$ for spin-allowed transitions in lanthanides or ns^2 ions. However, the decay time of $4f \rightarrow 4f$ transitions in lanthanides is in the order of hundreds of microseconds and this appears to be too slow [49].

Let us consider an ideal phosphor, i.e. with no spreading and absorption of the light due to granular structure. If all processes of charge transport and emission by luminescent centres are very fast in comparison with the annihilation times of trapping centres upon laser stimulation, i.e. stage "1", and there are no non-radiative losses during the charge migration, one can write for the PSL intensity curve [50]:

$$L(t) = N_0 \Phi \sigma [(\beta - 1)\Phi \sigma t + 1]^{\beta/1-\beta} \quad (2.2)$$

where N_0 is the initial number of trapped electrons, $1/(1-\beta)$ is the re-trapping probability during charge migration, Φ is a photon flux and σ is the optical cross section of the transition. According to this equation the PSL intensity rises instantaneously and reaches a maximum at $t=0$. The same situation is usually observed in scintillators [5]. *Two parameters:*

σ and β determine the stimulability of a storage phosphor. N_0 and the efficiency of charge transport to the luminescence centres determine the conversion efficiency.

By increasing the laser intensity the PSL decay time can be shortened. However, the increase of the laser intensity will lead to the lower spatial resolution, due to laser light scattering in the granular structure. The results of work described in [51] show that a scanner with 40 mW laser power and a focused spot of $100 \times 100 \mu\text{m}^2$ allows a resolution of $350 \mu\text{m}$. For neutron radiography of tiny objects this resolution can be too poor, however for neutron diffraction studies a resolution up to $500 \mu\text{m}$ is acceptable.

Equation (2.2) cannot be used for fitting of PSL in real phosphor curves because of the following reasons. In a real phosphor layer, Φ will be different due to spreading and absorption of the stimulation light in the IP. It was found in [48] that in the commercial ST III image plate (Fuji) with a thickness $d=300 \mu\text{m}$, the photon flux from a laser with $I=10 \text{ mW}$ decreases linearly with the depth by a factor of 6 from the front of the IP to the back. An other IP can have a different grain size of the phosphor and composition of the binder, thus the scattering length can vary significantly.

2.4.4 Detective quantum efficiency (DQE)

In imaging the DQE is a useful parameter which determines image quality and it is defined as [47]:

$$DQE = \frac{\left(\frac{\bar{S}_0}{\sigma_0}\right)^2}{\left(\frac{\bar{S}_i}{\sigma_i}\right)^2} = \frac{\nu_i}{\nu_o} \quad (2.3)$$

where \bar{S}_i/σ_i and \bar{S}_0/σ_0 are the signal-to-noise and ν_i/ν_o relative variance ratios of the input and output signals. In the case of a neutron IP detector, the input signal is the neutron radiation field and the output signal is the photoelectron signal in the PMT. The generation of output signal is a cascade of probability events from absorption of a neutron to generation of photoelectrons in the PMT and signal formation. If we put G as the gain of a detector, then it is possible to express the mean output signal as $S_o = G \cdot S_i$. In this case the variance of the output signal is expressed as $\nu_o = \nu_i + \frac{1}{S_i} \nu_{\text{det}}$, where ν_{det} is the variance of the gain of the

detector. If the incident neutron flux is distributed according to the Poisson law ν_i equals $\frac{1}{S_i}$.

Then the DQE of a detector can be written as

$$DQE = \frac{1}{1 + \nu_{\text{det}}} \quad (2.4)$$

It means that DQE depends only on relative variance of the gain of the detector in case of Poisson statistics of the incident neutron flux. It was mentioned above that the output signal is a cascade of probability events. The relative variance for a cascade of n events is given by [52]:

$$\nu_{\text{det}} = \nu_1 + \frac{\nu_2}{\bar{s}_1} + \dots + \frac{\nu_n}{\bar{s}_1 \bar{s}_2 \dots \bar{s}_{n-1}} \quad (2.5)$$

where ν is a relative variance of an event with a mean value \bar{s} . The first event is the neutron absorption in the IP; if A is the absorption probability the $\frac{1-A}{A}$ is its relative variance. After

the neutron absorption secondary particles generate electron hole pairs. If \bar{N}_{eh} is the mean number of created electron-hole pairs per absorbed neutron, then the relative variance on the second stage of the cascade is $\frac{\nu_{Neh}}{A}$. For the sake of convenience it is easier to put all the next

stages in one and define it as S_{sped} – mean output signal per energy deposited from one neutron. It is the function of a lot of parameters, like trapping probability of the electron and/or hole by the trapping centre, stimulation probability of trapped electron and/or hole during the laser stimulation, energy transfer to the luminescence centre, escape probability of the emitted photon from the IP, probability of the emitted photon to be detected. In other words, these are the parameters, which characterise the storage properties of the phosphor itself and the readout system. The parameter S_{sped} is a function of depth z , where the neutron is absorbed in an IP, because of absorption and scattering of stimulating and emitted light in the phosphor layer. Since we are not interested in influence of these parameters on DQE we can assume that S_{sped} is already integrated over the thickness of the phosphor layer of an IP. Then, the relative variance of the gain of the detector can be expressed as:

$$\nu_{\text{det}} = \frac{1-A}{A} + \frac{\nu_{Neh}}{A} + \frac{\nu_{S_{\text{sped}}}}{A \cdot \bar{N}_{eh}} \quad (2.6)$$

Finally, the DQE is obtained as:

$$DQE = \frac{A \cdot \bar{N}_{eh}}{(1 + \nu_{Neh}) \cdot \bar{N}_{eh} + \nu_{S_{\text{sped}}}} \quad (2.7)$$

and depends linearly on the neutron absorption coefficient and the number of created electron-hole pairs. Estimations made in [53] show that about 640 optically stimuable defects are generated per absorbed neutron when the Gd_2O_3 converter mixed with BaFBr:Eu^{2+} is used and 16000 when the ${}^6\text{LiF}$ converter is used. Because these values are very large, the DQE can be rewritten as:

$$DQE = \frac{A}{(1 + \nu_{Neh})} \quad (2.8)$$

A very important conclusion can be made from formula 2.8: if a neutron IP provides a neutron absorption probability A , and it is less than 100%, the DQE of this neutron imaging device can not be more than $A \cdot 100\%$. This conclusion will be used during the discussions of material selection.

The evaluation of the DQE parameter for the Gd-IP has been performed [47]. The number of neutrons, S_i , coming from the neutron beam has been measured by a conventional single-bin counter. The same neutron flux was accumulated in a Gd-IP. After the read-out

procedure, the pixel-by-pixel variance of the counts from background corrected signals from 4000*20 pixels was evaluated. The determined DQE value was 31%.

While a low DQE does not limit the accuracy of a detector, the experimental time required to record data to a particular accuracy increases in inverse proportion to the DQE. Clearly, it is essential to maximise this quantity.

2.4.5 Fading

The duration of neutron diffraction experiments may take from several hours up to several days, depending on the neutron scattering cross-section of the sample. Thus it is becoming of great importance for storage phosphors to keep the information during a long time. As an example, in KBr:Tl⁺ stored information fades away within minutes, and, consequently such a phosphor can not be used in conventional applications.

The fading is determined by thermal stability of trapped charges. For example, thermal diffusion of hole trapping centres (like H-centres) can be responsible for fast fading. Also an electron from a trap, located close to the conduction band can thermally escape and recombine with a hole centre. In some cases it is possible to predict the position of the ground state energy relative to the conduction band, thus making control of fading properties possible [chapter 7].

2.5 Selection of materials

2.5.1 Two approaches

Two different approaches can be followed to develop neutron IPs: either use a mixture of neutron converter material with a well-known storage phosphor or search for a material, containing a neutron sensitive element in its crystal lattice.

Mixture of storage phosphor and neutron converter

Up to now Gd₂O₃ with a natural abundance of the ¹⁵⁵Gd and ¹⁵⁷Gd isotope, as well as ⁶LiF [47,54-56] are used as neutron converters. When a system is composed of a mixture of a storage phosphor and ⁶LiF, the ranges of the neutron reaction products - tritium and α -particles with kinetic energies of 2.74 and 2.05 MeV, may be assumed larger than the grain sizes of the converter material, which are in the order of a few microns [53]. Thus the energy loss in grains of converter and binder material will not be too large.

In the mixture of BaFBr:Eu²⁺ with the Gd₂O₃ converter the mean energy of conversion electrons, X-rays and low energy γ -rays deposited to the BaFBr:Eu²⁺ phosphor grains is 56.50 keV [57]. The rest is absorbed in binding material or Gd₂O₃ grains. Therefore the energy deposition in the storage phosphor in the Gd-IP is much smaller than in Li-IP. In Gd-IP the PSL signal from incident γ -rays can be comparable with the PSL yield from the incident neutron. In [58] it was shown that the PSL yield of the Gd-IP from one γ -ray with an energy below 300 keV equals one half of that from an incident neutron. The energy of γ -rays is specified because at higher energies the probability of γ -ray absorption falls down [2.2.1].

According to the above considerations one can draw the conclusion that the Li-IP is expected to be preferable over the Gd-IP for achieving better neutron / γ -ray discrimination.

A comparison of imaging properties of two types of mixtures $\text{BaFBr:Eu}^{2+} \times \text{Gd}_2\text{O}_3$ and $\text{BaFBr:Eu}^{2+} \times {}^6\text{LiF}$ has been performed in [56]. The results show that the Gd-IP absorbs neutrons more efficiently than the Li-IP. Indeed, 200 micron thick Gd-IP with a ratio of Gd-to-Ba of 1:1 absorbs 99% of 3Å neutrons, whereas Li-IP with a ratio of Li-to-Ba 3:1 absorbs only 36 % of 3Å neutrons. However, the amplification rate in the conversion process of Gd-IP is about 30 times lower.

Due to the low neutron scattering cross-section in diffraction experiments the scattered neutron flux determining the Bragg spots is very low [47]. Therefore, the application of Li-IP with 36% neutron absorption efficiency would significantly increase the experiment duration. Applying another "terminology", like DQE, we may say that the DQE of Li-IP can not be higher than 36 % [2.4.4].

To increase the neutron absorption efficiency and to keep relatively high-energy deposition into the phosphor - ^{10}B containing converters like B_2O_3 or $\text{Na}_2\text{B}_4\text{O}_7 \cdot 10\text{H}_2\text{O}$ can be proposed. However, the ranges of α -particles and ${}^7\text{Li}$ nuclei after ^{10}B decay, having kinetic energies of 1.47 and 0.83 MeV, respectively, are of the order of a few microns. Therefore, there will be significant energy loss in the grains of converter and binder material [53].

As a final conclusion: in a mixture of storage phosphor - neutron converter the most suitable neutron converter, which can provide the highest DQE is Gd_2O_3 . However, for better neutron to gamma discrimination ${}^6\text{Li}$ containing phosphors are needed.

Neutron converter in the matrix of the storage phosphor

In this case the matrix with activator must play the role of both storage phosphor and neutron converter. The X-ray storage phosphors mentioned in [2.1] exhibit very good PSL characteristics in comparison with other known storage phosphors. The search of new neutron sensitive storage phosphors must be done among the compounds containing Gd, Li or B elements in their matrix. This reduces the number of possible materials to be investigated. The task to find such a material, having storage properties comparable with BaFBr:Eu^{2+} is very difficult.

However, in Gd-IP the mean energy deposited from secondary radiation to the BaFBr:Eu^{2+} phosphor grains is 56.50 keV per absorbed neutron. In a boron containing storage phosphor the energy deposition to the phosphor per absorbed neutron from α -particles and ${}^7\text{Li}$ nucleus is about 40 times higher [57]. In contrast to mixtures of storage phosphor and neutron converter, there are no losses occurring in grains of converter or binder. However, the higher ionisation density produced by the particles from the ^{10}B reaction can affect the conversion efficiency of a storage phosphor.

In ${}^6\text{Li}$ containing storage phosphors more photostimulable defects per absorbed neutron can be produced than in phosphors containing ^{10}B . However, due to the smaller neutron absorption efficiency the DQE of lithium based storage phosphors is expected to be lower in comparison with boron containing materials.

Thus, even if the PSL yield of boron- or lithium- containing storage phosphors under X-ray irradiation is smaller in comparison with BaFBr:Eu^{2+} , the situation can change dramatically upon neutron irradiation. Boron containing phosphors are more preferable than those containing lithium because of higher neutron capture cross-section.

We chose the second approach; i.e. the search of materials will be done among compounds containing a neutron sensitive element in its structure. The calculations presented in [57] show that a higher DQE can be achieved in this case in comparison with a mixture of storage phosphor and neutron converter.

2.5.2 Choice of compounds

According to the considerations above boron containing materials with a high molar ratio of boron atoms seem to be the most perspective. We did several attempts to find an appropriate boron-containing matrix and activator, which exhibits promising PSL yield. A number of borates doped with Ce^{3+} ions do not exhibit any TL and PSL signal. M. Kmitel [59] also studied a large number of borate compounds doped with Ce^{3+} or Eu^{2+} , for which no significant TL or PSL signal could be detected.

Haloborates

Haloborates doped with Eu^{2+} were proposed at first as X-ray storage phosphors by Meijerink *et al.* [60]. After that Kmitel suggested to use $Sr_2B_5O_9Br:Eu^{2+}$ as a neutron storage phosphor [61]. We found that Ce^{3+} doped haloborates are more suitable for application than those doped with Eu^{2+} . Therefore a detailed investigation of haloborates doped with Ce^{3+} has been performed [chapters 4,5 and 6 of this thesis].

Double doping with lanthanides

It was shown in [2.3.2] that some lanthanides could be converted to the di-valent state and some of them to the four-valent state. Thus, one of them can play the role of electron trap and another of the hole trap. The first idea to make a storage phosphor in which lanthanides form active PSL trapping centres comes from late 60s [62]. Storage properties of sulphides doped with Eu^{2+} and Sm^{3+} ions have been intensively studied. However, except for sulphides and $Y_2Si_2O_5:Ce^{3+},Sm^{3+}$ [63] no compounds doubly doped with lanthanides exhibiting storage effect have been found.

A number of samples doubly doped with lanthanides (Ce^{3+},Sm^{3+}) has been checked for the presence of any storage effect: SrB_4O_7 , SrB_6O_{10} , $Sr_2B_5O_9X(Cl,Br)$, YBO_3 , $Li_6Y(BO_3)_3$, Li_2CaSiO_4 .

It was not possible to stabilise Sm ions only in the trivalent state in borates with divalent cations. A significant amount of divalent Sm was found in all samples. Stability of Ln^{2+} ($Eu^{2+}, Sm^{2+}, Yb^{2+}$) in borates has been studied in [64]. It was established that stability of Ln^{2+} increases in the order $Sr_3(BO_3)_2, Sr_2B_2O_5 \rightarrow Sr_2B_5O_9X(Cl,Br) \rightarrow SrB_4O_7, SrB_6O_{10}$. It was not possible to stabilise Sm or Eu ions only in the trivalent state in SrB_4O_7, SrB_6O_{10} and $Sr_2B_5O_9X(Cl,Br)$; not even during the synthesis in oxygen atmosphere. At the same time a strong luminescence from Ce^{3+} centres was observed in these materials synthesised in neutral atmosphere, which is evidence that most of the Ce^{3+} ions are introduced in the tri-valent state.

In YBO_3 and $Li_6Y(BO_3)_3$ Ce and Sm ions were found only in the trivalent state. However, no storage effect has been detected.

In Li_2CaSiO_4 samples a strong TL signal was detected in Ce and Ce,Sm doped samples. The Ce and Sm ions were found in the trivalent state. It was assumed that the Li_2CaSiO_4 matrix acts as an electron trapping centre and Ce^{3+} as hole trap. The Sm ions, probably are not involved in the trapping process. No PSL signal has been detected during the stimulation at 470, 630 and 830 nm. The luminescence properties of $Li_2CaSiO_4:Ce^{3+}$ can be found in [65].

A strong TL and PSL signal has been detected in $\text{LiLuSiO}_4:\text{Ce}^{3+},\text{Sm}^{3+}$ and $\text{LiYSiO}_4:\text{Ce}^{3+},\text{Sm}^{3+}$ compounds. In both samples Ce and Sm act as hole and electron trapping centres respectively. Due to the low neutron absorption efficiency these compounds hardly can be used for thermal neutron detection, however the understanding of the trapping and recombination mechanism is crucial for development of storage phosphors based on double doping with lanthanide ions. Therefore, these materials will be fully discussed in Chapter 7.

References

- [1] Schweizer S., Phys. Stat. Sol. A **187** (2) (2001) 335
- [2] Pawlik Th. and Spaeth J.-M., Proc. SCINT'95, Delft University Press (Netherlands) 1995 (p.392)
- [3] Hangleiter Th., Rogulis U., Dietze C. *et al.*, Proc. SCINT'95, Delft University Press (Netherlands) 1995 (p.452)
- [4] Rowlands J. A., Phys. Med. Biol. **47** (2002) R123-R166
- [5] Rodnyi P. A., Physical processes in inorganic scintillators, CRC Press, 1997
- [6] Knoll G.F., *Radiation detection and measurement*, 3rd edition, J. Wiley and Sons, 1999
- [7] Backlin A., Hedin G., Fogelberg B. *et al.*, Nucl. Phys. A **380** (1982) 189
- [8] Greenwood R. C., Reich C. W., Baader H. A., Nucl. Phys. A **304** (1978) 327
- [9] Rodnyi P. A., Dorenbos P., van Eijk C. W. E., Phys. Stat. Sol. B **187** (1995) 15
- [10] Song K. S. and Williams R. T., *Self Trapped Excitons*, Springer-Verlag 1993
- [11] Pooley D., Proc. Phys. Soc., **87** (1966) 245
- [12] Hersh H. N., Phys. Rev., **148** (1966) 928
- [13] Dolbnaya I. P., Kulipanov G. N., Lyakh V. V. *et al.*, Nucl. Instr. Meth. **7** (1995) 376
- [14] Agullo-Lopez F. *et al.*, *Point Defects in Materials*, Academic Press, 1988
- [15] Liebich B. W., Nicollin D., Acta Cryst. B **33** (1977) 2790
- [16] Hangleiter Th., Koschnick F.K., Spaeth J.M. *et al.*, J. Phys.: Condens. Matter **2** (1990) 6837
- [17] Schweizer S., Spaeth J.M., Bastow T. J., J. Phys.: Condens. Matter **10** (1998) 9111
- [18] Bastow T. J., Stuart S. N., McDugle W. G., J. Phys.: Condens. Matter **6** (1994) 8633
- [19] Eachus R. S., McDugle W. G., Nutall R. H. D., J. Phys.: Condens. Matter **3** (1991) 9327
- [20] Eachus R. S., McDugle W. G., Nutall R. H. D., J. Phys.: Condens. Matter **3** (1991) 9339
- [21] Koschnick F. K., Hangleiter Th., Song K. S., J. Phys.: Condens. Matter **7** (1995) 6925
- [22] Koschnick F.K., Spaeth J.M., Eachus R. S., Phys. Rev. Lett. **67** (25) (1991) 3571
- [23] Meise W., Rogulis U., Koschnick F.K. *et al.*, J. Phys.: Condens. Matter **6** (1994) 1815
- [24] Agullo-Lopez F., *et al.*, Cryst. Lattice defects Amorph. Mat., **9** (1982) 227
- [25] Rogulis U., Spaeth J.M., Cabria I. *et al.*, J. Phys.: Condens. Matter **10** (1998) 6473
- [26] Rogulis U., Spaeth J.M., Cabria I. *et al.*, J. Phys.: Condens. Matter **10** (1998) 6481
- [27] Delbecq C. J., Ghosh A. K., Yuster P. H., Phys.Rev. **151** (1966) 599
- [28] Rogulis U., Dietze C., Pawlik T., J. Appl. Phys. **80** (4) 1996 2430-5
- [29] Schoemaker D., Phys.Rev B. **7** (1973) 786
- [30] Rogulis U., Schweizer S., Assmann S. *et al.*, J. Appl. Phys. **84** (1998) 4537
- [31] Rogulis U., Schweizer S., Assmann S. *et al.*, J. Appl. Phys. **87** (2000) 207
- [32] Thiel C. W., Cruguel H., Sun Y., J. Lumin. **94-95** (2001) 1-6
- [33] Mårtensson N., Reihl B., Pollak R. A., Phys. Rev. B **25** (1982) 6522-6525
- [34] Dorenbos P., J. Phys.: Condens. Matter **15** (2003) 575-594
- [35] Brewer L., J. Opt. Soc. Am. **61** (1971) 1666
- [36] Dorenbos P., J. Phys.: Condens. Matter **15** (2003) 8417-8434

- [37] Grinyov B. V., Dubovik M. F., *Semic.Phys. Quant.Elect.&Optoe.*, **3** (3) (2000) 410
- [38] Griscom D. L., *J. Non-Cryst. Sol.* **13** (2) (1974) 251
- [39] Shkrob I., Tadjikov B. M., Trifunac A. D., *J. Non-Cryst. Sol.* **262** (2000) 6-34
- [40] Chung W. J. and Heo J., *Appl.Phys. Let.* **79** (3) (2001) 326
- [41] Warren W.L., Shaeyfelt M.R., Fleetwood D.M., *IEEE trans. Nucl. Science* **42** (6) (1995) 1731
- [42] Boizot B., Petit G., Ghaleb D. *et al.*, *Nucl. Instr. Meth. B* **141** (1998) 580
- [43] Shkrob I. A., Tarasov V. F., *J. Chem. Phys.* **113** (23) (2000) 10723
- [44] Ogorodnikov I. N., Isaenko L. I., Kruzhalov A. V. *et al.*, *Rad. Meas.* **33** (2001) 577-581
- [45] Meijerink A., Blasse G. and Glasbeek M., *J. Phys.: Condens. Matter*, **29** (1990) 6303
- [46] Thoms M., *Appl. Optics* **35** (19) (1996) 3702
- [47] Myles D. A. A., Bon C., Langan P. *et al.*, *Phys. B* **241-243** (1998) 1122-1130
- [48] Thoms M., *Nucl. Instr. Meth. A* **378** (1996) 598-611
- [49] Blasse G., Grabmaier B C, *Luminescent Materials*, Springer Press, 1994
- [50] Bulur E., *Radiat. Meas.* **26** (5) (1996) 701-709
- [51] Thoms M. and von Seggern H., *J.Appl.Phys.* **81** (9) (1997) 5887
- [52] Breitenberger E., *Prog. Nucl. Phys.* **4** (1955) 56
- [53] Thoms M., Myles D., Wilkinson C., *Nucl. Instr. Meth. A* **424** (1999) 26-33
- [54] Kobayashi H. and Satoh M., *Nucl. Instr. Meth. A* **424** (1999) 1-8
- [55] Haga Y. K., Neriishi K., Takahashi K. *et al*, *Nucl. Instr. Meth. A* **487** (2002) 504-510
- [56] Takahashi K., Tazaki S., Miyahara J. *et al.*, *Nucl. Instr. Meth. A* **377** (1996) 119-122
- [57] Knitel M.J., Bom V.R. , Dorenbos P. *et. al*, *Nucl. Instr. And Meth. A* **449** (2000) 578-594
- [58] Haga Y. K., Kumazawa S., Niimura N., *J. Phys. Chem. Solids* **60** (1999) 1619-1621
- [59] Knitel M. J., Dorenbos P., van Eijk C. W. E., *Nucl. Instr. And Meth. A* **443** (2000) 364-374
- [60] Meijerink A., Blasse G., *J. Phys. : Appl. Phys.* **24** (4) (1991) 626-632
- [61] Knitel M. J., Hommels B., Dorenbos P. *et al.*, *Nucl. Instr. And Meth. A* **449** (2000) 595-601
- [62] Levshin V. L. *et al.*, *Izvestiya Akademii Nauk SSSR*; **33** (6) (1969) 962
- [63] Meijerink A., Schipper W. J. and Blasse G., *J. Phys. D: Appl. Phys.* **24** (1991) 997-1002
- [64] Dotsenko V. P., *Doctoral thesis*, Odessa, Ukraine
- [65] Dorenbos P., Pierron L., Dinca L., *J. Phys.: Condens. Matter* **15** (3) (2003) 511-520
- [66] Dotsenko V. P., *Borates of elements in I-II groups: synthesis – structure – spectroscopic properties*, dissertation for the 2nd habilitation, Odessa 2002



3 Experimental techniques

3.1 Introduction

Characterisation of spectroscopic and storage properties of studied materials and investigation of the nature of the radiation induced defects were performed by means of different spectroscopic techniques. They will be reviewed in this chapter.

3.2 Samples

All the borates were prepared in A.V. Bogatsky Physico-Chemical Institute, Odessa, Ukraine. The solid solutions of $M_{2(1-x)}Ce_{2x}B_5O_9X(x=0.001\div 0.01)$ where $M=Ca, Sr, Ba$ and $X=Br, Cl$ were prepared using a standard solid state method [1]. In case of $M=Sr$ and $X=Br$ starting mixtures of $SrCO_3$, $SrBr_2 \cdot nH_2O$ (10% excess), $Ce(NO_3)_3$ and H_3BO_3 (15% excess) were fired at a temperature of about $400^\circ C$ for 1 hour and then at $750-800^\circ C$ for 3 hours in a nitrogen stream. The samples were cooled, ground in a mortar to insure homogeneity and fired again at $800^\circ C$ for 2 hours in a weakly reduced atmosphere consisting of a nitrogen-hydrogen mixture containing 2% by volume of hydrogen. In some cases the starting powders were codoped with (Na^+, K^+) . In case of other M and X the firing temperatures and duration of firing are a bit different. The whole list of studied borates is presented in Table 6.1.

Synthesis of silicates is described in Chapter 7.

For the experiments samples were pressed into 30-mg pills with 5mm diameter, unless other conditions are mentioned.

3.3 Characterisation of spectroscopic properties

The X-ray excited emission spectra were recorded using an X-ray tube with a Cu-anode operated at 35kV and 25mA. The ARC VM-504 monochromator was used, which has 3 movable gratings (1200 grooves/mm, blazed at 150nm, 300nm and 750nm). Measurements in the 200-600 nm region were carried out with a Hamamatsu R943-02 photomultiplier tube (PMT) and in the 600-900 nm region with an EMI 9426 PMT. The angle between the incident X-ray beam and the focus line of the detected emission is 90° . The setup also allows carrying out measurements at liquid nitrogen temperatures.

Diffuse reflection measurements were performed with a diode array UV/VIS spectrophotometer (HP 8452A) equipped with a 95 mm diameter Spectralon Integrating Sphere (RSA-HP-84-UV) with an externally mounted xenon light source allowing

measurements in the 300-800 nm wavelength range. Large area samples were compared with a calibrated 99% diffuse reflectance standard.

Optical excitations in the UV/VIS region and emission spectra were recorded at room temperature using the spectrophotometer Quanta Master QM1 of Photon Technology International (PTI). This system consists of a 75 W Xenon lamp (PTI PowerArc™), a double excitation monochromator (PTI 121 A) and an emission monochromator (PTI 170) with a PMT unit (PTI 710). The emission spectra are corrected for the wavelength dependency of the measurement device and spectral sensitivity of the light detector. Sodium salicylate was used as a reference material to correct the excitation spectrum for the lamp spectrum.

Excitation spectra around 10K were performed at the Deutsche Elektronen Synchrotron (DESY) in Hamburg (Germany) at the SUPERLUMI station of Hasylab. The synchrotron operated in multibunch mode with bunches separated by 200 ns. The "short time" excitation spectra were recorded after 1.5 ns delay in a 12 ns time gate. Time delayed excitation spectra were recorded after 74 ns delay in an 85 ns time gate. Excitation spectra at room temperature were recorded using a laboratory VUV spectrofluorometer. The detailed properties of this setup were described in [2].

3.4 Characterisation of storage properties

3.4.1 Thermally stimulated luminescence

TL measurements were performed with a Riso-TL/OSL-DA-15A/B reader. The system allows to carry out measurements with a heating rate from 0.05 K/s to 10 K/s. The reader has an internal β -irradiation source ($^{90}\text{Sr}/^{90}\text{Y}$) with the dose-rate of 1.0 mGy/s in air.

A thermally stimulated luminescence, or thermoluminescence (TL) measurement, results in a graph of emission intensity versus temperature, i.e., the TL glow curve. The TL measurements can give an impression about the number of trapping centres and their relative depth. Let us assume that a certain type of TL active defect is formed as a result of ionising irradiation. For example, it can be an electron trapped on a halide vacancy (F- centre), V_k centre or an electron/hole trapped on an impurity ion [5.3]. With increase of temperature the trapped charge can be liberated by heat. In case of a trapped hole (V_k or similar centres) increase of temperature leads to the spatial migration of these centres. A trapped electron can be released to the conduction band with further re-trapping or recombination with a luminescence centre or tunnel to a nearby quenching or luminescence centre. At a temperature T (in K), the rate of release of trapped electrons is proportional to the Boltzmann function $\exp(-E_t/kT)$ where E_t is the "activation energy" (in eV) of the trap and k is the Boltzmann constant (in eV/K). In [3] the detailed theory of thermoluminescence is given, based on the simplified model of Randall and Wilkins. According to [3], in case of no re-trapping of a released electron (first-order Randall-Wilkins kinetics) the TL glow curve can be expressed as:

$$TL(T) = sn_0 \exp\{-E_t/kT\} \exp\left[-\frac{s}{\beta} \int_{T_0}^T \exp\{-E_t/k\vartheta\} d\vartheta\right], \quad (3.1)$$

where s [s^{-1}] is called oscillation frequency, β [K/s] is the heating rate, n_0 number of created trapped charges by irradiation. A similar equation has been derived for the general-order

kinetics, i.e. when there is a probability of re-trapping for released charge. In case of non-first order kinetics the linearity with n_0 disappears, i.e. the position of a TL peak will depend on the number of created defects, i.e. irradiation dose.

Many studies are dedicated to the fitting of an experimental TL glow curve with the Randall-Wilkins approximation. The TL fitting results in actual values of two fitting parameter, s and E_t . However, there are several cumbersome features, which raise the question whether the TL fit must be performed:

- The task of the TL fitting procedure does not have a limited number of solutions (set of parameters s and E_t).
- The liberation of the charge carriers from the trap during thermal stimulation occurs from excited molecular levels, which are, in principle, unknown. Therefore the activation energy parameter E_t , defined via Boltzmann energy is not correlated with the trap depth energy, derived from direct optical transitions. Thus the fitting of TL curves cannot be used as an addition to spectroscopy techniques for construction of energy level diagrams.
- The TL glow curve, which is used for fitting must be corrected for the temperature-dependent quenching of the luminescence, which requires additional long-duration experiments.
- The Randall-Wilkins theory assumes that the trap depth is single valued in energy. However, it can be that the activation energy of trapped charges is distributed within a certain range. In this case the theory becomes more complicated [3], and, probably, hardly applicable.

Thus the process of TL glow curve fitting appears to be quite time consuming and results in values, which cannot be used in combination with the results obtained from other techniques. In this work the TL technique was used to obtain the following information:

- Number of TL peaks and position of their maxima. The number of peaks corresponds to the number of trapping centres and the position of a peak maximum to the relative energy depth of a trap [4.3.3 and 7.5.1].
- Before providing the TL measurements, an irradiated sample can be illuminated with photons of certain wavelength and intensity. Thus, information about the photosensitivity of certain types of traps can be derived [6.3.1 and 7.6.2].
- The TL techniques cannot provide information about the nature of traps. However, TL in combination with EPR techniques can be very useful [5.3.1].
- If the trap filling is possible by illumination with photons of certain wavelength, and TL is recorded afterwards, information about trap filling efficiency can be derived. The latter can be used as additional information for determination of the trap nature [5.2.4 and 7.5.2].

We used the TL technique to predict the yield of studied materials upon photostimulation. However, as it will be shown in [6.3.1], sometimes the recombination processes of trapped carriers with luminescence centres can occur differently upon thermal and optical stimulation.

3.4.2 Photostimulated luminescence (PSL)

The effect of photostimulated luminescence has already been introduced in [2.4.3]. For the best achievement of image plate performance, the wavelength of a stimulation source must match to the stimulation energy of trapped carriers. The stimulation spectra of PSL were

measured in a homemade setup, well described in [4]. Since the sensitivity of the setup is low, the samples were irradiated for 1 hour by a ^{60}Co source with a dose rate of 1kGy/h.

The PSL measurements of studied materials were provided with the help of the Riso-TL/OSL-DA-15A/B reader. A schematic view of the sample holder and the position of light sources is shown in Figure 3.1.

Several types of stimulation sources were used in the PSL measurements:

- Ring of Blue Emitting Diodes (Blue LED's) with a wavelength of 470 nm and a total power density of 16 mW/cm^2
- Infrared diode with a wavelength of 830 nm and an output power density of 400 mW/cm^2
- Nd:YVO₄ solid state diode-pumped 10 mW laser emitting at 532 nm and producing a spot of approximately 120 μm in diameter at the surface of a sample

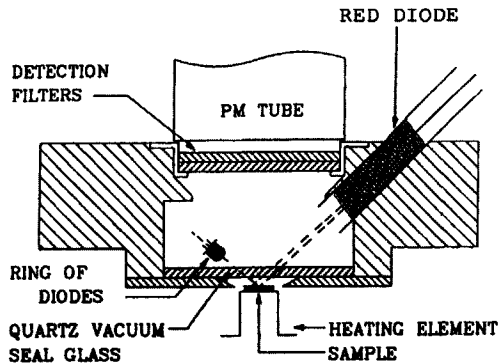


Figure 3.1: Schematic view of Riso-TL/OSL-DA-15A/B reader.

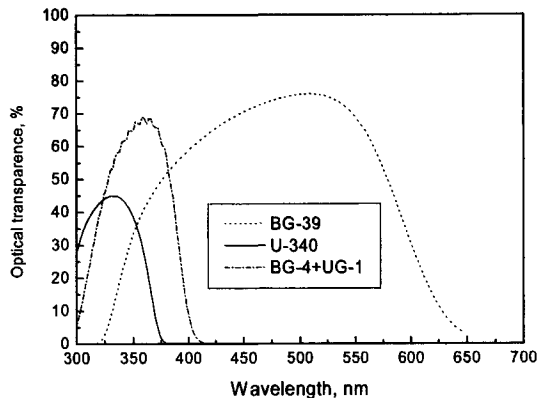


Figure 3.2: Transmission curves of some detection filters used in the PSL measurements.

In order to cut off the scattered light of the stimulation sources from the PMT window band filters were used. For each light source certain cut-off filters were used:

- Set of 3 U-340 filters (7 mm total thickness) was used in combination with Blue LED's
- Set of BG-4 + UG-1 filters was used in combination with Nd:YVO₄ laser

- BG-39 filter was used with Infrared Diode
The transmission curves of these filters are given in Figure 3.2.

3.4.3 Performance comparison of different storage phosphors

For quantitative comparison of storage phosphors CE, SE and CE/SE parameters are usually used [2.1]. Actually, this is not very correct. As was mentioned in [2.4.3], during the read out of an IP in an IP-scanner the integrating time of one pixel is limited to about 40 μs , which is determined by the large area of an IP (typically $80 \times 40 \text{ cm}^2$) and the required resolution (typically $200 \times 200 \mu\text{m}^2$). Therefore for the read-out experiment illustrated in Figure 2.1 it would be more correct to use the value "maximal PSL signal in the first X ms of stimulation", where X is an integration time per one channel during the read out procedure. In the TL Riso-TL/OSL-DA-15A/B reader the minimal allowed integrating time per data point is 10 ms. This time could be too long for the precise quantitative comparison of storage phosphors because of the following reason.

Let us assume that traps are filled by irradiation and photons of proper wavelength are applied for the stimulation. If the excitation light intensity is constant then observation would be the decay of PSL (PSL curve). The probability per second for the electron to leave the trap is proportional to the intensity of excitation, say $\Phi\sigma$ (in s^{-1}), where Φ is the intensity of excitation light, and σ is the optical cross section of the transition, leading to the creation of the PSL photon. The process is very similar to observation of the TL at a fixed temperature. The transfer of charge carriers can be described by a well-known differential equation. If one assumes the first-order kinetic (no re-trapping), the PSL curve can be described by the formula:

$$L(t) = L_0 \exp^{-\Phi\sigma t} \quad (3.2)$$

where L_0 is the PSL yield at $t=0$. Thus experimental PSL can be simulated as:

$$L(i) = \int_{t_i}^{t_{i+1}} L_0 \exp^{-\Phi\sigma g} dg, \quad i = 0, \dots, T/T_{ch} \quad (3.3)$$

where L_0 is the PSL yield at $t=0$, and T_{ch} is the minimal allowed integrating time per data point in a read-out setup, T is the duration of PSL read-out experiment.

Let us assume that we have two IPs, which must be compared. They have the same properties, however the σ of the first (IP₁) is 50 times bigger than that of the second (IP₂). This means that the SE [$\mu\text{J}\cdot\text{mm}^{-2}$] of IP₁ is 50 times smaller than that of IP₂. In Figure 3.3 the PSL curves of both IPs are compared. In Figure 3.3a the time per data point (T_{ch}) was chosen 10 ms and in Figure 3.3b, 40 μs . Considering only the result in Figure 3.3a, one can draw the conclusion that the performance of IP₁ in a commercial IP-scanner (integrating time of one pixel is about 40 μs) would be 14 times better than that of IP₂ (ratios of L_i values in the first channel for both IP). Considering the results in Figure 3.3b, one can draw the conclusion that the performance of IP₁ in a commercial IP-scanner is 45 times better than IP₂. The conclusion made from Figure 3.3b is true, since the same integration time is used in an experiment upon constant laser stimulation in an IP-scanner. Thus, the correct conclusion about the performance of a storage phosphor after performing the PSL measurements can be done only if the setup allows an integrating time small enough to be comparable with the integrating

time in the IP-scanner. In the TL Riso-TL/OSL-DA-15A/B reader the minimal allowed integrating time per data point is 10 ms. The latter means that the results obtained with Riso-TL/OSL-DA-15A/B reader can only be used as a rough estimation.

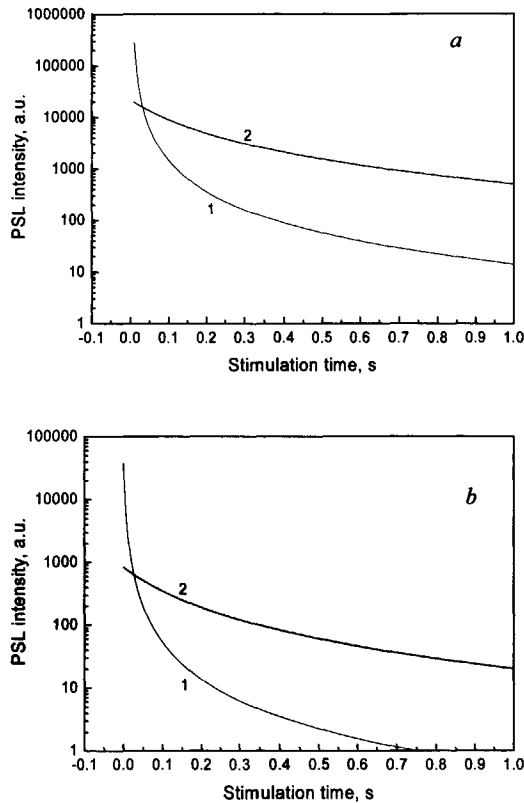


Figure 3.3: Simulated PSL curves of IP_1 (σ 50 times larger, curve 1) and IP_2 (curve 2). In Figure 3.3a the time per data point (T_{ch}) was chosen 10 ms and in Figure 3.3b - 40 μ s

Commercial Image Plate scanners

All the known commercial AGFA and Fuji scanners were developed for an IP containing BaFBr:Eu²⁺ storage phosphor. Therefore they are equipped with a He-Ne (633nm) laser as stimulation source. An interference filter for protection of the PMT from scattered laser light is optimally chosen for transmission of only Eu²⁺ luminescence in BaFBr, i.e. around 390 nm.

In order to perform a correct comparison of studied storage phosphors with a commercial one, the read-out system should be optimal for both of them. However, if the stimulation efficiency of studied phosphors is not optimal when stimulated with $\lambda \sim 633$ nm, and the PSL

emission spectrum does not have a maximum at 390 nm, no direct comparison can be made [6.3.3].

Single grain attachment to Riso-TL/OSL-DA-15A/B reader

The direct comparison of the PSL properties of studied materials with commercial BaFBr:Eu²⁺ was done with a single grain attachment to the Riso-TL/PSL reader. The reader was designed to measure sand-sized grains [5]. However it appears that the read-out parameters of this system are about optimal for all studied materials and the commercial phosphors [6.3.4 and 7.9.2]. The system employs a 10 mW Nd:YVO₄ solid state diode-pumped laser emitting at 532 nm, producing a spot approximately 120 μm in diameter at the surface of the sample disc. In our PSL experiments we used 10 % of the full laser power. Small portions of powder samples were put in 300 μm wide and 300 μm deep holes drilled into the surface of 10 mm diameter and 0.5 mm thick disk. The holes are located precisely in a ten by ten grid pattern giving a total of 100 pixels of photo-stimulated phosphor on each sample disk. The laser beam can scan the disk pixel by pixel. Thus the read-out conditions are very similar to those used for reading irradiated image-plates.

Each pixel was read out for 2s, and the PSL signal was recorded in an array of 100 channel. The value of the first channel represents the detected PSL signal in the first 20 ms of laser stimulation. The PSL properties of studied phosphors will be characterised by this value.

3.5 EPR technique

The EPR measurements were carried out at the Laboratory of Solid State-Applied Chemistry at the ENSCP (Paris), with a Bruker ESP300e spectrometer. The microwave frequency was measured with a Systron Donner frequency counter. All the spectra were corrected for the signal from the cavity with the empty sample holder (quartz tube).

Irradiation was performed ex-situ with a Siemens X-ray tube operating at 40 keV and 35 mA.

Electron paramagnetic resonance is a technique in which radiation of microwave frequency is absorbed by centres, possessing an electron with an unpaired spin when a strong magnetic field is applied. An electron possesses a "spin" (*s*) of 1/2, which has two energy levels. The lower energy level corresponds to $m_s = -1/2$ in which the spin magnetic moment is aligned with the field. At the high energy level, $m_s = +1/2$, the magnetic moment opposed to the field. The energy difference between the two spin states can be related to the microwave radiation frequency as:

$$\Delta E = h\nu = g\beta H_0 \quad (3.4)$$

where β is the Bohr magneton; g is the splitting factor; H_0 is the applied field. The interaction of the unpaired electron in a sample with the applied magnetic field is termed as Zeeman effect. The two spin states have the same energy in the absence of a magnetic field and the energies of the spin states diverge linearly as the magnetic field increases. In a conventional EPR experiment, the magnetic field is swept in the presence of the microwave radiation of constant frequency. A peak of absorption is observed at the magnetic field, for which the energy between the two spin states is equal to the applied energy of the microwave radiation.

g-factor

In the resonance condition, the g -factor determines the position of the line in the EPR spectrum and represents the sole value associated with the characteristics of the centre and its environment [6]. The g -factor of a free electron is $g_e=2.0023$. For bound unpaired electrons internal magnetic fields can shift and/or split the basic resonance line into several components. The orbital angular momentum of the electron gives a contribution to the total magnetic moment, which produces a shift in the g -factor from the free electron value. If a negative g -shift is obtained relative to g_e , it is typically attributed to an "electron" centre, while a positive g shift is characteristic of "hole" centres.

For crystal fields with a symmetry lower than cubic, g becomes anisotropic and the structure of the tensor reflects the symmetry of the crystal field. In fact, the principal axes of the g tensor determine the symmetry axes of the paramagnetic centre. In a powder sample, which is composed of many microcrystals that are oriented in all possible directions, the spectrum will be an envelope of all possible spectra due to the different orientation of the centre relative to the magnetic field.

Hyperfine splitting:

Surrounding nuclei, which possess a spin ($I \neq 0$) and hence a magnetic moment may interact with the unpaired electron. The magnetic interaction between magnetic nuclei and the electron, the so-called hyperfine interaction, produces a splitting of the basic resonance line into a number of hyperfine components. The hyperfine interaction depends on the unpaired electron distribution and on the distance between it and the nuclei.

References

- [1] Dotsenko V. P. *et al.*, *J. of Lumin.* **93** (2) (2001) 137
- [2] van der Kolk E., *Photon cascade emission of Pr³⁺ and optimization of Mn²⁺ based phosphors*, Ph.D Thesis, Delft University of Technology, 2001
- [3] Chen R. and McKeever S. W. S., *Theory of thermoluminescence and related phenomena*, World Scientific Publishing, 1997
- [4] Kmitel M. J., *New inorganic scintillators and storage phosphors for detection of thermal neutrons*, Ph.D Thesis, Delft University of Technology, 1998
- [5] Duller G. A. T. *et al.*, *Nucl. Instr. And Meth. B* **155** (1999) 506-514
- [6] Abragam A. and Bleaney B., *Electron Paramagnetic Resonance of Transition Ions*, Clarendon Press, Oxford (1970)

4 Luminescence and Thermoluminescence of $\text{Sr}_2\text{B}_5\text{O}_9\text{X}:\text{Ce}^{3+},\text{A}^+$ ($\text{X}=\text{Cl},\text{Br}$, $\text{A}=\text{Na}^+,\text{K}^+$) phosphors

4.1 Introduction

The work presented in this chapter is part of a more extensive study where the properties of Ce^{3+} doped haloborate storage phosphors are investigated. Barium bromoborate activated with Eu^{2+} has been proposed at first as an X-ray storage phosphor by Meijerink *et al.* [1]. After that Knitel suggested to apply $\text{Sr}_2\text{B}_5\text{O}_9\text{Br}:\text{Eu}^{2+}$ as a neutron storage phosphor [2]. As will be shown later in chapter 6 haloborates doped with Ce^{3+} show better storage characteristics in comparison with those doped with Eu^{2+} .

The luminescence properties of $\text{Sr}_2\text{B}_5\text{O}_9\text{Br}:\text{Ce}^{3+}$ have been reviewed recently in [3]. We performed an extended spectroscopic study of the series of $\text{Sr}_2\text{B}_5\text{O}_9\text{X}:\text{Ce}^{3+},\text{A}^+$ ($\text{X}=\text{Cl},\text{Br}$, $\text{A}=\text{Na}^+,\text{K}^+$) phosphors by means of optical and EPR techniques. We also studied the thermoluminescence properties of these materials and contributions of different Ce^{3+} centres in the TL emission spectra. The data presented in this chapter will be used later on when the storage mechanism of haloborates is discussed.

We performed the EPR measurements on $\text{Sr}_2\text{B}_5\text{O}_9\text{Br}:\text{Ce}^{3+}$ in addition to conventional luminescence studies. The Ce^{3+} ion is paramagnetic and electron paramagnetic resonance should be an available tool to obtain the crystallographic site location and the influence of neighbouring defects on the Ce^{3+} centre in the lattice. However, to our knowledge only a few EPR studies on Ce^{3+} in polycrystalline materials are available in the open literature.

The ground state of the Ce^{3+} ion is $^2F_{5/2}$, i.e., $L=3$, $S=1/2$, and $J=5/2$. The excited state $^2F_{7/2}$ lies approximately 2000 cm^{-1} above $^2F_{5/2}$. The low-symmetry crystal field splits the $^2F_{5/2}$ ground state into three Kramers doublets with M_J equal to $\pm 5/2$, $\pm 3/2$, and $\pm 1/2$. Under dissimilar conditions these doublets may lie lower or higher relative to each other, depending on the intensity of the crystalline field, the distance between them may vary from 10 to 100 cm^{-1} and greater.

While information on the crystallographic structure of $\text{Sr}_2\text{B}_5\text{O}_9\text{Br}$ is lacking, structural data on $\text{Eu}_2\text{B}_5\text{O}_9\text{Br}$ are available [4]. Europium can occupy two crystallographic positions in the matrix, in each of which it is surrounded by seven oxygen atoms of the borate groups and two halogen atoms. Because the ionic radii of Eu^{2+} and Sr^{2+} are close in magnitude [5], we assumed that the europium- and strontium-based haloborates have similar crystallographic parameters. The two strontium atoms in $\text{Sr}_2\text{B}_5\text{O}_9\text{Br}$, which occupy different crystallographic positions, have a very similar environment, but with a slightly different arrangement of the nearest neighbour oxygen ions (Figure 4.1).

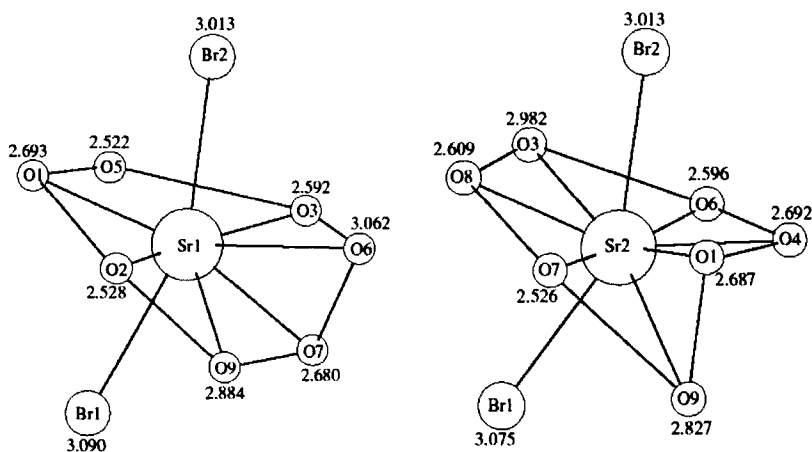


Figure 4.1: Polyhedra of substituted strontium ions in two crystallographic positions. The number of surrounding oxygen and halogen ions in both cases is the same.

4.2 Materials

For the experiments several solid solutions of haloborates were synthesised in the A.V. Bogatsky Physico-Chemical Institute using the solid state method as described in [3]. The samples studied in this work are:

series of non-co-doped $\text{Sr}_2\text{B}_5\text{O}_9\text{Br}$ and $\text{Sr}_2\text{B}_5\text{O}_9\text{Cl}$ samples with different concentrations of Ce^{3+} between 0.05 and 5 mol%

series of co-doped compounds: $\text{Sr}_{2(1-x)}\text{Ce}_x\text{Na}_x\text{B}_5\text{O}_9\text{Br}$ ($x=0, 0.01$ and 0.001), $\text{Sr}_{2(1-x)}\text{Ce}_x\text{K}_x\text{B}_5\text{O}_9\text{Br}$ ($x=0.001$) and $\text{Sr}_{2(1-x)}\text{Ce}_x\text{Na}_x\text{B}_5\text{O}_9\text{Cl}$ ($x=0.01$)

4.3 Results

4.3.1 Optical properties of Ce^{3+} in $\text{Sr}_2\text{B}_5\text{O}_9\text{Br}$ and $\text{Sr}_2\text{B}_5\text{O}_9\text{Cl}$.

Monovalent cations K^+ or Na^+ are commonly used co-dopants to provide charge-compensation for trivalent rare-earth ions on divalent cations sites. The emission spectrum of $\text{Sr}_{2(1-x)}\text{Ce}_x\text{Na}_x\text{B}_5\text{O}_9\text{Br}$ ($x=0.01$) upon X-ray excitation results in a resolved Ce^{3+} emission doublet at 330 and 350 nm (Figure 4.2, curve b). The replacement of bromine by chlorine leads to a shift of Ce^{3+} emission in $\text{Sr}_{2(1-x)}\text{Ce}_x\text{Na}_x\text{B}_5\text{O}_9\text{Cl}$ ($x=0.01$) towards shorter wavelength (Figure 4.2, curve a). The band in the emission spectrum of $\text{Sr}_{2(1-x)}\text{Ce}_x\text{Na}_x\text{B}_5\text{O}_9\text{Cl}$ ($x=0.01$) (Figure 4.2, curves a) between 280-303 nm might be due to SrB_4O_7 which is present in the sample as a phase impurity. The emission band due to the $5d-2F_{5/2}$ transition in Ce^{3+} in strontium tetraborate has a maximum at 293 nm [6].

The excitation spectra of Ce^{3+} emission in chlorides and bromides are shown in Figure 4.3. Time resolved excitation spectrum of $\text{Sr}_{2(1-x)}\text{Ce}_x\text{K}_x\text{B}_5\text{O}_9\text{Br}$ ($x=0.001$) emission at 350 nm

has been recorded under synchrotron radiation at 12 K. In the short time excitation spectrum the five dominant bands with maxima at 223, 243, 268, 280 and 315 nm are attributed to the transitions to the five levels of the 5d Ce^{3+} configuration. In addition, two low intensity bands are located at 165 and 202 nm. The origin of the band at 165 nm (7.5 eV) can be attributed to the host excitation, since the typical band gap energy of borates is about this value [7-9].

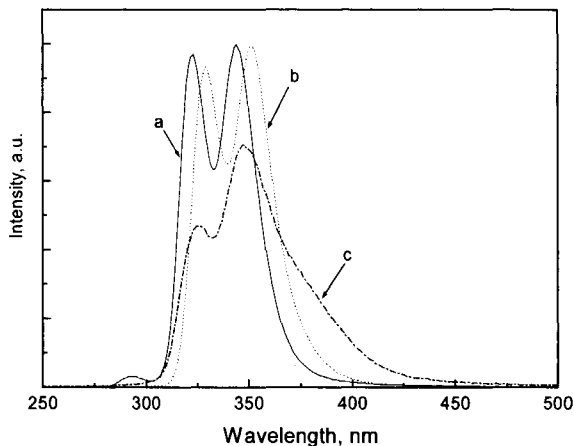


Figure 4.2: X-ray excited emission spectra of $Sr_{2(1-x)}Ce_xNa_xB_5O_9Cl$ ($x= 0.01$) (curve a), $Sr_{2(1-x)}Ce_xNa_xB_5O_9Br$ ($x= 0.01$) (curve b) and $Sr_{2(1-x)}Ce_xB_5O_9Cl$ ($x=0.01$) (curve c) recorded at room temperature.

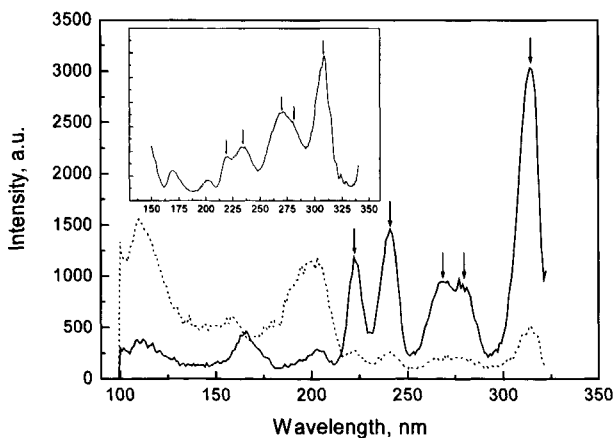


Figure 4.3: Excitation spectra of 350 nm emission of $Sr_{2(1-x)}Ce_xK_xB_5O_9Br$ ($x= 0.001$) recorded under synchrotron radiation at 12 K in short time (solid curve) and time delayed (dotted curve) mode. In the inset the excitation spectrum of 350 nm emission of $Sr_{2(1-x)}Ce_xNa_xB_5O_9Cl$ ($x=0.01$) recorded at room temperature is shown. The arrows indicate the positions of Ce^{3+} 5d bands.

In the time delayed excitation spectrum the intensity of the band at 202 nm is dominant. This evidences that this band is not related to the 5d configuration of Ce^{3+} . The excitation spectrum of $Sr_{2(1-x)}Ce_xNa_yB_5O_9Cl$ ($x=y=0.01$) has been recorded at room temperature using the VUV-spectrofluorometer. The excitation spectrum consists of the expected five bands of the 5d Ce^{3+} configuration with maxima at 219, 234, 270, 279 and 308 nm and two additional bands at 170 and 202 nm, see the inset of Figure 4.3. The positions of the 5d excitation bands of Ce^{3+} in haloborates do not change whether K^+ or Na^+ is the monovalent co-dopant.

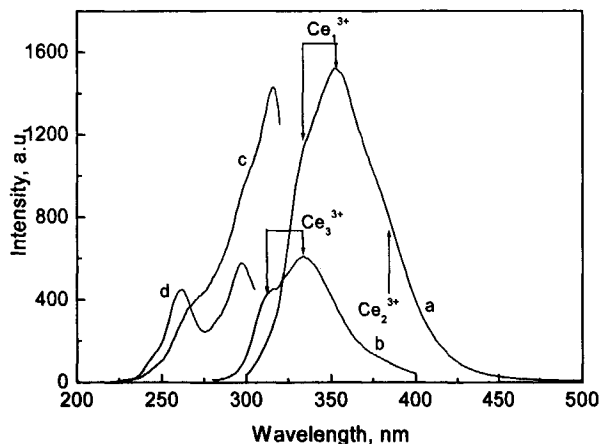


Figure 4.4: Emission spectra of $Sr_{2(1-x)}Ce_xB_5O_9Br$ ($x=0.01$) recorded at $\lambda=315$ nm (curve a) and $\lambda=260$ nm (curve b) excitation. Excitation spectra of emission at $\lambda=350$ nm (curve c) and $\lambda=315$ nm (curve d). All the spectra are recorded at room temperature.

Various types of Ce^{3+} emission centres in compounds where Ce^{3+} substitutes for a divalent cation without additional co-dopants are expected due to different charge compensation mechanisms [10]. Excitation and emission spectra of Ce^{3+} in $Sr_{2(1-x)}Ce_xB_5O_9Br$ ($x=0.01$) are shown in Figure 4.4. Two non-resolved emission bands at 330 and 352 nm observed under excitation at 315 nm are indicated as Ce_1^{3+} centre emission. This Ce_1^{3+} emission doublet is well resolved at 325 and 347 nm in the X-ray excited emission spectrum of $Sr_{2(1-x)}Ce_xB_5O_9Cl$ ($x=0.01$). The position of the lowest 5d-level of Ce_1^{3+} centres is the same as that of Ce^{3+} centres in co-doped compounds. Another broad emission band appears at about 375 nm under X-ray or photo-excitation and is indicated as Ce_2^{3+} centre emission in Figure 4.4. The intensity of this long wavelength emission increases with increase of Ce^{3+} concentration. In the sample with 0.05 mol% of Ce^{3+} it has a very low intensity upon X-ray and photo excitation at 315 nm, but the doublet at 330 and 352 nm is well resolved. It was not possible to resolve the 5d-excitation bands of these Ce_2^{3+} centres with synchrotron radiation at 12 K.

Probable charge compensation mechanisms, which occur when a trivalent ion is introduced on a divalent site, can be performed by the creation of one vacancy at a strontium site per two Ce^{3+} ions or by an oxygen on a bromine site [3]. Usually Ce^{3+} centres with nearby charge compensators produce the emission at longer wavelength than isolated Ce^{3+}

centres [11]. We therefore attribute the emission band at 375 nm to Ce^{3+} centres with nearby charge compensating defects.

A weak emission, see curve b in Figure 4.4, with the resolved doublet at 315 and 334 nm has been detected at excitation with $\lambda=260$ nm. This emission is associated with Ce_3^{3+} centres. This luminescence is not observed in all studied samples. When the sample showing the luminescence at 315 and 334 nm is fired in a very dry nitrogen atmosphere at 500 °C for 1.5 hour this luminescence disappears completely. This provides an argument that the luminescence at 315 and 334 nm is caused by Ce^{3+} centres associated with OH groups replacing the Br⁻ ions, i.e., this luminescence is a result of slow hydrolysis in air.

4.3.2 EPR spectra of Ce^{3+} ions

Figure 4.5 displays EPR spectra of $Sr_2B_5O_9Br:Ce^{3+},K^+$ taken at 9 and 20 K. Both spectra exhibit a resonance at magnetic field $B=1578$ G, which can be assigned to the presence of Fe^{3+} ions [12]. The narrow lines at $B=2035$ and 2180 G, as well as the broad band at $B=4380$ G, are clearly seen at 9 K but are absent at 20 K. It is known that Ce^{3+} ions are usually difficult to detect at temperatures above 30 K because of the strong spin-orbit coupling and the short relaxation time of the lower $4f^1$ state [13]. This gives us grounds to attribute these ESR lines to the Ce^{3+} centres.

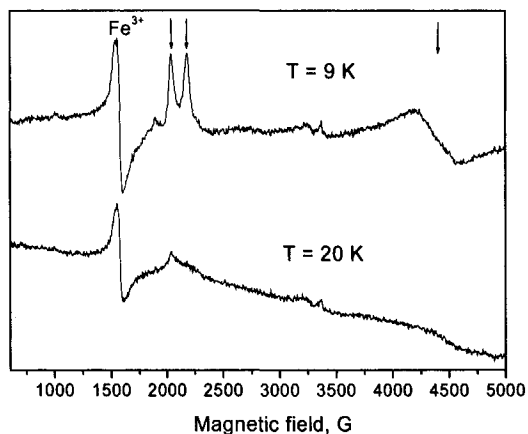


Figure 4.5: ESR spectra of an $Sr_2B_5O_9Br:0.1\% Ce^{3+},0.1\% K^+$ sample measured at 9 and 20 K. The arrows identify lines corresponding to Ce^{3+} centres.

The falloff in the 20 K EPR spectrum observed for $B > 2200$ G (Figure 4.5) is due to the Ce^{3+} resonance being broadened as a result of spin-lattice relaxation. The nuclear spin of all stable Ce isotopes is zero, and, therefore, there is no hyperfine structure. The g-tensor components corresponding to the Ce^{3+} ions occupying low symmetry crystallographic positions have been obtained earlier for $YAlO_3$ (3.162, 0.402, 0.395) [14], barium-strontium niobate (3.55, 0.89, 0.54) [15], and $LaCl_3$ (4.037, 0.23, 0.23) [16], i.e., for crystals where Ce^{3+} ions sit at sites with C_{3h} symmetry. For all these systems, the first component of the g tensor is considerably larger than the others. Because some components of the g tensor can be very small, the corresponding EPR lines may not fit within the span on the abscissa axis in Figure

4.5. This suggests that the two narrow EPR lines in Figure 4.5 are related to the first g-tensor components (with $g_1 = 3.32$ and 3.16) of Ce^{3+} centres in two different crystallographic positions shown in Figure 4.1. The EPR lines corresponding to the second g-tensor component are indistinguishable for the different Ce^{3+} positions, and this accounts for the broad band with $g_2 = 1.54$.

The effect of cerium ion concentration on the EPR spectra of $Sr_2B_5O_9Br:Ce^{3+}$ is illustrated in Figure 4.6. The signals due to Fe^{3+} ions are seen to have approximately the same intensity for all the samples studied. An increase of Ce^{3+} content in the samples is accompanied by a corresponding increase in the EPR line intensity with g_1 of 3.32 and 3.16. This relation supports the conclusion that it is the Ce^{3+} ions that are responsible for these resonances. At the same time, a broad resonance line with $g \sim 3.6$ appears in the EPR spectra at 9 K of samples with a high Ce^{3+} concentration. This resonance is not observed at 20 K. As shown in 4.3.1, an increase in Ce^{3+} concentration leads to an increase in the contribution to the total luminescence intensity from Ce^{3+} centres with local charge compensation. At a low Ce^{3+} concentration (0.05 mol %), there is no band with $g \sim 3.6$, which may indicate the presence of isolated Ce^{3+} centres only. The latter conjecture correlates with the results of the optical study presented above. Because the intensity of the EPR line with $g \sim 3.6$ grows with increasing Ce^{3+} centre concentration, we can assign this line to the first g-tensor component of Ce^{3+} ions with local charge compensation.

As for the narrow ESR line in $Sr_2B_5O_9Br:1\%Ce^{3+}$ with $g \sim 3.94$, it can likewise be related to the Ce^{3+} centres.

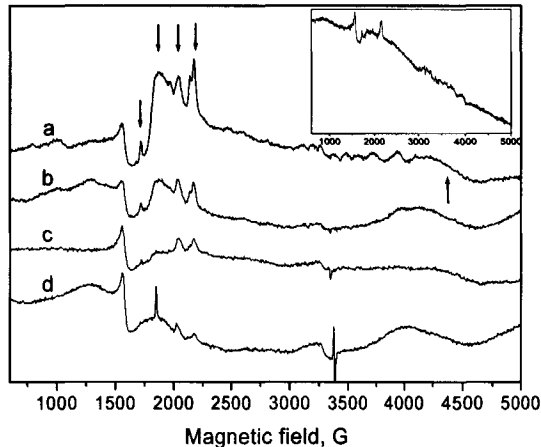


Figure 4.6: The experimental EPR spectrum recorded at 9 K of $Sr_2B_5O_9Br$ doped with different concentrations of Ce^{3+} : (a) – 1 mol%, (b) – 0.5 mol%, (c) – 0.2 mol%, (d) – 0.05 mol%. Arrows indicate the lines attributed to Ce^{3+} . In the inset the EPR spectrum of $Sr_2B_5O_9Br:1\%Ce^{3+}$ recorded at 20 K is shown.

4.3.3 Thermoluminescence

The TL glow curves of $Sr_2B_5O_9Br$ with different concentrations of Ce^{3+} ions are shown in Figure 4.7. For all Ce^{3+} concentrations there are two main TL glow peaks and the positions of these peaks do not change with concentration. The integral intensity of TL signal increases with increasing Ce^{3+} concentration up to 2 mol% as is shown in the inset.

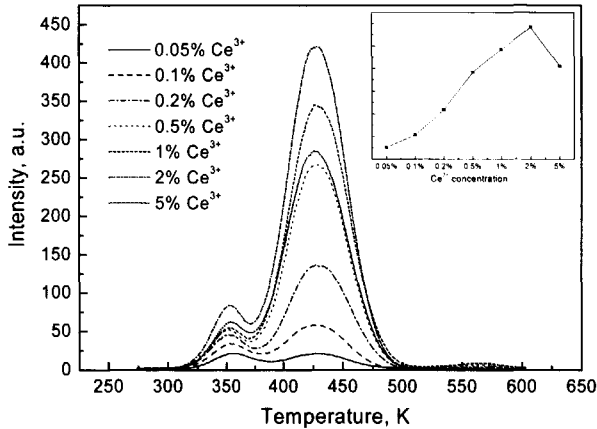


Figure 4.7: TL glow curves of $Sr_2B_5O_9Br:Ce^{3+}$ for different concentrations of Ce^{3+} . Heating rate is $\beta=1$ K/s. In the inset the integral TL intensity as a function of Ce^{3+} concentration is plotted.

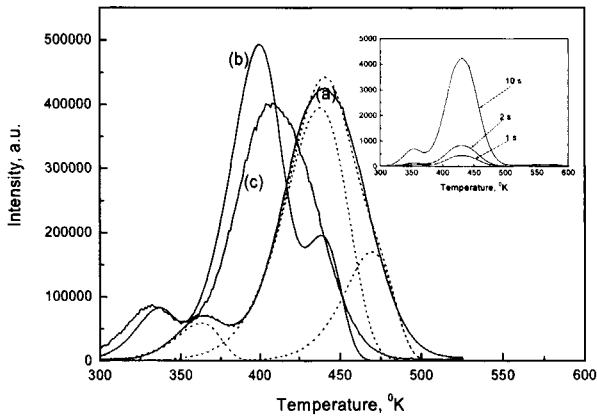


Figure 4.8: The TL glow curve (curve a) of $Sr_{2(1-x)}Ce_{2x}B_5O_9Br$ ($x=0.01$) recorded with the heating rate of 1 K/s. Dashed curves correspond to approximation of TL glow curve (a) with 3 first order TL peaks. Curve (b): calculated TL glow curve based on fitting parameters of curve (a), corresponding to the heating rate of 0.1 K/s. Curve (c): The TL glow curve recorded with 0.1 K/s heating rate. In the inset the TL glow curves of $Sr_{2(1-x)}Ce_{2x}B_5O_9Br$ ($x=0.01$) recorded after different irradiation doses.

The intensity ratio between low and high temperature peak changes with the Ce^{3+} concentration. The positions of both TL peaks do not change with absorbed radiation dose, which is consistent with a first order kinetics as described by the Randall-Wilkins equation [17]. Physically it is a case of negligible retrapping of carriers during the thermal stimulation. However the symmetrical shape of the peak at 430 K is not consistent with the first order kinetics. The assumption that the TL curve of $\text{Sr}_2\text{B}_5\text{O}_9\text{Br}:1\%\text{Ce}^{3+}$ is composed of several first orders TL peaks has been made. The TL curve has been fitted well with three first order kinetics peaks in the region between 300 and 500 K (Figure 4.8). The consistence of this mathematical fit with the real physical processes occurring during thermal stimulation has been checked by changing the heating rate during the TL measurements. Observed results show a large contradiction between experimental and fitted data. Such a contradiction means that none of the peaks at 430 K can represent a composition of several first order peaks. Most of the functions describing TL glow curves consider the trap depth associated with the defect to be a single-value in energy, i.e., an ideal case. However, the activation energy of trapped charges is distributed continuously within a certain range. This implies a significant complication of the mathematical modelling of TL kinetics. We did not perform any further attempts of TL glow curves fitting.

The influence of monovalent cations, Na^+ or K^+ on TL glow curves of $\text{Sr}_2\text{B}_5\text{O}_9\text{Br}(\text{Cl}):\text{Ce}^{3+}$ is shown in Figure 4.9. The TL intensity increases approximately by a factor of 2 when Na^+ is introduced. Monovalent co-dopants do not influence the shape of TL glow curve and peak positions. However, the intensity of the low temperature peak relative to that at high temperature is much higher in the presence of co-dopants. If one compares the TL glow curves of bromides and chlorides, the position of the low temperature peak does not depend on the ligand anion (Cl^- or Br^-). The position of the high temperature peak is shifted towards lower temperature in the case of chlorides.

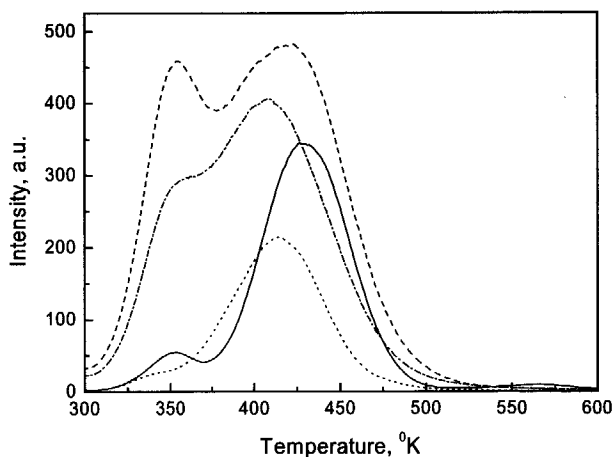


Figure 4.9: The TL glow curves of $\text{Sr}_{2(1-x)}\text{Ce}_x\text{B}_5\text{O}_9\text{Br}$ ($x=0.01$) (solid curve), $\text{Sr}_{2(1-x)}\text{Ce}_x\text{Na}_x\text{B}_5\text{O}_9\text{Br}$ ($x=0.01$) (dashed curve), $\text{Sr}_{2(1-x)}\text{Ce}_x\text{B}_5\text{O}_9\text{Cl}$ ($x=0.01$) (dotted curve), $\text{Sr}_{2(1-x)}\text{Ce}_x\text{Na}_x\text{B}_5\text{O}_9\text{Cl}$ ($x=0.01$) (dashed-dotted curve) recorded with 1K/s heating rate.

4.3.4 Emission spectra upon thermal stimulation

The structure of a TL glow curve gives the possibility to determine the characteristics of various traps. To know the features of luminescence centres the TL emission spectra should be measured. Emission spectra recorded at different temperatures during TL readout are shown in Figure 4.10. Emission related to the TL peak at 350 K in $Sr_{2(1-x)}Ce_{2x}B_5O_9Br$ ($x=0.01$) coincides with the emission of Ce_1^{3+} centres. But the emission related to the TL peak at 430 K is shifted towards longer wavelength and resembles the superposition of the emissions from Ce_1^{3+} and Ce_2^{3+} centres. The emission spectra of co-doped compounds measured near the low and high temperature TL peaks are very slightly different.

The TL emission as a function of the Ce^{3+} concentration and the type of co-dopant has been further investigated. TL measurements were performed with different band pass filters U-340 and HA-3. When the U-340 filter is placed between sample and PMT, the long wavelength emission of Ce_2^{3+} centres is absorbed. With HA-3 filter all types of Ce^{3+} emission are transmitted. The ratio of TL signals measured with the two filters, i.e. TL_{HA-3}/TL_{U-340} is a measure for the contribution of the long wavelength emission to the total TL signal. The results are listed in Table 4.1. The ratio TL_{HA-3}/TL_{U-340} increases with increase of Ce^{3+} concentration. In compounds co-doped with Na^+ or K^+ the TL_{HA-3}/TL_{U-340} ratio is smaller than that for the sample with the same concentration of Ce^{3+} but without co-doping.

Table 4.1: Integral intensity of TL signal and its dependency on the filter used. The fifth column represents the attenuation of the emission light from the sample passing through the U-340 filter, i.e. the contribution of the long wavelength Ce_2^{3+} emission to the total emission spectrum

Compound	Concentration of dopants	TL intensity HA-3	TL intensity U-340	TL_{HA-3}/TL_{U-340}
$Sr_2B_5O_9Br:Ce^3$	0.05%	2.6	1.3	1.9
	0.1%	5.3	2.3	2.3
	0.2%	10.9	4.3	2.5
	0.5%	19.2	6.0	3.2
	1%	24.3	6.5	3.8
	2%	29.2	5.6	5.2
	5%	20.6	3.6	5.7
$Sr_2B_5O_9Br:Ce^{3+},Na^+$	0.1%,0.1%	20.5	8.1	2.5
	1%,1%	61.5	23.0	2.7
$Sr_2B_5O_9Br:Ce^{3+},K^+$	0.1%,0.1%	55.6	25.3	2.2

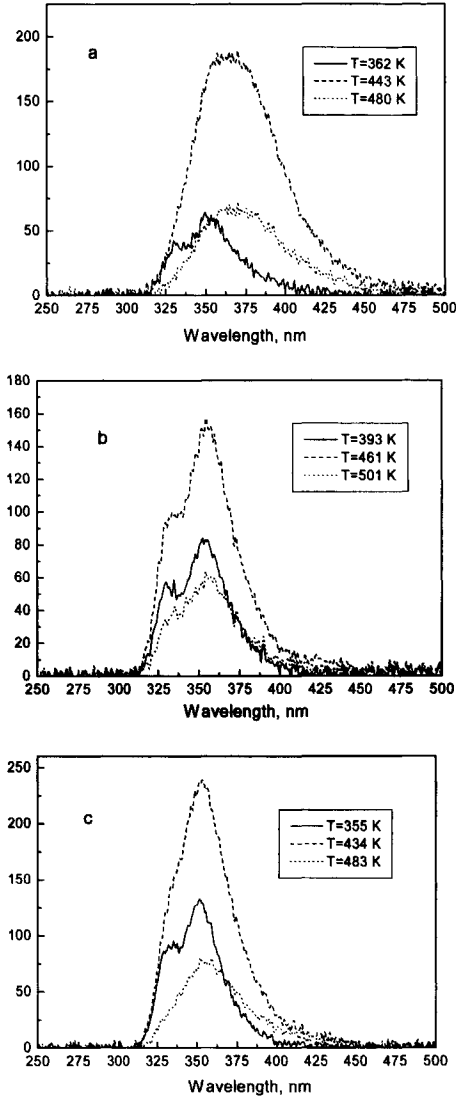


Figure 4.10: TL emission spectra of $Sr_{2(1-x)}Ce_{2x}B_5O_9Br$ ($x=0.01$) (a), $Sr_{2(1-x)}Ce_xK_xB_5O_9Br$ ($x=0.001$) (b), $Sr_{2(1-x)}Ce_xNa_xB_5O_9Br$ ($x=0.01$) (c). Measurements have been performed with 1K/s heating rate after received dose of 1kGy with ^{60}Co gamma source. The temperatures at which emission spectra have been taken are given

4.4 Discussions

The relative positions of Ce^{3+} 5d levels are very similar in bromo- and chloroborates, as can be seen in Figure 4.3. Since the relative positions of 5d levels are strongly determined by the shape and size of anion coordination polyhedron, this confirms that the polyhedral coordination of Ce^{3+} is practically the same in both compounds. The energy of the lowest 5d level in chloroborates is at 32470 cm^{-1} against 31745 cm^{-1} for bromoborates. The difference of 720 cm^{-1} is practically the same as the difference between the average energy, i.e. centroid shift of the 5d configuration, which is 12480 cm^{-1} for $\text{Sr}_2\text{B}_5\text{O}_9\text{Cl}$ and 13115 cm^{-1} for $\text{Sr}_2\text{B}_5\text{O}_9\text{Br}$.

Morrison [18] and Aull and Jenssen [19] developed a model in order to explain the behavior of the centroid shift of the 5d configuration of Ce^{3+} ions in fluorides. According to this model the shift is proportional to α/R^6 , where α is the polarizability of the ligands and R is the metal-ligand distance. The ligand polarization model was further developed by Dorenbos in [20,21] and applied to interpret the centroid shift in fluorides, chlorides, bromides and oxide compounds. Generally, a larger polarizability of bromine ions as compared to chlorine ions leads to larger centroid shift. If one takes the crystallographic data on strontium haloborates, the difference in mean strontium to oxygen distances in bromo- and chloroborates raised to the power six would be too small to explain the observed difference in centroid shift. But in real situation there could be significant difference in relaxation of ligands around trivalent cerium ion substituted for a smaller divalent strontium ion in bromo- and chloroborates. Therefore, the observed difference in centroid shifts, which amounts to 720 cm^{-1} appears to be too small to apply the ligand polarization model.

The formation of $(\text{Ce}_{\text{Sr}}\text{-K}_{\text{Sr}})$ complexes during the co-doping was considered in [3]. Adding a monovalent cation enhances the solubility of Ce^{3+} ions in the matrix and does not require additional charge compensation. That is why the EPR spectrum of $\text{Sr}_2\text{B}_5\text{O}_9\text{Br}:\text{Ce}^{3+},\text{K}^+$ consists only of the lines corresponding to the two Ce^{3+} crystallographic positions. The values of the first g-tensor components of these Ce^{3+} centres are practically identical to those of isolated Ce^{3+} ions in samples not subjected to monovalent co-doping. The small effect of the co-dopant (the K^+ ion) should be attributed either to the two neighbouring Sr^{2+} ions being separated by B_2O_9 networks or to the K^+ ions occupying a site not adjacent to the Ce_{Sr} position.

In some compounds like SrB_4O_7 and CaSO_4 two different Ce^{3+} emission centres have been found [11,22]. Centres with the largest redshift were attributed to Ce^{3+} ions with nearby charge compensation – strontium vacancy. Another possibility for charge compensation in $\text{Sr}_2\text{B}_5\text{O}_9(\text{Br},\text{Cl}):\text{Ce}^{3+}$ can be an oxygen in a bromine site next to Ce^{3+} . In this case the higher intensity of the long wavelength emission for the sample synthesised in air than in nitrogen atmosphere is expected. But the emission at 375 nm of $\text{Sr}_2\text{B}_5\text{O}_9\text{Br}:0.3\%\text{Ce}^{3+}$ sample synthesised in air has lower intensity than that of $\text{Sr}_2\text{B}_5\text{O}_9\text{Br}:1\%\text{Ce}^{3+}$ synthesised in nitrogen atmosphere. Our optical measurements did not succeed in resolving the 5d-excitation level structure of the Ce_2^{3+} centres with neighbouring charge compensating defect into individual components even at 12 K.

The EPR band with $g_1 \sim 3.6$ is seen in samples without monovalent co-doping. It was attributed to the Ce^{3+} centres whose additional charge is compensated by neighbouring defects. This resonance is broader than that observed in the case of isolated Ce_1^{3+} centres.

This implies that charge compensation may occur through more than one mechanism. Thus, the EPR band with $g_1 \sim 3.6$ and the long wavelength optical emission band are actually superpositions of contributions from several Ce^{3+} centres with different kinds of local charge compensation defects.

The Ce^{3+} emission doublet at 315 and 334 nm detected in $Sr_2B_5O_9Br$ (see Figure 4.4) was assumed to originate from Ce^{3+} with nearby OH-groups in halogen site. The shift of this Ce_3^{3+} emission towards shorter wavelength is consistent with the ligand polarization model, since polarizability of OH-groups is smaller than that of Br or Cl ions and thus the centroid shift of Ce_3^{3+} levels is expected to be smaller [21]. However the 5d configuration of Ce_3^{3+} centres must be known to base this conclusion more firmly.

The probability that a charge-compensating defect is placed near a Ce^{3+} site becomes higher with an increase of Ce^{3+} concentration. The assumption that the emission at 330 and 350 nm is caused by Ce_1^{3+} ions without nearby charge compensators then seems to be reasonable, since this emission is dominating upon X-ray and optical excitation of Ce^{3+} doped samples with very low concentrations (0.05% and less). X-ray and optically excited emission measurements show that the contribution to the total light output from long wavelength emission, i.e. Ce_2^{3+} centres with nearby charge compensatory increases with the concentration of Ce^{3+} ions.

Two types of Ce^{3+} emission centres have been detected in TL emission spectra of $Sr_2B_5O_9Br:Ce^{3+}$. Only the emission from Ce_1^{3+} centres, i.e. locally uncompensated Ce^{3+} ions, gives rise to the TL peak at 350K. The emission spectrum corresponding to the second TL peak at 430 K is the superposition of two types of Ce_1^{3+} and Ce_2^{3+} emissions. It is seen in Figure 4.7 that the intensity of this glow peak increases significantly with concentration of Ce^{3+} . Also the contribution to TL signal from Ce_2^{3+} centres grows with Ce^{3+} concentration (see Table 4.1), which is the result of a larger number of Ce_2^{3+} centres than of Ce_1^{3+} centres at high concentrations.

4.5 Conclusions

The two strontium sites in $Sr_2B_5O_9Br$ have very similar anion coordination polyhedra. Using optical spectroscopy we could not distinguish two Ce^{3+} sites. At the same time the EPR lines from Ce^{3+} centres in two crystallographic positions are very well distinguishable.

Two types of Ce^{3+} centres have been detected in $Sr_2B_5O_9(Br,Cl):Ce^{3+}$ and they can be associated with isolated Ce_1^{3+} and charge compensated Ce_2^{3+} centres. Several kinds of charge compensation defects are responsible for the Ce_2^{3+} emission. Only one type of Ce^{3+} emission centre was detected in the samples co-doped with Na^+ or K^+ . The emission is the same as that of the isolated Ce_1^{3+} centres. Two peaks appear in TL glow curves at 350 and 430 K for both co-doped and non-co-doped samples. The relative intensity of the peak at 350 K is higher in the case of co-doping. Also the integral TL intensity doubles when monovalent cations are introduced. The TL emission of $Sr_2B_5O_9(Br,Cl):Ce^{3+}$ related to the low temperature peak originates from (Ce_1^{3+}) centres. The emission in the 430 K peak is from both Ce_1^{3+} and Ce_2^{3+} centers. The TL emission corresponding to both TL peaks in co-doped samples originates from the only one type of Ce^{3+} centre.

References

- [1] Meijerink A., Blasse G., J. Phys. D: Appl. Phys. **24** (1991) 626
- [2] Knitel M. J. *et al.*, Nucl. Instr. And Meth. A **449** (2000) 595
- [3] Dotsenko V. P. *et al.*, J. of Lumin. **93** (2) (2001) 137
- [4] Machida K., Ishino T., Adachi G., Shiokawa J, Mater. Res. Bul. **14** (12) (1979) 1529
- [5] Shannon R. D., Acta Cryst. A **32** (1976) 751
- [6] Meijerink A., Blasse G., J. of Lumin. **43** (1989) 283
- [7] French R H. *et al.*, Phys. Rev. B **44** (16) (1991) 8496
- [8] Efrayushina N. P. *et al.*, Rad. Meas. **33** (5) (2001) 755
- [9] Knitel M. J. *et al.*, Nucl. Instr. And Meth. A **443** (2000) 364
- [10] Hayes W., *Crystal with the Fluorite Structure*, Clarenton Press, Oxford, 1974
- [11] Verwey J. W. M., Dirksen G. J., Blasse G., J. Phys. Chem. Solids **53** (3) (1992) 367-375
- [12] Bishay A., Quadros C. and Piccini A., Phys. Chem. Solids, **15** (4) (1974)
- [13] Abragam A. and Bleaney B., *Electron Paramagnetic Resonance of Transition Ions*, Clarendon Press, Oxford (1970)
- [14] Asatryan H. R., Rosa J. and Mares J. A., Solid State Comm, **104** (1) (1997) 5
- [15] Wingbermhle J. *et al.*, J. Phys.: Condens. Matter **12** (2000) 4277
- [16] Birgeneau R. J. and Hutchings M. T., Phys. Rev. **175** (3) (1968) 1116
- [17] Chen R. and McKeever S. W. S., *Theory of thermoluminescence and related phenomena*, World Scientific Publishing, 1997
- [18] Morrison C. A., J. Chem. Phys. **72** (1980) 1001
- [19] Aull B. F. and Jenssen H. J., Phys. Rev. B **34** (1986) 6640
- [20] Dorenbos P., Phys. Rev. B **62** (23) (2000) 15640
- [21] Dorenbos P., Phys. Rev. B **65** (2001) 125117
- [22] van der Kolk E. *et al.*, Phys. Rev. B **64** (2001) 195129



5 Complex study of radiation induced defects in $\text{Sr}_2\text{B}_5\text{O}_9\text{Br}:\text{Ce}^{3+}$ storage phosphor

5.1 Introduction

In the previous chapter we presented the optical, thermoluminescence and EPR properties of $\text{Sr}_2\text{B}_5\text{O}_9\text{X}:\text{Ce}^{3+},\text{A}^+$ ($\text{X}=\text{Cl},\text{Br}$, $\text{A}=\text{Na}^+,\text{K}^+$) phosphors. It will be shown in Chapter 6 that the storage characteristics of these phosphors are close to those required for application. That is why here we will present the results of experiments aimed at understanding the storage mechanism in haloborates. The chapter is organised as follow: first, the EPR results on irradiated pure $\text{Sr}_2\text{B}_5\text{O}_9\text{Br}$ will be presented. After that the radiation induced optical absorption spectra will be discussed. Next, the thermoluminescence and luminescence spectra of haloborates doped with different rare earth, such as Yb^{2+} and Sm^{2+} will be analysed.

The TL glow curves of haloborates doped with Ce^{3+} consist of two main peaks. The discussions of the origins of both peaks will be presented separately.

5.2 Results

5.2.1 EPR measurements on irradiated pure $\text{Sr}_2\text{B}_5\text{O}_9\text{Br}$

Before irradiation no EPR signal in pure $\text{Sr}_2\text{B}_5\text{O}_9\text{Br}$ was detected. The EPR spectra of irradiated pure $\text{Sr}_2\text{B}_5\text{O}_9\text{Br}$ recorded at 120 K just after irradiation, one day and one week after irradiation are shown in Figure 5.1. The spectrum measured just after irradiation shows the presence of at least two overlapping EPR spectra: one is the broad line with maxima at 334 and 339 mT and another one is the narrow line in the 336 to 337 mT range. Defects due to the broad EPR line are not stable at room temperature, since this line can not be observed one day after irradiation, while storing the sample at room temperature. Therefore it is possible to separate both overlapping signals. Performing measurements one day after irradiation we can assume, that only room temperature stable defects are present in a sample. From here, the discussion of EPR spectra will concern only room temperature stable defects.

In Figure 5.2 the evolution with temperature of the EPR spectra recorded one day after irradiation is shown. The shape of the lines changes dramatically with temperature. Moreover, at low temperatures an additional EPR signal at about 340 mT appears. Such a trend in EPR spectra suggests the existence of two types of paramagnetic defects with overlapping EPR spectra in the 336-340 mT range. This point will be discussed later on.

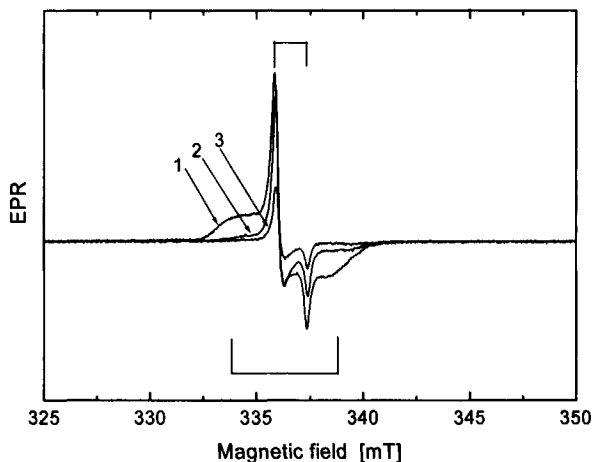


Figure 5.1: Experimental EPR spectra of X-ray irradiated pure $\text{Sr}_2\text{B}_5\text{O}_9\text{Br}$ recorded at 120 K. Each curve was recorded at different time after irradiation: 10 min (curve 1), 1 day (curve 2) and one week (curve 3) after irradiation. The “broad” and “narrow” EPR lines are indicated (see text). Between experiments the sample was kept in darkness at room temperature.

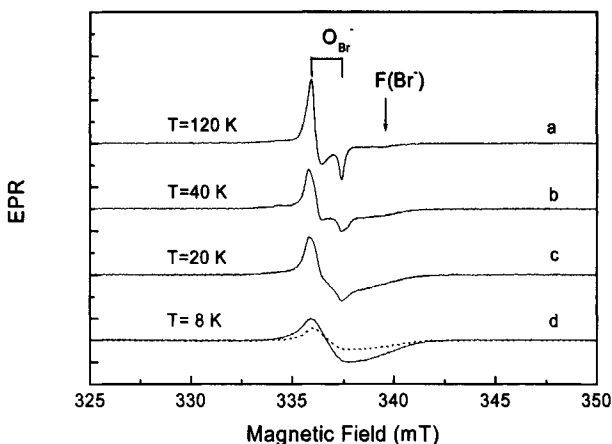


Figure 5.2: The EPR spectra of X-ray irradiated pure $\text{Sr}_2\text{B}_5\text{O}_9\text{Br}$ recorded at different temperatures. Measurements were carried out one day after irradiation. The EPR spectrum measured at 8 K one week after irradiation is shown as dotted curve. The attribution of EPR lines to $\text{F}(\text{Br})$ and O_{Br}^- is explained in the text.

5.2.2 Radiation induced optical absorption spectra of irradiated pure and Ce^{3+} doped $\text{Sr}_2\text{B}_5\text{O}_9\text{Br}$

The diffuse reflection spectra of pure and Ce^{3+} doped $\text{Sr}_2\text{B}_5\text{O}_9\text{Br}$ were measured. In Figure 5.3 and 5.4 the differences between the reflection spectra recorded prior and after irradiation are plotted. The difference between these spectra represents the radiation-induced absorption. The absorption curve of pure $\text{Sr}_2\text{B}_5\text{O}_9\text{Br}$ was fitted with two Gaussians with maxima at 365 and 560 nm as it is shown in Figure 5.3. The broad structures of these peaks must be due to polycrystalline nature of the sample [1]. It is seen from Figure 5.3 that the relative contribution to the total absorption from these two peaks is the same just after irradiation and two days after irradiation. Therefore we assume that the two bands originate from trapped hole and electron centres, created under irradiation. Thus, the ratio between the number of electron and hole centres stays constant, but part of them recombines with each other at room temperature, what leads to the decrease in total absorption in Figure 5.3. The nature of these centres will be discussed later.

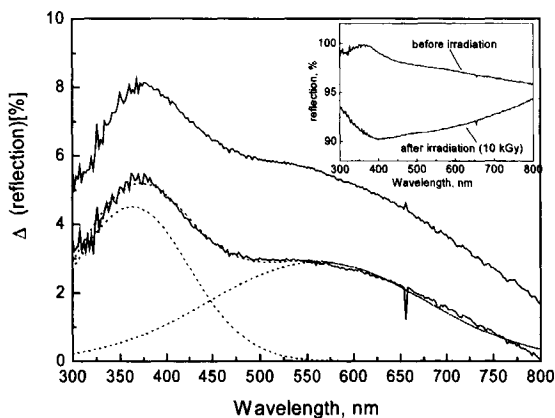


Figure 5.3: In the inset reflection spectra of pure $\text{Sr}_2\text{B}_5\text{O}_9\text{Br}$ recorded before irradiation and after irradiation (10 kGy with ^{60}Co gamma source) are plotted. The difference between them just after irradiation (upper curve) and two days after irradiation (lower curve) is plotted in the main figure. Dotted curves represent the Gaussian fit of the absorption curve measured two days after irradiation.

The treatment of reflection spectra of $\text{Sr}_2\text{B}_5\text{O}_9\text{Br}$ doped with Ce^{3+} is more complicated than in case of pure material. The measurement system is equipped with diode array for light detection and with Xenon lamp. During the measurements a sample is excited with the whole spectrum of the Xenon lamp (270-820 nm). Therefore, in reflection curves the bands due to Ce^{3+} absorption and Ce^{3+} luminescence at 330 and 350 nm are very intense. As can be seen in the inset of Figure 5.4, at a particular wavelength the reflectivity is more than 100%, which is caused by Ce^{3+} luminescence. In a spectrum obtained just by subtraction of reflection curves before and after irradiation the intense band due to Ce^{3+} luminescence is still present. It can be explained by partial absorption of Ce^{3+} luminescence in the material after irradiation. Therefore Ce^{3+} emission intensities in reflection curves measured before and after irradiation are different. Because of this an additional subtraction of Ce^{3+} emission band was done to

obtain a correct differential spectrum, and the result is shown in Figure 5.4. This spectrum was fitted with two Gaussians with maxima at 380 and 580 nm.

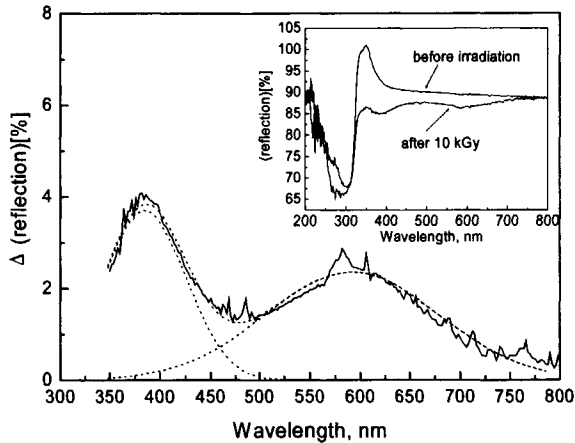


Figure 5.4: Reflection spectrum of $\text{Sr}_2\text{B}_5\text{O}_9\text{Br}:1\%\text{Ce}^{3+}$ recorded prior to irradiation minus the reflection spectrum recorded after irradiation with ^{60}Co gamma source. The received dose was 10 kGy. Below 350 nm the differential spectrum is not plotted, because of the large error caused by the presence of Ce^{3+} absorption and emission bands. The dotted curves represent a fit of the spectrum with two Gaussian peaks. In the inset reflection spectra of $\text{Sr}_2\text{B}_5\text{O}_9\text{Br}:1\%\text{Ce}^{3+}$ recorded before irradiation and after irradiation (10 kGy with ^{60}Co gamma source) are plotted.

5.2.3 Luminescence and TL of Eu, Yb and Sm doped $\text{Sr}_2\text{B}_5\text{O}_9\text{Br}$

To establish the influence of the type of rare-earth ion on TL bromoborates doped with different rare-earth ions have been synthesised.

The X-ray excited luminescence spectrum of $\text{Sr}_2\text{B}_5\text{O}_9\text{Br}:\text{Yb}$ measured at 295 K is shown in the inset of Figure 5.5. It is seen that this spectrum consists of the superposition of at least two bands with maxima at 340 and 420 nm. The Yb ions can be incorporated in $\text{Sr}_2\text{B}_5\text{O}_9\text{Br}$ as Yb^{2+} and as Yb^{3+} . The emission band at 420 nm has been attributed to the $5d \rightarrow 4f$ transitions in Yb^{2+} ions [2]. The intensity of this luminescence is reduced when the sample is fired in air. It can be due to oxidation of Yb^{2+} during the firing. The emission band at 340 nm, which intensity is increasing after oxidation, was attributed to charge transfer luminescence of Yb^{3+} ions [2]. The reduction of Yb^{2+} luminescence has been detected also after irradiation with X-rays. At the same time no increase of Yb^{3+} luminescence has been noticed. The TL curves of $\text{Sr}_2\text{B}_5\text{O}_9\text{Br}:\text{Yb}$ samples before and after oxidation are shown in Figure 5.5. The intense peak at 350 K is followed by a less intense one at 420 K. The TL emission measurement revealed that the emission corresponding to the TL peak at 350 K exhibits superposition of Yb^{2+} and Yb^{3+} luminescences. The emission spectrum corresponding to the low intensity TL peak at 420 K could not be measured due to low sensitivity of the setup.

Solid solution of $Sr_2B_5O_9Br$ doped with Eu synthesised in neutral atmosphere contains Eu^{2+} as well as Eu^{3+} ions (Figure 5.6). Emission spectra of $Sr_2B_5O_9Br:Eu$ upon X-ray irradiation exhibit the superposition of $4f^65d \rightarrow 4f^7$ transitions in Eu^{2+} and the series of transitions between $4f^n$ states in Eu^{3+} . The TL curve consists of two most intense peaks at 346 and 400 K. The emission, corresponding to these TL peaks originates only from Eu^{2+} ions.

The Sm ions are introduced in $Sr_2B_5O_9X$ as Sm^{2+} if synthesis occurs in hydrogenated atmosphere [3]. The luminescence of Sm^{2+} ions in $Sr_2B_5O_9Br$ is determined by $4f^65d \rightarrow 4f^6$ transitions. The TL curve of the irradiated $Sr_2B_5O_9Cl:Sm^{2+}$ sample represents an intense peak at about 355 K, and another one at 490 K of low intensity (Figure 5.6).

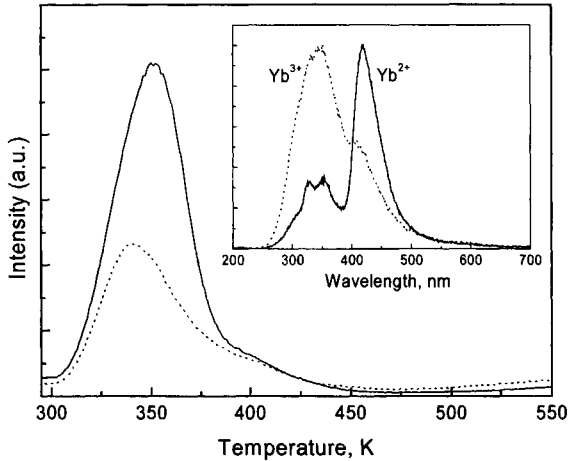


Figure 5.5: TL glow curves of β -irradiated $Sr_2B_5O_9Br:1\%Yb$: before the firing in air (solid line) and "oxidised" sample (dotted line). The heating rate is 1 K/s. In the inset the comparison of X-ray excited luminescence spectra of $Sr_2B_5O_9Br:1\%Yb$ before (solid line) and after (dotted line) firing in air is shown.

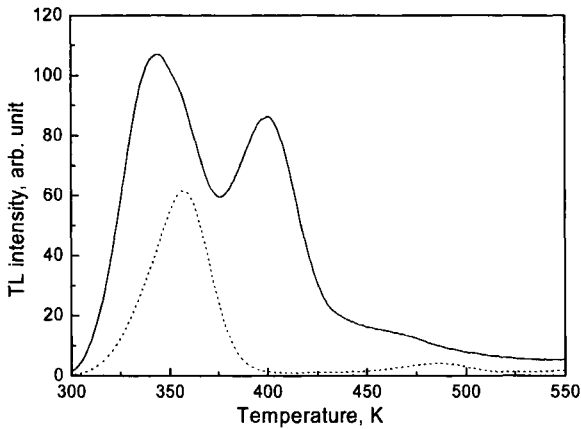


Figure 5.6: TL glow curves of β -irradiated $Sr_2B_5O_9Cl:0.2\%Sm$ (dashed line) and $Sr_2B_5O_9Cl:0.2\%Eu$ (solid line). The heating rate is 1 K/s

5.2.4 Thermoluminescence after UV-illumination

A TL response after UV-illumination has been observed in the studied materials. The band gap of $\text{Sr}_2\text{B}_5\text{O}_9\text{Br}$ is about 7.6 eV [4.3.1]. Apparently, the excitation by UV-light can not cause band-to-band transitions with subsequent creation of free e-h pairs. The TL glow curve of $\text{Sr}_2\text{B}_5\text{O}_9\text{Br}:\text{Ce}^{3+}$ recorded after illumination with photons of $\lambda=220$ nm wavelength is compared with that after β -irradiation in Figure 5.7 (upper graph). They are almost identical. The TL glow curves after illumination with photons of longer wavelength have the same structure, but their intensity decreases significantly. The intensity of the TL signal caused by illumination at $\lambda=220$ nm is several orders of magnitudes higher than that obtained from $\lambda=315$ nm illumination.

For the co-doped sample $\text{Sr}_2\text{B}_5\text{O}_9\text{Br}:\text{Ce}^{3+},\text{Na}^+$ UV illumination with photons of $\lambda=220$ nm wavelength does not create defects which are responsible for a TL peak at 350 K as seen from Figure 5.7 (lower graph). As in the case of the non-co-doped compound the total TL signal decreases when irradiation at longer wavelength is applied.

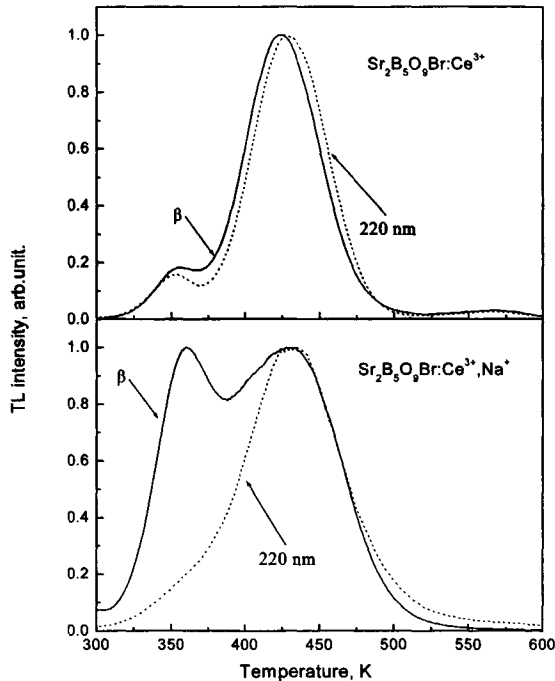


Figure 5.7: TL glow curves of $\text{Sr}_2\text{B}_5\text{O}_9\text{Br}:\text{Ce}^{3+}$ (upper graph) and $\text{Sr}_2\text{B}_5\text{O}_9\text{Br}:\text{Ce}^{3+},\text{Na}^+$ (lower graph) after illumination with UV light of $\lambda=220$ nm wavelength (dotted curves) and comparison with data from β -irradiated samples. The heating rate is 1 K/s.

5.3 Discussions

5.3.1 Room temperature stable defects and high temperature TL peak

EPR results

The EPR measurements performed at 120 K on irradiated pure $\text{Sr}_2\text{B}_5\text{O}_9\text{Br}$ showed the presence of defects, which are stable at room temperature and exhibiting the line between 335 and 338 G (Figure 5.2, curve a). This spectrum can be simulated well by assuming an axial centre with the g -values of $g_{\perp}=2.017(0)$ and $g_{\parallel}=2.008(5)$. The positive shift of g -values indicates that it is a hole centre. The absence of hyperfine interaction of the spin with boron nuclei (^{11}B has $I=3/2$ and 91.2% abundance), evidences that the hole is not trapped in borate network [4].

Based on crystal structure of haloborates two hypotheses about the nature of this defect are proposed. The first one is the creation of a V_k -centre (Br_2^- molecule). Usually V_k centres diffuse at temperatures above 120 K, and only some V_{ka} centres, i.e. V_k centres localised close to a defect or impurity can be stable at room temperature [5]. For the creation of V_k centres a high local symmetry and small distance between halogens is needed [5]. In $\text{Sr}_2\text{B}_5\text{O}_9\text{Br}$ the Br-Br distance is 5.9 Å and that is too large for creation of V_k centres.

The absence of hyperfine splitting in Figure 5.2 suggests a centre whose central element has a low abundance of magnetic isotopes. The natural abundance of ^{17}O ($I=5/2$) is just 0.038%, thus no hyperfine interaction can be observed. Oxygen is a major contaminant of alkaline-halides crystals grown in air and almost unavoidable. Hence, it is reasonably to propose the formation of an oxygen ion in a bromine site ($\text{O}_{\text{Br}^{2-}}$) during the synthesis. Such a defect has an additional negative charge and can trap a hole. The mean distance $\text{O}_{\text{Br}^{2-}}-\text{B}$ is about 4.44–4.96 Å and $\text{O}_{\text{Br}^{2-}}-\text{Br}$ distance is 5.9 Å. This is sufficiently large to prevent observation of superhyperfine interaction with neighbouring boron and bromine nuclear spin.

In Figure 5.2, curves b+d display the behaviour of the EPR spectra of pure $\text{Sr}_2\text{B}_5\text{O}_9\text{Br}$ with temperatures below 120 K. A small deviation of the EPR line from O_{Br^-} centres at 336–337 mT can be explained by a change of the local symmetry of the defect with temperature. It is difficult to determine precise g -values of O_{Br^-} centres down to 8 K because of the appearance of the additional signal at about 340 mT. This signal must be due to another kind of defect, with very fast spin-lattice relaxation above 120 K, since above this temperature it can not be observed. The EPR signal at 340 mT and higher have g values lower than g_e , and originate from electron trapped centres [1]. Therefore in the EPR spectra shown in Figure 5.2, curves b-d represent the overlapped lines from electron and hole defects. In Figure 5.2 the EPR spectra measured at 8 K in one day and one week after irradiation, while keeping the sample at room temperature are compared. The total intensity of EPR signal decreases. However the relative contribution from electron and hole trapped centres remains constant. This allows us to conclude that these electron/hole trapped centres are correlated, and at room temperature partly recombine with each other.

Optical absorption studies

The absorption energy of 365 nm (Figure 5.3) seems to be too high for $1s \rightarrow 2p$ transitions of F-centres in bromides [6]. In stead this band can be attributed to the absorption of O_{Br^-} centres. This assignment is based on three factors. First, the radiation induced EPR signal related to the O_{Br^-} centres was observed. Second, similar radiation absorption was observed in

oxygen-contaminated BaF_2 crystal, and the absorption band of O^- centres was found in UV region [7]. Finally, a very similar radiation induced absorption band at 360 nm was found in $\text{Ba}_5\text{SiO}_4\text{Br}_6:\text{Eu}^{2+}$ [8]. The only one similar radiation induced defect is obvious in $\text{Ba}_5\text{SiO}_4\text{Br}_6$ and $\text{Sr}_2\text{B}_5\text{O}_9\text{Br}$ and is not a $\text{F}(\text{Br}^-)$ centre: it is an O_{Br^-} .

Radiation induced broad optical absorption band have been observed in many oxide materials and this absorption was ascribed to hole trapped at O^{2-} centres. Attempts to explain the optical absorption of these O^- ($2p^5$) centres as the transitions between the p levels have met difficulties, since these transitions are forbidden and can not cause the observed high oscillator strength of the absorption bands [9]. Another model was proposed in [10], where the optical absorption is explained by a hole transfer from one to another O^{2-} site near the defect. This model is more plausible, since the charge transfer process is known to exhibit a broad optical absorption band [11]. Thus the absorption band at 365 nm can be caused by a hole transitions from $\text{O}_{\text{Br}^{2-}}$ to one of the 12 adjacent oxygen atoms belonging to the borate network.

If oxygen impurity is created in a bromine site during the synthesis, the anion vacancy is needed for charge compensation. After irradiation the anion vacancy can trap an electron and form F-centre. The radiation induced optical absorption band at 560 nm (Figure 5.3) can be caused by $1s \rightarrow 2p$ absorption band of $\text{F}(\text{Br}^-)$ centres. The position of the F centre absorption band reflects the distance between the anion site and the surrounding first cation coordination sphere sites. The mean Sr-Br distance in bromoborates is 3.075 Å. For example, a Na-Br distance in NaBr is 3.0 Å, and F-centre absorption band is located at 590 nm [6]. Absorption energies of F-centres due to $1s \rightarrow 2p$ transitions in alkali-bromides are about 2 eV (~ 600 nm) [6]. Therefore, it is reasonable to assume that the broad absorption band at 560 nm in Figure 5.3 is caused by $\text{F}(\text{Br}^-)$ centres.

Thus the formation of $\text{V}_{\text{Br}} + \text{O}_{\text{Br}^{2-}}$ pairs during the synthesis in pure $\text{Sr}_2\text{B}_5\text{O}_9\text{Br}$ must be proposed. Created upon irradiation $\text{F}(\text{Br}^-)$ and O_{Br^-} defects are stable at room temperature and give characteristic lines to EPR and optical absorption spectra.

The formation of the same types of defects can also be accepted in Ce^{3+} doped $\text{Sr}_2\text{B}_5\text{O}_9\text{Br}$. However, the optical absorption bands due to these defects are slightly shifted to a longer wavelength range (Figure 5.4), which can be attributed to the presence of high content of Ce^{3+} ions (1 mol %).

Origin of TL peak at 430 K in $\text{Sr}_2\text{B}_5\text{O}_9\text{Br}:\text{Ce}^{3+}$

The high temperature peak is of interest from a practical point of view, because it is stable at room temperature and gives the largest contribution to the TL signal. It is located at 430 K in Ce^{3+} doped bromoborates and at 415 K in Ce^{3+} doped chloroborates (Figure 4.9). Hence, the high temperature TL peak can be somehow attributed to the defects related to the halide anion or its vacancy.

The formation of $\text{V}_{\text{Br}} + \text{O}_{\text{Br}^{2-}}$ pairs during the synthesis in $\text{Sr}_2\text{B}_5\text{O}_9\text{Br}$ was proposed above. Created upon irradiation $\text{F}(\text{Br}^-)$ and O_{Br^-} defects are stable at room temperature. So, they are likely candidate defects responsible for the TL peak at 430 K.

The creation of O_{F^-} -anion vacancy pairs during the synthesis was also observed in stoichiometric $\text{BaFBr}:\text{Eu}^{2+}$. Moreover, there a spatial correlation between the O_{F^-} -anion vacancy pairs and the Eu^{2+} activator generated during the production of the material was found. It was also established, that the oxygen content in stoichiometric $\text{BaFBr}:\text{Eu}^{2+}$ influences the PSL and TL intensity. With use of cross-relaxation spectroscopy was shown

that irradiation produced F-centres, O_F^- centres, and Eu^{2+} activator ions are spatially correlated with each other although their local environments are regular [12].

A similar model can be accepted for the studied haloborates.

5.3.2 Low temperature TL peak

Haloborates with monovalent co-dopants

The TL glow curves of $\text{Sr}_2\text{B}_5\text{O}_9(\text{Br},\text{Cl}):\text{Ce}^{3+},\text{Na}^+$ after β -irradiation are very similar to the TL glow curves of the samples without co-doping, but the low temperature peak at 350 K is much more intense in the presence of co-doping ions (Figure 4.9). The absence of the low temperature peak in the TL glow curve of the co-doped sample after UV illumination arises the question whether the defects related to this low temperature TL peak have the same nature in materials with and without co-doping. We did not investigate this fact further, since this peak fades very fast and therefore is not of interest from the application point of view.

Haloborates without monovalent co-dopants

The TL curves of haloborates doped with different rare-earth ions, like Ce^{3+} , Yb^{3+} , Yb^{2+} , Sm^{2+} and Eu^{2+} all contain the TL peak at 350 K (Figure 4.7, 5.5 and 5.6). The TL intensity of haloborates doped with Yb, and Sm is lower than that of those doped with Ce^{3+} or Eu^{2+} ; however, the luminescence of Yb and Sm upon X-ray irradiation in this matrix is also less intense. The fact, that both, di- and trivalent rare-earth ions act as recombination centres is a strong argument that the TL peak at 350 K corresponds to intrinsic defects of the haloborate matrix. The position of this TL peak does not change with the type of ligand anion (Cl or Br) (Figure 4.9). Thus, we can conclude that any kinds of defects connected to the anion or its vacancy (i.e. in form of F centre) are not involved in charge trapping. The precursor to the charge trap can be found from EPR measurements. The broad EPR line, which can be ascribed to the hole trapping defect has been detected (Figure 5.1). These defects are not stable at room temperatures. The TL peak at 350 K also fully disappears in four hours after irradiation. Thus, it is possible to connect the broad EPR line with the defects, which are responsible for the TL peak at 350 K. However, the question about the nature of this peak is still open. If these defects are not connected to an anion or its vacancy, it must be placed in the boron-oxygen carcass. The broad EPR lines are typical for boron-oxygen-hole-centres [4]. However, no superhyperfine interaction with boron nuclei has been observed even at 4 K. Only an EPR study on the haloborate crystal can bring clarity on this point.

One question about the TL peak at 350 K remains - why do only charge uncompensated Ce^{3+} centres give rise to TL emission at 350 K? It was shown in [4.3.4] that no long wavelength emission from charge-compensated Ce^{3+} centres gives rise to the TL peak at 350 K. The charge uncompensated Ce^{3+} centres have an extra local positive charge. If we suppose that upon thermal stimulation a quasi-free electron is formed, the uncompensated Ce^{3+} centres would attract them with higher probability than locally neutral charged compensated Ce^{3+} centres. Thus, the recombination probability of electron-hole pairs on charge uncompensated centres would be much higher. A similar situation was observed in the $\text{CsBr}:\text{Ga}^+$ and $\text{RbBr}:\text{Ga}^+$ storage phosphor, where PSL active $(\text{Ga}^{2+})^1$ centres, i.e. positively charged centres without nearby cation vacancy, clearly dominate over PSL inactive $(\text{Ga}^{2+})^2$ centres, i.e. neutrally charged with a nearby cation vacancy [13]. This can also explain why only Eu^{2+} centres take part in recombination processes at 350 K. In a Eu doped sample, where Eu has been found in di- and trivalent states, free electrons are captured by Eu^{3+} ions, which is

followed by Eu^{2+} luminescence and the hole resides on Eu^{2+} centres. In an Yb doped sample a free electron can be attracted by Yb^{3+} centres, which is followed by $5d \rightarrow 4f$ transitions in Yb^{2+} ions or CT transitions of Yb^{3+} ions.

5.4 Conclusions

The EPR study on irradiated pure $\text{Sr}_2\text{B}_5\text{O}_9\text{Br}$ revealed a room temperature stable defect, which was attributed to O_{Br^-} center. The EPR signal from $\text{F}(\text{Br}^-)$ centres can be observed at temperatures below 120 K. The $1s \rightarrow 2p$ transitions of these $\text{F}(\text{Br}^-)$ centres cause the optical absorption band at 560 nm. The optical absorption band at 365 nm was attributed to O^- centres. Thus electron and hole trapping in pure $\text{Sr}_2\text{B}_5\text{O}_9\text{Br}$ occurs in V_{Br} and O_{Br^-} aggregates, which are created during the synthesis.

The EPR and radiation induced absorption measurements on Ce^{3+} doped $\text{Sr}_2\text{B}_5\text{O}_9\text{Br}$ revealed the same defects as in pure material. It is very likely that these defects take part in the processes of thermostimulated luminescence, which correspond to the high temperature peak.

References

- [1] Marfunin A. S., *Spectroscopy, Luminescence and Radiation centres in Minerals*, ch.7, Springer-Verlag, Berlin, 1979
- [2] Dotsenko V.P. *et al.*, *J. Solid State Chem.* **166** (2002) 271
- [3] Dotsenko V.P., Radionov V.N., Voloshinovskii A.S., *Mat. Chem. Phys.*, **57** (1998) 134-137
- [4] Griscom D. L., *Journal of non-crystalline solids*, **13** (2) (1974) 251
- [5] Hayes W., *Crystal with the Fluorite Structure*, Clarenton Press, Oxford, 1974
- [6] Agullo-Lopez F., Catlow C.R.A., Townsend P.D., *Point Defects in Materials*, Academic Press, 1988
- [7] Eachus R. S. *et al.*, *Phys.: Condens. Matter* **3** (1991) 9327
- [8] Schipper W J, *Luminescence and Storage Mechanism of New X-ray Storage Phosphors*, PhD thesis, ch. 6, Utrecht University, 1993
- [9] Tohver H. T., Henderson B., Chen Y. and Abraham M.M., *Phys. Rev. B.* **5** (8) (1972) 3276
- [10] Schirmer O. F., *J. Phys. Chem. Solids* **32** (1971) 499
- [11] Dorenbos P., *J. Phys.: Condens. Matter* **15** (2003) 8417
- [12] Koschnick F. K. *et al.*, *Phys. Rev Let.* **67** (25) (1991) 3571
- [13] Rogulis U. *et al.*, *J. Appl. Phys.* **87**, 207 (2000).

6 Storage properties of Ce^{3+} doped haloborate phosphors enriched with ^{10}B isotope

6.1 Introduction

In the previous two chapters the spectroscopy and thermoluminescence properties of Ce^{3+} doped haloborates were presented together with the results of other experiments providing information about the physical mechanisms responsible for the storage effect. The nature of charge trapping defects was discussed. In this chapter we consider the suitability of haloborate phosphors with the general formula $\text{M}_2\text{B}_5\text{O}_9\text{X}:\text{Ce}^{3+}$ ($\text{M}=\text{Sr}$ or Ca ; $\text{X}=\text{Br}$ or Cl) for practical application.

The chapter is organised as follows. First, yields of photostimulated luminescence (PSL) and TL upon β -irradiation for the series of studied haloborates with different anion, cation and impurity ions will be presented and characterised. Next, the PSL and TL yields of the series of haloborates with 99% enrichment of ^{10}B will be reported.

After that the PSL characteristics of several haloborates irradiated with cold neutrons and read-out with the commercial image plate BAS-scanner will be given and compared with those of the Gd-Image Plate. It will be shown that the read-out parameters of the commercial scanner are far from optimal for haloborates.

Finally, the PSL yields of ^{10}B enriched haloborates will be compared with a common mixture of $\text{BaFBr}:\text{Eu}^{2+}$ (40 wt%) and Gd_2O_3 (60 wt%) after γ - and neutron irradiation, employing optimised read-out parameters.

6.2 Experimental procedures

6.2.1 Standard TL and PSL read-out system

The measurements of thermo- and photostimulated luminescence intensities of the series of haloborates were performed by means of the Risø-TL/PSL-DA-15A/B reader with an installed $\text{Sr}^{90}/\text{Y}^{90}$ β -source with a dose rate 1.0 mGy/s in air. As photostimulation source a ring of blue emitting diodes (Blue LEDs) with $\lambda=470\pm 20$ nm was used. A set of three U-340 filters ($\lambda_p\sim 340$ nm, FWHM ~ 80 nm) with a total thickness 7 mm was employed in order to shield the PMT window from the scattered light of the stimulation source.

We compared the storage characteristic of the studied haloborates with common neutron storage phosphors using two different techniques and under different irradiation conditions.

6.2.2 Read out with the commercial BAS scanner

The first comparison was done upon irradiation with cold neutrons, i.e. $\lambda \sim 7.6 \text{ \AA}$. For irradiation samples were installed in a neutron guide N29 in the experimental hall of the ILL/EMBL nuclear reactor. The neutron beam is collimated by means of CB_4 (Figure 6.1). The neutron beam size is $1.5 \times 1 \text{ cm}^2$ and the neutron flux is about $10^8 \text{ n}\cdot\text{cm}^{-2}\cdot\text{s}^{-1}$. A significant amount of γ -rays is also present in the beam.

Several powder samples were put in an aluminium plate holder with circular wells of 200 μm deepness (Figure 6.1). The weights of the powder samples are given in Table 6.2. With the help of a gas-filled detector installed in front of the neutron beam it is possible to measure the relative neutron flux. Thus, measuring the neutron flux with and without sample in front of the detector window it is possible to know directly the amount of neutrons absorbed in the sample layer.

As a reference a commercial Fuji Neutron Image Plate (Fuji - NIP) representing a mixture of BaFBr:Eu^{2+} and Gd_2O_3 was used.

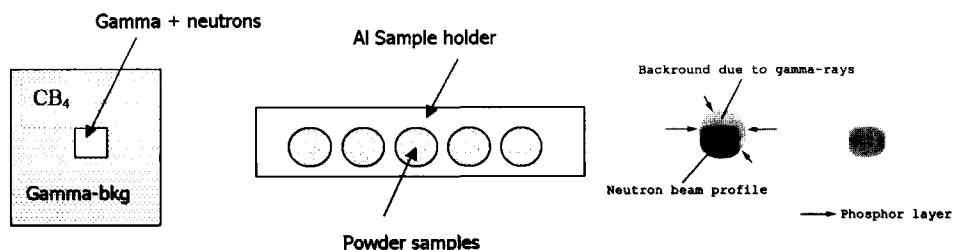


Figure 6.1: On the left: sketch of the collimator for the neutron beam and the holder for the powder sample. Irradiation is carried out sample-by-sample. On the right: Picture received by scanning the sample holder with irradiated samples: Fuji-NIP (on the left) and $\text{Ca}_2\text{B}_5\text{O}_9\text{Br:1\%Ce,Na}$ (on the right).

Read out was performed by means of a commercial BAS Image Plate scanner. It is equipped with a He-Ne laser ($\lambda=635 \text{ nm}$) as stimulation source and a band pass filter ($\lambda \sim 390 \text{ nm}$) in front of the PMT for separation of scattered laser light. The scanned images of several irradiated samples are shown in Figure 6.1. The rectangular black spot represents the neutron flux profile.

6.2.3 Read out with the Risø-PSL single-grain reader

As will be shown later, the read out parameters of the BAS Image Plate scanner are highly inefficient for haloborates. That is why the second stage of the comparative study had to be performed with optimised read-out parameters. It was also aimed at getting the real values of neutron and gamma sensitivities of haloborate phosphors and comparing them with those of a reference neutron storage phosphor. As a reference material the mixture of BaFBr:Eu^{2+} (40 wt%) with Gd_2O_3 (60 wt%) was used.

Irradiation with neutrons was performed using one of the beam lines (L21) of the IRI nuclear research reactor. The energy spectrum of the thermal neutrons is close to a Maxwell distribution with a maximum at 25 meV. The neutron flux was measured to be about $5 \cdot 10^4$

$n\cdot cm^{-2}\cdot s^{-1}$. Irradiation with γ -rays was performed by means of a ^{137}Cs source (662 keV) with a dose rate ~ 2 mGy/h.

Read out of the haloborates and $BaFBr:Eu^{2+}\times Gd_2O_3$ was performed by means of a single grain attachment to the Risø-TL/PSL reader [3.4.3]. As a photostimulation source a 10 mW Nd:YVO₄ solid state diode-pumped laser was used, emitting at 532 nm and producing a spot approximately 120 μm in diameter at the surface of the sample disc. In our PSL experiments we used 10 % of the full laser power, i.e. 1mW. Powder samples were put into the wells of 10 mm diameter in the surface aluminium disk. The depth of the well is about 300 μm . The laser beam can scan the wells in the ten by ten grid pattern giving a total of 100 pixels of photostimulated phosphor on each sample disk. Therefore, the read-out procedure is very similar to that in commercial image plate scanners.

Each pixel was read out during 2 s, and the PSL signal was recorded in a histogram of 100 channels. The value of the first channel represents the detected PSL signal in the first 20 ms of laser stimulation. The PSL yield of the studied phosphors was characterised by this value.

6.3 Results

6.3.1 TL and PSL study of haloborates with natural abundance of ^{10}B (18.8%)

The TL technique is usually used to predict the yield of the studied materials upon photostimulation. The measured TL yields of the series of β -irradiated haloborates with natural abundance of ^{10}B and different types of anions and cations as well as monovalent co-dopants are listed in column 3 of Table 6.1. All the samples exhibit a TL yield of the same order of magnitude. The TL glow curves of $Sr_2B_5O_9Br:Ce^{3+},Na^+$, $Sr_2B_5O_9Br:1\%Ce^{3+}$ and $Ca_2B_5O_9Cl:Ce^{3+},Na^+$ are shown in Figure 6.2a-c (solid curves). The intensity of the low temperature peak at 350 K relative to that at the high temperature, 400-430 K, is much higher in the presence of monovalent co-dopants.

It has been shown in [1] that haloborates doped with Eu^{2+} show a 30 times lower integral PSL yield and 30-80 times less stimulation efficiency than $BaFBr:Eu^{2+}$ upon stimulation at $\lambda=635$ nm. It has also been established that stimulation of PSL by light with shorter wavelength would enhance the stimulation efficiency of Eu^{2+} doped haloborates. The position of the emission band of Eu^{2+} luminescence in haloborates depends on the cation and ligand type and varies between 415-447 nm. Therefore, the application of a stimulation source with shorter wavelength will certainly cause a problem in the separation of the scattered stimulation light and the induced PSL.

Emission bands of Ce^{3+} luminescence in haloborates are located in the 325-360 nm region depending on cation and anion type. The so-called stimulation spectrum of photostimulated luminescence of $Sr_2B_5O_9Br:1\%Ce^{3+}$ is shown in Figure 6.3 (solid curve). The spectrum was recorded after γ -ray irradiation of the sample and detecting Ce^{3+} luminescence at 350 nm. The spectrum is almost structureless and increases monotonically with shortening of the wavelength. All the studied haloborates show a similar behaviour of the stimulation spectrum. It is seen that stimulation with the common He-Ne laser wavelength $\lambda=632$ nm is inefficient. Applying a stimulation source with shorter wavelength down to 430 nm can increase the stimulation efficiency.

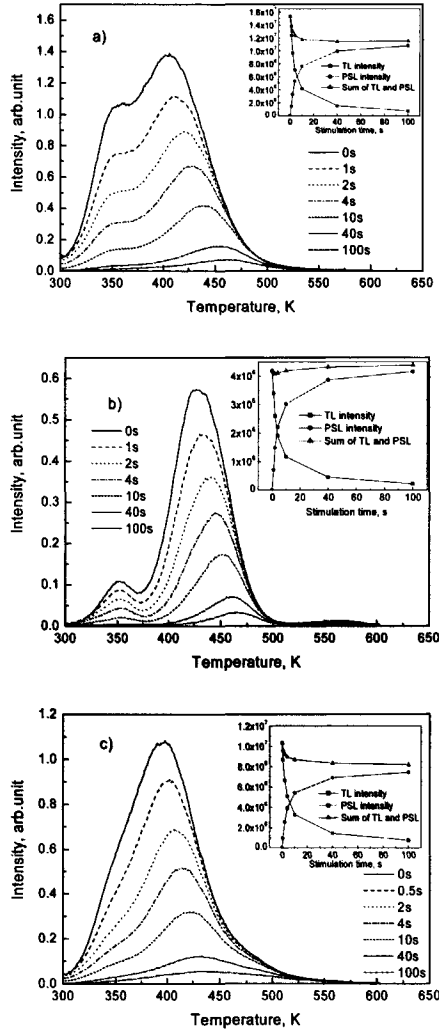


Figure 6.2: The TL glow curves of β -irradiated $Sr_2B_5O_9Cl:Ce^{3+},Na^+$ (a), $Sr_2B_5O_9Br:1\%Ce^{3+}$ (b) and $Ca_2B_5O_9Cl:Ce^{3+},Na^+$ (c), which were recorded after photostimulation of different duration – from 0 to 100 s. Blue LED's ($\lambda=470$ nm) were used as a stimulation source. The TL curves were recorded with a heating rate of 1 K/s. Irradiation was performed with $^{90}Sr/^{90}Y$ β -source. In the inset the integral intensity of the residual TL signal, PSL signal measured before TL measurements and the sum of both are plotted as a function of optical stimulation time.

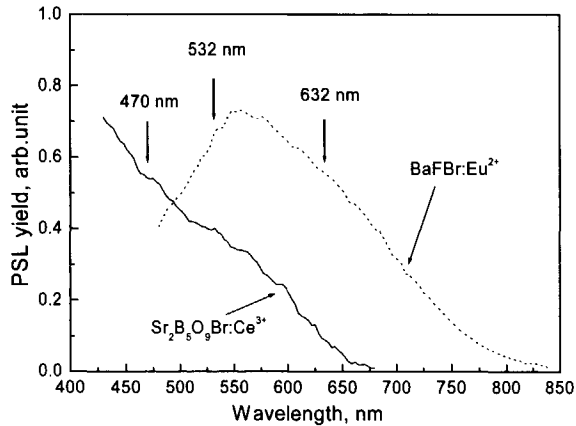


Figure 6.3: PSL stimulation spectra of $Sr_2B_5O_9Br:1\%Ce^{3+}$ (solid curve) measured at $\lambda=350$ nm emission and of $BaFBr:Eu^{2+}$ (dotted curve) measured at $\lambda=390$ nm emission. The spectra were corrected for the intensity of the xenon lamp.

Table 6.1: Summary of TL and PSL yields of investigated compounds. All the samples were measured under the same conditions. Irradiation was performed with a $^{90}Sr/^{90}Y$ β -source. The fourth column shows TL yields measured with a U-340 filter. This filter is used for PSL measurements with blue LEDs, and the fifth column represents the attenuation of the emission light from the sample passing through the U-340 filter. The sixth column shows the integral PSL signal during 20 s of photostimulation with $\lambda=470$ nm.

Compound	Conc. Mol%	Total TL intensity arb. units	TL intensity U-340 arb. units	Ratio TL/TL _{U-340}	PSL intensity arb. units
$Sr_2^{nat}B_5O_9Br:Ce^{3+}$	1%	24.3	6.5	3.8	5.8
$Sr_2^{nat}B_5O_9Br:Ce^{3+},Na^+$	1%,1%	61.5	23.0	2.7	12
$Sr_2^{nat}B_5O_9Br:Ce^{3+},K^+$	1%,1%	55.8	14.3	3.9	9.9
$Sr_2^{nat}B_5O_9Cl:Ce^{3+}$	0.5%	22.6	7.7	2.9	5.4
$Sr_2^{nat}B_5O_9Cl:Ce^{3+},Na^+$	0.5%,0.5%	47.8	26.7	1.8	15
$Ca_2^{nat}B_5O_9Br:Ce^{3+}$	1%	31.2	6.6	4.8	5.5
$Ca_2^{nat}B_5O_9Br:Ce^{3+},Na^+$	0.5%	25.8	9.3	2.8	6.5
$Ca_2^{nat}B_5O_9Cl:Ce^{3+},Na^+$	1%	31.9	14.6	2.2	9.4
$Sr_2^{10}B_5O_9Br:Ce^{3+}$	1%	-	6.7	-	3.7
$Sr_2^{10}B_5O_9Br:Ce^{3+},K^+$	1%,1%	-	7.2	-	4.8
$Sr_2^{10}B_5O_9Br:Ce^{3+},Na^+$	1%,1%	-	7.1	-	4.5
$Ca_2^{10}B_5O_9Br:Ce^{3+},Na^+$	1%,1%	-	6.2	-	3.7
$Ca_2^{10}B_5O_9Cl:Ce^{3+},Na^+$	1%,1%	-	8.3	-	6.1

In our PSL experiments as stimulation source the ring of Blue LEDs with $\lambda=470$ nm installed in the Risø reader was chosen and a pack of three U-340 cut-off filters was placed in front of the PMT. The measured TL yields with U-340 filters are listed in column 4 of Table 6.1. The degree of attenuation of a TL signal due to the mismatch of cut-off filter transmission spectrum and the TL emission spectrum is shown in column 5 of Table 6.1. For some compounds, especially with a high concentration of Ce^{3+} the use of U-340 filters cut-off a significant part of the PSL light. For example for $\text{Ca}_2\text{B}_5\text{O}_9\text{Br}:\text{Ce}^{3+}$ only one fifth part of the PSL light passes through the filter. With an increase of Ce^{3+} concentration the emission spectrum of the Ce^{3+} luminescence shifts more to the long wavelength part. The origin of this shift has been discussed in [4.3.4].

We used the TL technique to estimate the yield of PSL. However, the results of Table 6.1 show that for some samples there is a discrepancy between TL and PSL response. Especially it is pronounced for compounds co-doped with Na^+ . Different recombination processes occurring upon thermal and optical stimulation can explain this.

A combined PSL and TL technique was applied to investigate the observed differences between PSL and TL signals. The procedure of this technique is as follows. After β -irradiation the integral PSL signal was measured during a certain stimulation time. Immediately after photostimulation the residual TL glow curve was recorded. The residual TL signal is proportional to the number of trapped carriers, which were not released upon the preceding photostimulation. Varying the duration of the photostimulation time, information about efficiency of photostimulation of certain types of traps can be extracted. In Figure 6.2 the results are shown for $\text{Sr}_2\text{B}_5\text{O}_9\text{Br}:\text{Ce}^{3+},\text{Na}^+$, $\text{Sr}_2\text{B}_5\text{O}_9\text{Br}:\text{Ce}^{3+}1\%$ and $\text{Ca}_2\text{B}_5\text{O}_9\text{Cl}:\text{Ce}^{3+},\text{Na}^+$ compounds. In the insets integral intensities of PSL, TL and both PSL+TL signals are plotted versus the time of photostimulation applied before the TL measurements.

For the samples with Na^+ co-doping where the intensity of 350 K TL peak is high, the integral PSL+TL signal decreases with an increase of photostimulation time, as it is seen in insets in Figures 6.2. But after a certain stimulation time it becomes constant. We have performed the same type of experiments described above with β -irradiated samples that were annealed at 350 K, i.e., samples, in which only traps corresponding to the high temperature peak are left. In that case no decrease of integral PSL+TL signal was observed. Thus the trapped charges corresponding to the 350 K TL peak are efficiently emptied upon photostimulation, but there are non-radiative losses occur along with recombination with Ce^{3+} emission centres. Therefore only the traps, which correspond to the high TL peak appear to be active in the PSL process.

6.3.2 TL and PSL study of haloborates with enriched abundance (99%) of ^{10}B isotope

Five samples of haloborates with 99% enrichment of ^{10}B were synthesised. The TL and PSL yields of these samples were compared with those with natural abundance and the results are compiled in Table 6.1. The TL and PSL yields of the enriched haloborates are lower than those with natural abundance. Different starting materials used for synthesis can explain this. Boric acid was used for synthesis of haloborates with ^{10}B and boron oxide was used for synthesis of enriched samples. The studied samples with 99% enrichment of ^{10}B represent a "pilot" series and synthesis conditions are not yet optimised.

The results of Table 6.1 lead to the conclusion that $Ca_2B_5O_9Cl:Ce^{3+},Na^+$ is the most promising of the studied series for detection of thermal neutrons with reduced sensitivity to γ -rays, since it has the lowest Z_{eff} number and, at the same time, a relatively high PSL yield.

6.3.3 Quantitative comparison of the studied haloborates (natural abundance of ^{10}B) with Gd-IP after cold neutron irradiation and read-out with a commercial BAS-scanner

During irradiation the transmission of cold neutrons through the sample layers of 200 μm thickness was measured. The results are listed in Table 6.2. The neutron absorption efficiency is proportional to the number of ^{10}B nuclei. This value depends on the chemical composition and the amount of a compound in a sample holder. The linear absorption coefficients divided by weight fractions of the neutron absorber are given in the fifth column of Table 6.2. These values, as it follows from Equation 6.2, should be independent on the material composition.

Table 6.2: The results of neutron absorption and PSL measurements on studied samples. The amount of each material used in the experiments is shown in the second column. The measured neutron absorption efficiency, i.e. the probability for a neutron to be absorbed while passing through the sample is presented in the third column. The weight fraction (W_i) of ^{10}B nuclei in each compound was calculated. In the fifth column, the presented coefficients of neutron absorption were derived from Equation 6.2. The PSL yield in the last column was defined as an average number of counts per pixel in neutron beam profile.

Compound	Amount of a sample material W, g	Neutron absorption efficiency, P	Weight fraction of ^{10}B , W_i	$-\ln(1-P)$ / $W \cdot W_i$	PSL yield, counts per pixel
$Ca_2^{nat}B_5O_9Cl: 2\%Eu$	0.1428	0.79	0.17	63	30
$Sr_2^{nat}B_5O_9Br: 1\%Ce,K$	0.1932	0.73	0.12	56	90
$Ca_2^{nat}B_5O_9Br: 1\%Ce,Na$	0.1011	0.62	0.15	62	10
$Sr_2^{nat}B_5O_9Br: 1\%Ce,Li$	0.1515	0.66	0.12	59	12
Gd-IP (Fuji)	--	100	--	--	40000

After neutron irradiation the samples were put in the BAS scanner and read-out. The mean PSL intensities in the neutron beam profile (left picture in Figure 6.1) are listed in Table 6.2. It is seen that the haloborates exhibit very low PSL yield in comparison with Gd-IP in the given read-out conditions. Indeed, the stimulation of PSL with $\lambda \sim 630$ nm is highly inefficient (Figure 6.3). The transmission of the band-pass filter with $\lambda = 390$ nm in front of the PMT does not match the emission spectrum of Ce^{3+} in haloborates (Figure 6.4). In addition, having a sample with 100% of ^{10}B enrichment the neutron absorption and consequently the PSL yield can be increased. The quantitative comparison of ^{10}B enriched samples with commercial neutron storage phosphors under optimised read-out conditions will be given in [6.3.4]

One sample of calcium chloroborate with Eu^{2+} was measured. The PSL yield is not very much different from the samples with Ce^{3+} doping. However, haloborates with Eu^{2+} are not very promising, since PSL emission occurs at relatively long wavelength (415 - 447 nm), and consequently implementation of a stimulation source with shorter wavelength would be difficult.

6.3.4 Quantitative comparison of the studied haloborates with $\text{BaFBr:Eu}^{2+}\text{xGd}_2\text{O}_3$ after thermal neutron irradiation and read-out with the Risø-PSL single-grain reader

To perform a correct comparison between two different types of storage phosphors, the experimental conditions must be equally optimal for both of them. The read-out of BaFBr:Eu^{2+} storage phosphor is usually performed with a He-Ne laser ($\lambda=632$ nm). However, as it can be seen from Figure 6.3, the maximum of PSL excitation spectrum of BaFBr:Eu^{2+} is at 550 nm. The stimulation of haloborates is also very inefficient at $\lambda=632$ nm. For our experiment we used a Nd:YWO₄ laser with $\lambda=532$ nm, which is about optimal for both haloborates and BaFBr:Eu^{2+} .

As a cut-off filter for protection of the PMT we used a set of BG-4 and UG-1 filters. The filters transmission curves and X-ray excited emission spectra of BaFBr:Eu^{2+} , $\text{Ca}_2^{10}\text{B}_5\text{O}_9\text{Cl:Ce}^{3+},\text{Na}^+1\%$ are shown in Figure 6.4. These filters attenuate the emission from BaFBr:Eu^{2+} by a factor of 5, and the emission from $\text{Ca}_2^{10}\text{B}_5\text{O}_9\text{Cl:Ce}^{3+},\text{Na}^+$ by a factor of 2.

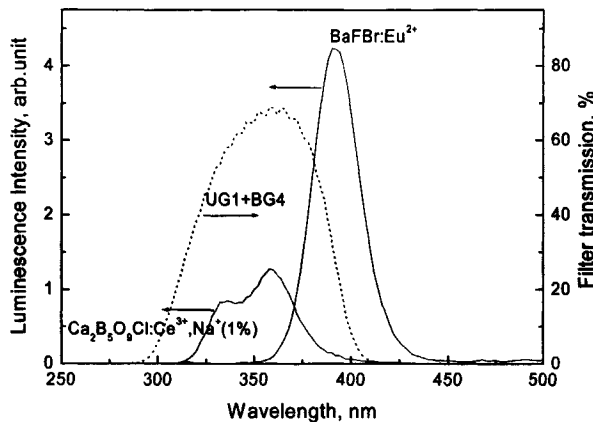


Figure 6.4: Transmission spectrum of BG4+UG1 filter (dotted curve), X-ray excited emission spectrum of BaFBr:Eu^{2+} phosphor and of $\text{Ca}_2\text{B}_5\text{O}_9\text{Cl:Ce}^{3+},\text{Na}^+$.

The typical PSL curves of $\text{BaFBr:Eu}^{2+}\text{xGd}_2\text{O}_3$ and $\text{Ca}_2^{10}\text{B}_5\text{O}_9\text{Cl:Ce,Na}$ upon continuous laser stimulation after neutron irradiation are shown in Figure 6.5. The measurements were carried out 1 hour after irradiation. The PSL signal of BaFBr:Eu^{2+} phosphor (without adding Gd_2O_3) after neutron irradiation is two orders of magnitude lower than that of $\text{BaFBr:Eu}^{2+}\text{xGd}_2\text{O}_3$ or $\text{Ca}_2^{10}\text{B}_5\text{O}_9\text{Cl:Ce,Na}$. Pure BaFBr:Eu^{2+} does not interact with thermal neutrons and the PSL signal is attributed to the γ -rays in the neutron flux.

The results of PSL experiments are collected in Table 6.3. The values represent the average of PSL signals within the first 20 ms of laser stimulation from 100 pixels in the sample disc. The mean measured PSL signals after neutron and γ -ray irradiation are denoted as S_n and S_γ . The values are corrected for the attenuation of the cut-off filters, i.e. the detected signal from $\text{BaFBr:Eu}^{2+}\text{xGd}_2\text{O}_3$ is multiplied by 5, and that from haloborates is multiplied by 2.

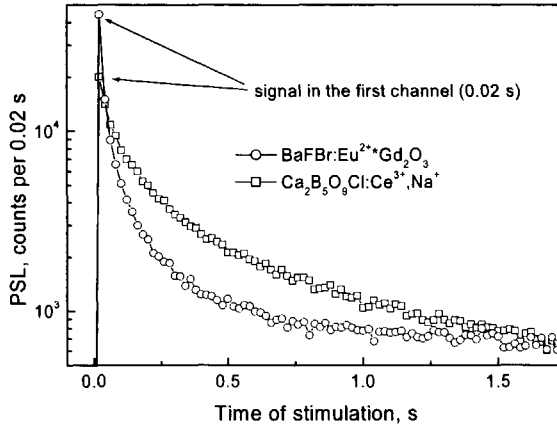


Figure 6.5: The PSL curves of $BaFBr:Eu^{2+}xGd_2O_3$ and $Ca_2^{10}B_5O_9Cl:Ce,Na$ under continuous stimulation by means of $Nd:YVO_4$ laser ($\lambda=532$ nm). Laser power is 1 mW and the beam diameter approximately 120 μm on the sample surface.

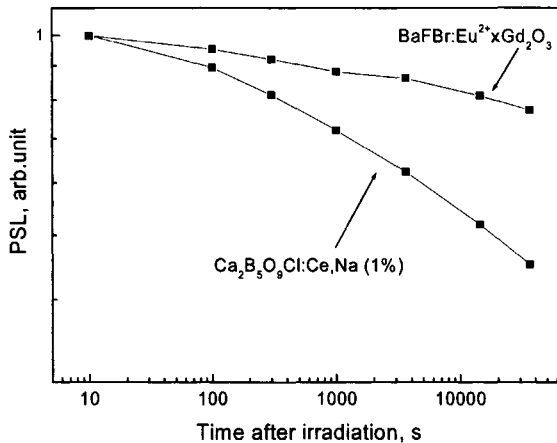


Figure 6.6: Fading of PSL signal in $BaFBr:Eu^{2+}xGd_2O_3$ and $Ca_2^{10}B_5O_9Cl:Ce,Na$ (1%) at room temperature.

The results of Table 6.3 show that the neutron sensitivity of $BaFBr:Eu^{2+}xGd_2O_3$ is 16 times higher than that of $Ca_2^{10}B_5O_9Cl:Ce,Na$ (1%). At the same time, the γ -ray sensitivity of $BaFBr:Eu^{2+}xGd_2O_3$ is 125 times higher than that of $Ca_2^{10}B_5O_9Cl:Ce,Na$ (1%). Thus, the S_n/S_γ of $Ca_2^{10}B_5O_9Cl:Ce,Na$ (1%) is 8 times better than that of $BaFBr:Eu^{2+}xGd_2O_3$.

The fading properties of the studied materials are presented in Figure 6.6. It is seen that 10 hours after irradiation 46 % of the initial PSL signal is left in $Ca_2^{10}B_5O_9Cl:Ce,Na$ (1%), and this value is 77 % for the $BaFBr:Eu^{2+}xGd_2O_3$.

Table 6.3: The measured PSL yields (S_n and S_γ) of some studied materials after neutron (1.8 Å) and γ - irradiation (662 keV). The yields are normalised to the one of BaFBr:Eu²⁺xGd₂O₃. The samples were measured at the same conditions.

Items	Sr ₂ ^{nat} B ₅ O ₉ Br:Ce ³⁺	Ca ₂ ¹⁰ B ₅ O ₉ Cl:Ce,Na	BaFBr:Eu ²⁺ xGd ₂ O ₃
S_n	3.2	6	100
S_γ (at 662 keV)	0.26	0.14	18
S_n/S_γ	12	43	5.5

6.4 Discussions

6.4.1 The difference between S_n/S_γ (haloborates) and S_n/S_γ (BaFBr:Eu²⁺xGd₂O₃)

As discussed in [2], the energy deposition in the phosphor from the ¹⁰B(n, α)⁷Li reaction is 40 times higher than that from Gd(n, γ) reaction. Thus, the gain of haloborates upon neutron irradiation in comparison with γ -ray irradiation should be at least 40 times higher than that of Gd-phosphors. The results of Table 6.3 show that S_n/S_γ of Sr₂^{nat}B₅O₉Br:Ce³⁺ is 2.2 times and S_n/S_γ of Ca₂¹⁰B₅O₉Cl:Ce,Na (1%) is 8 times higher than that of BaFBr:Eu²⁺xGd₂O₃. The question arises: why are these values much less than the expected factor of 40?

Gd and ¹⁰B nuclei produce different secondary particles after neutron capture. In case of Gd these are conversion electrons (ce's), γ -rays and X-rays with the energy range between 25 and 200 keV. In case of boron, ⁴He and ⁷Li particles are produced with a total energy of 2.30 MeV. The ionisation density of these heavy particles is very high in comparison with γ -rays and ce's. It was found for scintillators that the light yield per unit of absorbed alpha particle energy relative to the light yield per unit of absorbed γ -ray energy can vary between 0.5 for NaI:Tl⁺ and 0.08 for plastic scintillators [3]. Thus, the ratio of the number of created PSL active defects per incident neutron to the number of created PSL active defects per incident γ -ray can be the same order of magnitude for Gd-phosphor and for borates. This effect can explain the smaller than expected difference between S_n/S_γ for Gd-phosphor and for haloborates.

To check this point, TL and PSL experiments upon irradiation with α -particles have been performed. ²⁴¹Am was used as irradiation source. The decay of ²⁴¹Am produces one α -particle with the energy about 5.57 MeV and in 37% of the cases a γ -ray with energy ~60 keV. Since the range of α -particles in a material is just several microns, the surface defects can play a significant role. The TL glow curves of Ca₂B₅O₉Cl:Ce³⁺ after irradiation with α - and γ -ray irradiation were recorded. The shapes of TL glow curves are identical after γ - and α -irradiation. Thus, it is possible to conclude that surface effects do not influence the type of created defects and the trap filling upon irradiation with α -particles.

The influence of 60 keV γ -rays from the ²⁴¹Am on TL or PSL intensity also must be investigated, especially if the ratio of the signal per unit of absorbed alpha particle energy relatively to the signal per unit of absorbed γ -ray energy (S_α/S_γ) is very small. If the sample is

covered by Teflon tape with of 100- μ m thickness, all alpha particles will be stopped in the Teflon tape. The measured TL signal at these conditions is caused only by the γ -ray component from the ^{241}Am source. It has been established that the TL signal after irradiation with γ -ray component from the ^{241}Am source is about 200 times less than that from $\alpha+\gamma$ irradiation from the same source. The energy deposition in the phosphor from the α component is about 250 time more than that from γ component (5.517MeV/0.37*60keV). Therefore we may conclude that the value TL_{α}/TL_{γ} is in the order of 1 in the studied haloborates. Apparently, the same relation must hold for PSL process.

Thus, another explanation of the smaller than expected difference between S_n/S_{γ} for Gd-phosphor and for haloborates must be found.

6.4.2 Absorption of PSL light in the phosphor layer

The TL or PSL photons in the phosphor travel to the surface of the phosphor suffering from a number of scatterings on grains. If the phosphor represents even a very low absorbing substrate for the emitted light, the probability for the photon to be absorbed is much higher than in a crystal. We have studied the attenuation of the emitted light in powdered phosphors. Three samples have been made by pressing $Sr_2B_5O_9Br:Ce^{3+}$ phosphor powder in pills with different thickness $d = 200, 375$ and $650 \mu m$ applying the same pressure. All the samples have been irradiated by a ^{241}Am source and put in the TL reader with the irradiated side directed to the PMT. With the sample in this orientation the TL signals have been recorded (TL_{front}). After annealing, samples were irradiated again, and TL signals have been recorded, but during the measurements the irradiated side of the sample was positioned to the opposite direction of the PMT window (TL_{rear}). During the irradiation with α particles, all the e-h pairs are created in a layer much thinner than the thickness of the sample due to the small range of alpha particles (several microns). Thus, the ratio TL_{front}/TL_{rear} represents the attenuation of the emitted light in the phosphor layer. For the sample with the thickness $d=200 \mu m$ the TL_{front}/TL_{rear} ratio equals 20, and for the samples with $d=375$ and $650 \mu m$ it is more than 100. It means that if a photon is created at a depth of 200 microns from the surface of the phosphor, it will escape with a probability of 5%. Note, that this value for absorption of emitted light is very close to that measured for $Y_2O_2S:Eu$ screen phosphor in [4].

The results mentioned above bring to the conclusion that not only the value of energy deposition, but also the depth distribution of the deposited energy is of main importance to observe a high PSL and TL signal in the phosphor material.

The expressions for absorption of emitted light passing trough the phosphor layer can be found in [4,5]. For rough estimations we assume that the absorption of light passing through the phosphor layer depends exponentially on the thickness of the layer. Based on results presented above, the attenuation coefficient $\mu=150 [1/cm]$ has been derived.

Thus the probability for the PSL photon that created at a depth x to escape from the surface:

$$Escape(x) = \exp(-\mu \cdot x) \quad (6.1)$$

The probability for the neutron to be absorbed in a phosphor layer with the thickness x can be found from the next well-known formula:

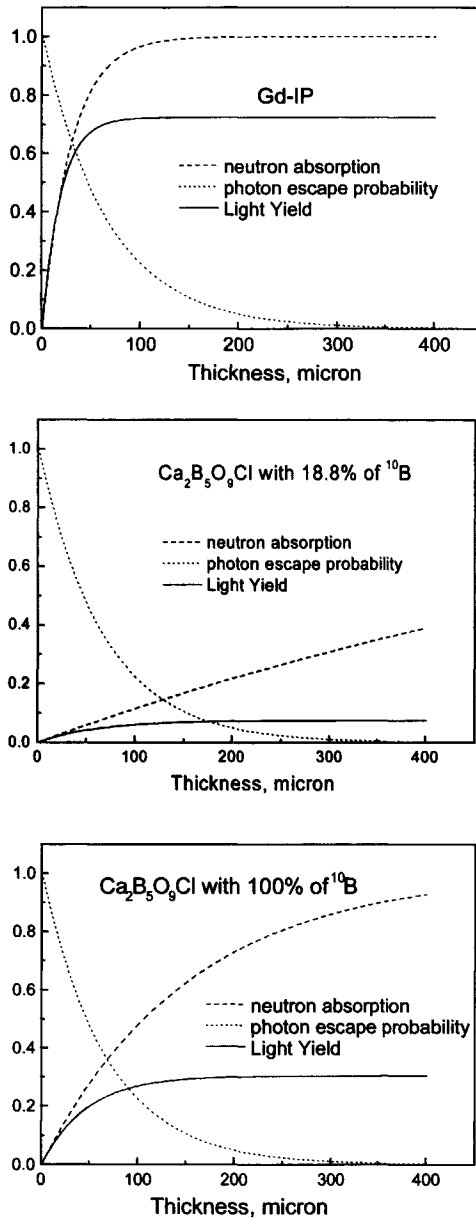


Figure 6.7: Calculated neutron absorption probability, PSL photon escape probability and the stimulated Light Yield per incident neutron as a function of phosphor layer thickness for Gd-IP (a), haloborates with natural abundance of ^{10}B (b) and with 100% of ^{10}B (c).

$$Absorb(x) = 1 - \exp\left(-\rho \cdot \frac{w}{M} \cdot N_A \cdot \sigma \cdot x\right) \quad (6.2)$$

where ρ – density of the material ($\rho = BaFBrxGd_2O_3$ g/cm³ for Gd-phosphor, and $\rho = 2.04$ g/cm³ for studied haloborates), M – molar mass of the absorbed element (g·mol⁻¹), N_A – Avogadro constant (mol⁻¹), w – weighting factor of absorbed element in the phosphor ($w(^{10}B)$ in $Ca_2B_5O_9Br$ is 0.027 in case of 18% enrichment of ^{10}B and 0.151 in case of 100% enrichment of ^{10}B , $w(^{nat}Gd)$ is 0.525 in $BaFBrxGd_2O_3$ with 1:1 molar ratio of $BaFBr$ to Gd_2O_3), σ – cross-section of thermal neutron capture (3837 barn for ^{10}B and 48890 barn for ^{nat}Gd at neutron wavelength $\lambda = 1.8$ Å).

Thus, the light yield (LY) of the TL or PSL per incident neutron is proportional to the probability for the incident neutron to be absorbed – $Absorb$, the number of TL or PSL photons created per absorbed neutron $N_{photperneutron}$ and the probability that this photon will escape from the surface of the phosphor with thickness d :

$$LY(d) \sim N_{photperneutron} \int_d Escape(x) \cdot \frac{\partial Absorb(x)}{\partial x} dx \quad (6.3)$$

The calculated neutron absorption probability, probability of PSL photons to escape and the light yield per incident neutron as a function of phosphor layer thickness are plotted in Figure 6.7 for haloborates with 18.8% and 100 % enrichment of ^{10}B and for $BaFBrxGd_2O_3$. For $BaFBrxGd_2O_3$ the photon attenuation coefficient has been taken the same as for haloborates. It is seen that an increase of phosphor thickness after a certain value leads to the higher probability of neutron capture, but this does not lead to a higher light yield. The deeper from the surface the neutron is captured the lower the probability that the created PSL photon will reach the surface of the phosphor. Due to the high absorption probability of thermal neutrons in $BaFBrxGd_2O_3$ most of the PSL photons are created in the layer close to the surface, and thus there is a higher probability for the created PSL photons to be emitted than in case of borates.

For the fixed thickness $d = 200$ micron the $LY/N_{photperneutron}$ for $BaFBrxGd_2O_3$ is about 10 times more than that for haloborates with natural abundance of ^{10}B . Thus, despite the $N_{photperneutron}/N_{photpegamma}$ ratio for borates is 40 times higher than for $BaFBrxGd_2O_3$, the difference in PSL yield of haloborates and $BaFBrxGd_2O_3$ is about the same after γ - and neutron irradiation due to the lower neutron absorption efficiency of borates and attenuation of PSL light in phosphor layer. The use of haloborates with 100 % of ^{10}B increases the PSL yield by a factor of 4 (Figure 6.7). This explains well the results in Table 6.3.

6.5 Conclusions

The TL and PSL properties of the series of haloborates with general formula $M_2B_5O_9X:Ce^{3+},A^+$ ($M=Ba,Sr,Ca$, $X=Cl,Br$, $A=Na^+,K^+$) were studied. The results of this study led to the conclusion that the $Ca_2B_5O_9Cl:Ce^{3+},Na^+$ compound is the most promising of the whole studied series for detection of thermal neutrons and with reduced sensitivity to γ - rays, since it has the lowest Z_{eff} number and, at the same time, a relatively high PSL yield.

The read-out parameters, i.e., stimulation wavelength and band-pass filter of commercial image plate scanners are highly inefficient for haloborates.

When optimised read-out parameters are implemented, the PSL light yield of $\text{Ca}_2^{10}\text{B}_5\text{O}_9\text{Cl}:\text{Ce},\text{Na}$ (1%) after neutron irradiation at $\lambda \sim 1.8 \text{ \AA}$ is 16 times less than that of $\text{BaFBr}:\text{Eu}^{2+}x\text{Gd}_2\text{O}_3$. However the neutron to gamma discrimination of $\text{Ca}_2^{10}\text{B}_5\text{O}_9\text{Cl}:\text{Ce},\text{Na}$ (1%) is almost an order of magnitude better than that of $\text{BaFBr}:\text{Eu}^{2+}x\text{Gd}_2\text{O}_3$. Therefore haloborate phosphors could be more attractive when utilised in environments with a high γ -ray background.

The observed difference between S_n/S_γ of the Gd-phosphor and haloborates, when irradiated at 1.8 \AA is smaller than expected. The lower neutron absorption efficiency of haloborates and the absorption of PSL photons in the phosphor layer allow us to explain the observed results. The better S_n/S_γ of haloborates is expected when they are applied in experiments with cold neutrons, since the neutron capture cross section of ^{10}B increases with decreasing neutron energy.

References

- [1] Knitel M. J. *et al.*, Nucl. Instr. And Meth. A **449** (2000) 595
- [2] M. J. Knitel *et al.*, Nucl. Instr. and Meth. A **449** (2000) 578
- [3] Bertolini G., del Turco A. M., Restelli G., Nucl. Instr. Meth. **7** (1960) 350
- [4] Wang P. C. and Cargill G. S., J. Appl. Phys. **81** (3) (1997) 1031
- [5] Reichman J., Appl. Opt. **12** (1973) 1811

7 Spectroscopic and storage properties of $\text{LiLnSiO}_4:\text{Ce}^{3+}, \text{Sm}^{3+}$

7.1 Introduction

It was already discussed in [2.3.2] that activation of a phosphor with two specific rare-earth impurities could lead to the storage effect. In this chapter a new type of such storage phosphor is introduced. The storage mechanism is related to the presence of two types of activator ions: Ce^{3+} and Sm^{3+} , which play the role of hole and electron trap respectively.

An ions tendency to capture a hole or an electron, i.e. to become stabilised in different valence states depends on the energy position of its ground 4f state relatively to the host band. If this information is known for one of the 14 lanthanides, the energy level diagram can be constructed for all 13 other lanthanides [2.3.2]. These diagrams can be very helpful for determination of the hole and electron trap depth of lanthanide impurities.

This chapter is organised as follows. First, a general introduction to the infrared stimuable phosphors will be given, where the storage effect is based on double activation with lanthanides.

After that the spectroscopy of Ce^{3+} , Sm^{3+} and Eu^{3+} doped LiLnSiO_4 , where $\text{Ln}=\text{Y}$, Lu will be presented. Based on these data the energy level diagram of lanthanide ions in LiYSiO_4 and LiLuSiO_4 will be plotted.

Afterwards, the TL, PSL and some other properties of yttrium and lutetium silicates with different rare-earth dopants will be presented, and the nature of trapping defects in these phosphors will be elucidated. The results will be compared and a consistent model of the storage and recombination mechanism in LiYSiO_4 and LiLuSiO_4 will be constructed.

An additional section will concern the quantitative properties of these novel phosphors in comparison with commercial image plates.

7.2 Infrared Stimulable Phosphors (ISP)

There have been many reports about ISPs such as $\text{MgS}:\text{Eu}^{2+}, \text{Sm}^{3+}$ [1], $\text{MgS}:\text{Ce}^{3+}, \text{Sm}^{3+}$ [1], $\text{CaS}:\text{Eu}^{2+}, \text{Sm}^{3+}$ [2-6], $\text{CaS}:\text{Ce}^{3+}, \text{Sm}^{3+}$ [7], $\text{SrS}:\text{Eu}^{2+}, \text{Sm}^{3+}$ [8-10], $\text{SrS}:\text{Ce}^{3+}, \text{Sm}^{3+}$ [8,9]. Among those phosphors $\text{CaS}:\text{Eu}^{2+}, \text{Sm}^{3+}$ exhibits fast PSL kinetics and has a high chemical stability. The samples with $\text{Ce}^{3+}, \text{Sm}^{3+}$ double doping were less studied than those with Eu^{2+} and Sm^{3+} .

Emission spectra of these materials upon UV or X-ray excitation exhibit the $5d \rightarrow 4f$ transitions of Ce^{3+} or Eu^{2+} centres and $4f \rightarrow 4f$ emission lines of Sm^{3+} ions. There are two types of Sm^{3+} centres – in symmetric and asymmetric sites. The latter is probably related to nearby charge compensation defects [2]. The PSL emission spectra, i.e. emission spectra

upon photostimulation of irradiated ISPs, show the emission from Ce^{3+} or Eu^{2+} centres, while no emission from Sm^{3+} has been observed.

The spectrum of trap-filling efficiency, that corresponds to PSL in $CaS:Eu^{2+},Sm^{3+}$ represents a composition of three bands. These bands were attributed to the transitions from the $^8S_{7/2}$ state to the two 5d states and one 6s state of Eu^{2+} . Therefore the trap filling occurs by ionisation of Eu^{2+} centres.

The general storage mechanism of ISPs can be described as follows. Upon irradiation, ionisation of Eu^{2+} occurs. This is well confirmed by the presence of Eu^{2+} excitation bands in the trap-filling spectrum, i.e. excited to 5d or 6s state the electron "looses its identity" and becomes free, leaving Eu in a trivalent state. Next, it is captured by Sm^{3+} ions, forming Sm^{2+} centres. This possibility was discussed already in [2.3.2]. A creation of Sm^{2+} centres after UV illumination has been confirmed in [10]. However, which mechanism leads to ionisation of Sm^{2+} during photostimulation is not known yet. Direct injection of an electron to the conduction band or ionisation of Sm^{2+} via $4f \rightarrow 5d$ transitions could be proposed. After ionisation a free electron recombines with Eu^{3+} creating Eu^{2+} in an excited state, followed by $5d \rightarrow 4f$ emission.

PSL stimulation spectra of $CaS:Eu^{2+},Sm^{3+}$ and $CaS:Ce^{3+},Sm^{3+}$ irradiated samples look very similar and represent a broad band between 1050 and 1400 nm (taken as FWHM from [6]) with some structure. There is still a lot of discussions on whether this band is related to $4f \rightarrow 5d$ transitions in Sm^{2+} ions.

Unlike the PSL spectra, the TL emission spectra of $MgS:Eu^{2+},Sm^{3+}$ and $MgS:Ce^{3+},Sm^{3+}$ exhibit only emission from Sm^{3+} centres [1]. This can be explained by hole migration from Eu^{3+} to Sm^{2+} with further Sm^{3+} luminescence.

7.3 Synthesis of silicates

Samples of $LiLn_{1-x-y}Ce_xSm_ySiO_4$, $LiLn_{1-x-y}Ce_xTb_ySiO_4$ and $LiLn_{1-x-y}Ce_xEu_ySiO_4$ were prepared by solid state reaction from Li_2CO_3 , Ln_2O_3 ($Ln=Y,La,Gd$ or Lu), SiO_2 and CeF_3 and/or Sm_2O_3 , Tb_2O_3 or Eu_2O_3 . The mixture was fired for 8 hours at a temperature of $800^\circ C$ in Ar atmosphere. After that, samples were ground and fired again for 15 hours in Ar atmosphere. The firing temperature in the last procedure varied depending on the dopant or the host lattice.

The crystal structures of $LiLnSiO_4$ are known from Blasse [11] and Nakayama [12]. A large number of structures found reminds of the polymorphism of Ca_2SiO_4 . The present compounds can be derived from Ca_2SiO_4 by the substitution of $2Ca^{2+} \rightarrow Li^+ + Ln^{3+}$. Compounds with $Ln=La...Dy$ are hexagonal [11,12]. Compounds with $Ln=Ho...Lu$ and Y are orthorhombic. Six oxygen atoms of SiO_4 tetrahedrons surround the Ln^{3+} ion that occupies a site with C_1 point symmetry.

All the samples were checked by X-ray diffraction analysis and compared with diffraction patterns known from [12]. In the X-ray diffraction spectra of $LiYSiO_4$ samples, fired at $1075^\circ C$ in the second stage, additional lines from a parasitic phase were found and attributed to the $Y_{4.67}(SiO_4)_3O$ phase. For the sample fired at $1000^\circ C$ these lines are absent. The latter can be explained by Li evaporation from the yttrium samples at temperatures, higher than $1000^\circ C$. Since the $LiYSiO_4$ and $LiLuSiO_4$ are orthorhombic and the phases without Li are hexagonal, it became possible to distinguish the "parasitic" phase. For

LiLuSiO_4 series the final firing temperature was 1150°C , for $\text{LiYSiO}_4 - 1000^\circ\text{C}$. All the synthesised samples are listed in Table 7.1.

Table 7.1: Compounds synthesised for the current study. X-ray diffraction patterns were compared with those reported in [12].

$\text{LiLu}_{1-x-y}\text{Ce}_x\text{Sm}_y\text{SiO}_4$	$x=0.01, y=0$ $x=0.01, y=0.002$ $x=0.01, y=0.01$ $x=0.001, y=0.01$ $x=0, y=0.01$
$\text{LiLu}_{1-x-y}\text{Ce}_x\text{Tb}_y\text{SiO}_4$	$x=0, y=0.01$ $x=0.005, y=0.005$
$\text{LiY}_{1-x-y}\text{Ce}_x\text{Sm}_y\text{SiO}_4$ $\text{LiLa}_{1-x-y}\text{Ce}_x\text{Sm}_y\text{SiO}_4$ $\text{LiGd}_{1-x-y}\text{Ce}_x\text{Sm}_y\text{SiO}_4$	$x=0.01, y=0$ $x=0.01, y=0.002$
$\text{LiLu}_{1-x-y}\text{Ce}_x\text{Eu}_y\text{SiO}_4$ $\text{LiY}_{1-x-y}\text{Ce}_x\text{Eu}_y\text{SiO}_4$	$x=0, y=0.01$ $x=0.01, y=0.001$

7.4 Spectroscopic properties of LiLnSiO_4 doped with rare-earth

7.4.1 X-ray excited luminescence of $\text{LiLnSiO}_4:\text{Ce},\text{Sm}$, $\text{Ln}=\text{Y},\text{Gd},\text{La},\text{Lu}$

In Figure 7.1 the X-ray induced emission spectra of the $\text{LiLnSiO}_4:\text{Ce},\text{Sm}$ series, where $\text{Ln}=\text{Y},\text{Gd},\text{La},\text{Lu}$ are presented.

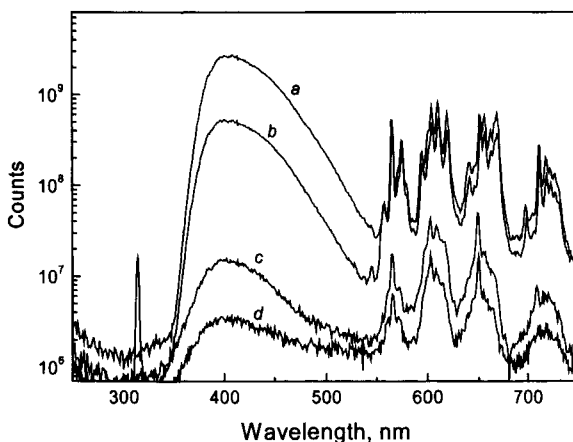


Figure 7.1: X-ray excited emission spectra of $\text{LiLuSiO}_4:1\%\text{Ce}^3,0.2\%\text{Sm}^{3+}$ (curve a), $\text{LiYSiO}_4:1\%\text{Ce}^3,0.2\%\text{Sm}^{3+}$ (curve b), $\text{LiLaSiO}_4:1\%\text{Ce}^3,0.2\%\text{Sm}^{3+}$ (curve c) and $\text{LiGdSiO}_4:1\%\text{Ce}^3,0.2\%\text{Sm}^{3+}$ (curve d) recorded at room temperature.

The spectra consist of the known emission band of Ce^{3+} $5d \rightarrow 4f$ transitions with a maximum at 400 nm and Sm^{3+} $4f \rightarrow 4f$ transitions in the 550-800 nm range. In the Ce^{3+} emission spectrum the ground state components ($^2F_{5/2}$ and $^2F_{7/2}$) can not be resolved. The emission intensities of both Ce^{3+} and Sm^{3+} centres in $LiLaSiO_4$ and $LiGdSiO_4$ are more than two orders of magnitude lower than those in $LiLuSiO_4$ and $LiYSiO_4$. Also the structure of Sm^{3+} $4f \rightarrow 4f$ transitions in $LiLnSiO_4$, $Ln=La, Gd$ is different from that in $LiLnSiO_4$, $Ln=Y, Lu$. The latter is an evidence of different crystallographic structures and consequently different site symmetries occupied by Sm^{3+} in $LiLnSiO_4$, $Ln=La, Gd$ and $LiLnSiO_4$, $Ln=Y, Lu$. The hexagonal $LiLaSiO_4$ and $LiGdSiO_4$ will not be considered in this work anymore.

The emission spectrum of Sm^{3+} in $LiLuSiO_4$ has been measured more accurately at 77 K as it is shown in Figure 7.2. The $4f^6$ electrons of the Sm^{3+} ion substituting a cation in a crystal are free from the electron-phonon interaction, since they are electrically shielded by $5s^2 \cdot 5p^6$ electron clouds. The crystal field around the Sm^{3+} ion splits each $4f$ level into Stark components. In case of a low-symmetry crystal field (C_1 -symmetry of Lu ions in $LiLuSiO_4$) each level splits in a number of $(J+1/2)$ Stark components. The emission spectrum of Sm^{3+} is expected to be composed of 12 groups of transitions within the $4f^6$ configuration: $^4G_{5/2} \rightarrow ^6H_J$ ($J=5/2, 7/2, 9/2, 11/2, 13/2, 15/2$) and $^4G_{5/2} \rightarrow ^6F_J$ ($J=1/2, 3/2, 5/2, 7/2, 9/2, 11/2$) [13]. The crystal field splits each group into $J+1/2$ lines. In the 550-750 nm wavelength range only four groups $^4G_{5/2} \rightarrow ^6H_J$ ($J=5/2, 7/2, 9/2, 11/2$) can be observed.

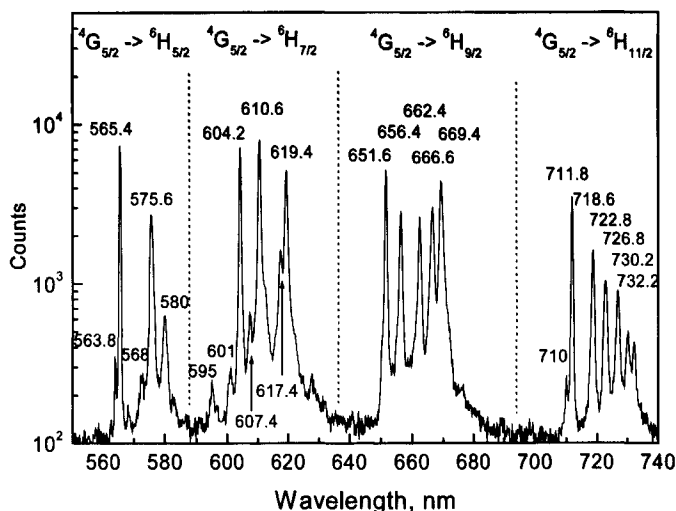


Figure 7.2: X-ray excited emission spectrum of $LiLuSiO_4:1\%Ce^{3+}, 0.2\%Sm^{3+}$ recorded at 77 K. The peak positions are given in nm.

In the first group of $^4G_{5/2} \rightarrow ^6H_{5/2}$ transitions three lines of high intensity and two lines of low intensity are observed. However only $5/2+1/2=3$ lines are expected. Therefore, either two types of Sm^{3+} centres are present in the material or the extra low intensity lines at 563.8 and

568 nm correspond to phonon satellite lines. The electron-phonon coupling is very weak for the 4f electrons, which matches with positions of vibronic lines. In the group of ${}^4\text{G}_{5/2} \rightarrow {}^6\text{H}_{9/2}$ transitions five lines are observed, as is predicted. This is an evidence for only one type of Sm^{3+} centre present in LiLuSiO_4 .

7.4.2 X-ray excited luminescence of $\text{LiLnSiO}_4, \text{Ln}=\text{Y}, \text{Lu}$ doped with Ce^{3+} and Eu^{3+}

Yttrium and lutetium silicates doubly activated with $\text{Ce}^{3+}, \text{Eu}^{3+}$ were synthesised. The measured emission spectra of yttrium and lutetium silicates are the same.

$\text{LiLuSiO}_4:1\%\text{Ce}^{3+},0.2\%\text{Eu}^{3+}$ shows quite intense emission from both Ce^{3+} and Eu^{3+} centres (Figure 7.3). The emission of Eu^{3+} centres is mostly determined by forced electric-dipole ${}^5\text{D}_0 \rightarrow {}^7\text{F}_2$ transitions.

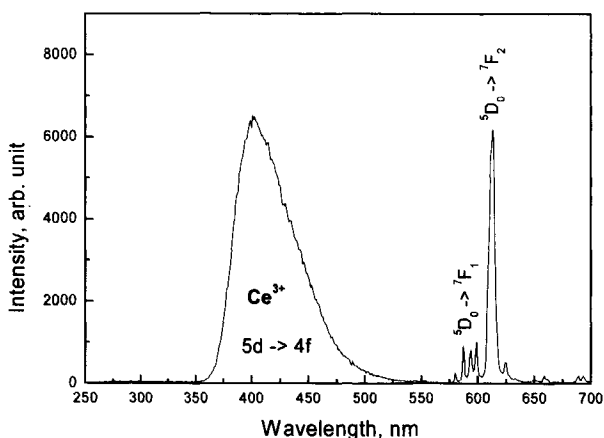


Figure 7.3: X-ray excited emission spectrum of $\text{LiLuSiO}_4:1\%\text{Ce}^{3+},0.2\%\text{Eu}^{3+}$ recorded at room temperature.

7.4.3 Excitation spectra of Ce^{3+} in $\text{LiLnSiO}_4, \text{Ln}=\text{Y}, \text{Lu}$

The excitation spectra of Ce^{3+} emission in LiLuSiO_4 and LiYSiO_4 are presented in Figure 7.4. The bands at 351, 315, 300 and 354, 317, 304 nm are attributed to the Ce^{3+} 5d components in LiLuSiO_4 and LiYSiO_4 respectively. This attribution is confirmed by the decay time measurements of Ce^{3+} , shown in Figure 7.5. The decay curves of Ce^{3+} emission excited at 302 and 320 nm have 30 ns decay time, which is typical for fast dipole allowed $5\text{d} \rightarrow 4\text{f}$ emission.

The small relative shift of 5d states in the two compounds can be attributed to the difference in ionic radii of Y ($R=1.040 \text{ \AA}$) and Lu ($R=1.001 \text{ \AA}$) in six-fold coordination for the substituting Ce^{3+} ions [14].

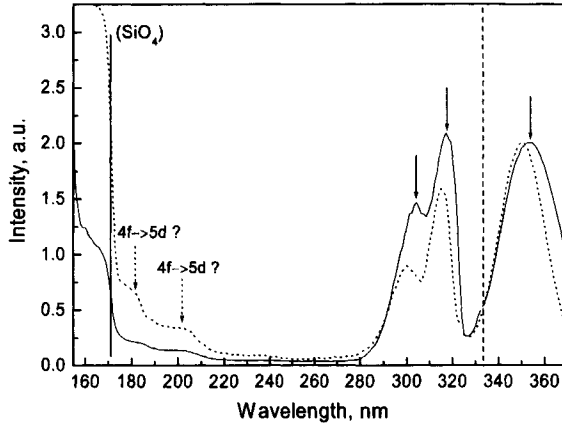


Figure 7.4: The excitation spectra of Ce^{3+} emission at 390 nm in $LiLuSiO_4:1\%Ce^{3+}$ (solid curve) and $LiYSiO_4$ (dotted curve). Measurements below 335 nm were carried out at 10 K using synchrotron radiation. A quartz window was used to cut off 2nd order effects from the radiation below 150 nm. Measurements above 335 nm were carried out at room temperature using a spectrofluorimeter. The bands indicated by solid arrows are attributed to the first three 5d bands of Ce^{3+} . The bands indicated by dotted arrows are attributed indirectly to the remaining 5d bands of Ce^{3+} .

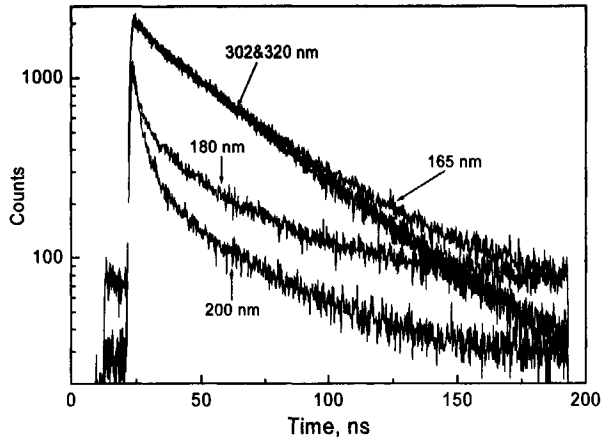


Figure 7.5: The decay time curves of Ce^{3+} emission at 390 nm in $LiLuSiO_4:1\%Ce^{3+}$ upon excitation at different wavelengths. The measurements were carried out using synchrotron radiation at 10 K.

7.4.4 Excitation spectra of Eu^{3+} in LiLnSiO_4 , $\text{Ln}=\text{Y}, \text{Lu}$

Excitation and emission spectra of $\text{LiYSiO}_4:\text{Eu}^{3+}$ measured at 10 K under synchrotron radiation are shown in Figure 7.6. The excitation spectrum of Eu^{3+} emission at 610 nm shows a broad band with some structure near 220 nm. When the sample is excited at 206 nm, two types of emissions can be observed. The first is a typical sharp-line emission due to Eu^{3+} $4f \rightarrow 4f$ emission and the second is a broad band at about 350 nm. The excitation spectrum of this emission at 350 nm is shown in Figure 7.6a and has a threshold at about 210 nm. It was established that excitation at 225 nm causes only the $4f \rightarrow 4f$ emission and no emission at 350 nm can be observed. The origin of the centre responsible for the 350-nm emission is unknown.

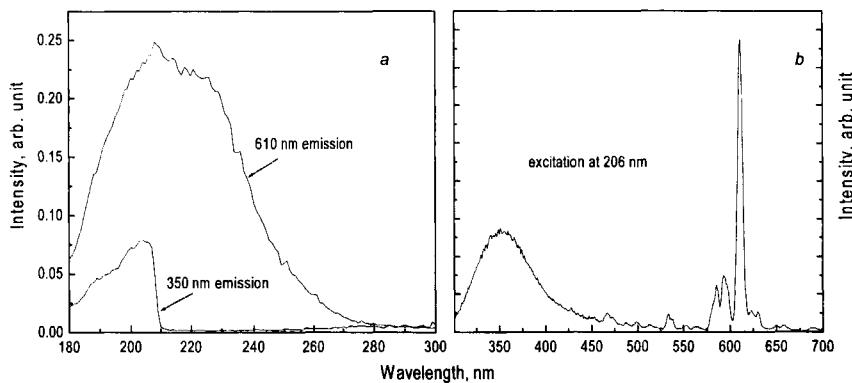


Figure 7.6: “a”: the excitation spectrum of Eu^{3+} emission at 610 nm and the excitation spectrum of unknown emission at 350 nm. “b”: the emission spectrum of $\text{LiYSiO}_4:1\%\text{Eu}^{3+}$ at 206 nm excitation. Measurements were carried out at 10 K using synchrotron radiation.

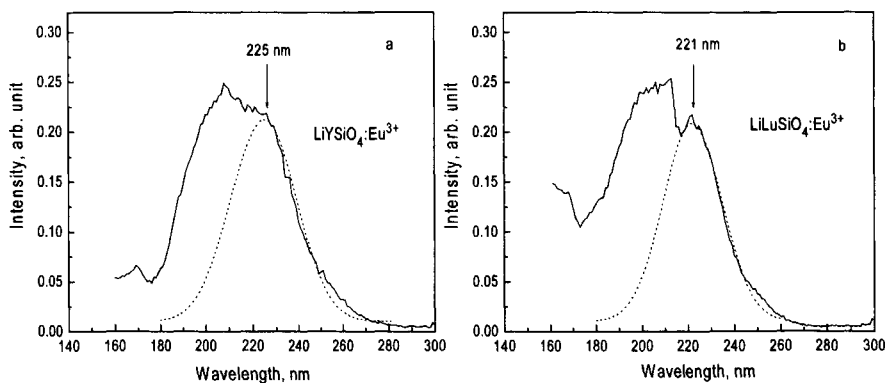


Figure 7.7: “a”: the excitation spectrum of Eu^{3+} emission at 610 nm in $\text{LiYSiO}_4:1\%\text{Eu}^{3+}$ sample. “b”: the excitation spectrum of Eu^{3+} emission at 610 nm in $\text{LiLuSiO}_4:1\%\text{Eu}^{3+}$ sample. Dotted curves represent the Gaussian fit. Measurements were carried out at 10 K using synchrotron radiation.

The edge at 210 nm is more clearly visible in the excitation spectrum for $\text{LiLuSiO}_4:\text{Eu}^{3+}$ in Figure 7.7b. We conclude that the excitation spectrum of Eu^{3+} emission consists of the superposition of two bands. One is from the unknown centre that can only be excited at $\lambda < 210$ nm and the other has been fitted by a Gaussian shaped broad band, see Figure 7.7. We attribute this band to the charge transfer of an electron from the top of the valence band to Eu^{3+} .

7.4.5 Excitation spectra of Sm^{3+} in LiLnSiO_4 , $\text{Ln}=\text{Y},\text{Lu}$

The excitation spectrum of Sm^{3+} emission in $\text{LiLuSiO}_4:1\%\text{Sm}^{3+}$ is shown in Figure 7.8. Three bands at 210, 183 and 173 nm are clearly resolved. The host absorption edge is not pronounced, which is evidence of low efficiency of the energy transfer from free e-h pairs to Sm^{3+} centres.

It was discussed in detail in [15] that the energy of the first spin allowed $4f \rightarrow 4f5d$ transition of any lanthanide in a particular compound can be predicted with an accuracy of less than 0.7 eV, if the $4f \rightarrow 4f5d$ transition of at least one lanthanide is known. The energy of the first $4f \rightarrow 5d$ transition of Ce^{3+} in LiLuSiO_4 is 3.53 eV (351 nm). According to [15] the lowest 5d band of Sm^{3+} must be located at 3.29 eV higher energy, i.e. at 6.82 eV (182 nm). Thus, the band at 183 nm in the excitation spectrum in Figure 7.8 can be attributed to the first $4f \rightarrow 4f5d$ transition in the Sm^{3+} ion. Since the 5d level in Sm^{3+} is placed above the quite dense structure of 4f levels, the $5d \rightarrow 4f$ luminescence in Sm^{3+} is not possible. Excited 5d electrons further relax via 4f states resulting only in $4f \rightarrow 4f$ emission (Figure 7.2).

The band at 173 nm has about the same width and intensity as the 5d band at 183 nm. Thus it can be attributed to the second Sm^{3+} 5d state.

The band at 210 nm is clearly resolved in $\text{LiLuSiO}_4:\text{Sm}^{3+}$, however it is absent in the excitation spectrum of Sm^{3+} of doubly co-doped $\text{LiLuSiO}_4:\text{Sm}^{3+},\text{Ce}^{3+}$ (Figure 7.8). The origin of this band is not known, but it is probably the same as observed in Figures 7.6 and 7.7.

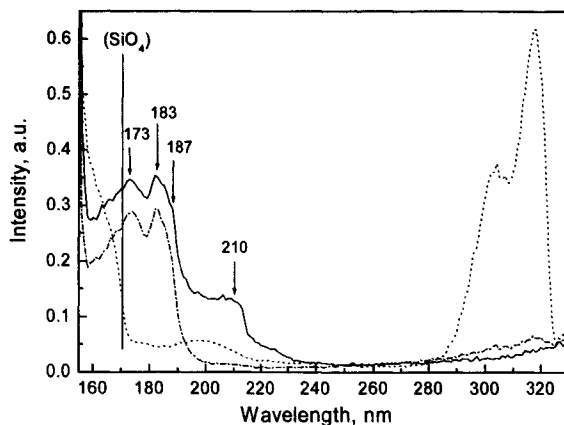


Figure 7.8: The excitation spectrum of Sm^{3+} emission at 600 nm in $\text{LiLuSiO}_4:1\%\text{Sm}^{3+}$ (solid curve) and in $\text{LiLuSiO}_4:1\%\text{Sm}^{3+},1\%\text{Ce}^{3+}$ (dash-dotted curve); and the excitation spectrum of Ce^{3+} emission at 390 nm in $\text{LiLuSiO}_4:1\%\text{Sm}^{3+},1\%\text{Ce}^{3+}$ (dotted curve). Measurements were carried out at 10 K using synchrotron radiation.

In the excitation spectrum of Ce^{3+} emission in $\text{LiLuSiO}_4:\text{Sm}^{3+}, \text{Ce}^{3+}$ no presence of bands due to Sm^{3+} is found. Therefore, Ce-Sm interaction seems to be very weak, and Ce to Sm energy transfer is not significant either, as can be seen from Figure 7.8.

7.5 Thermoluminescence of LiLuSiO_4 , Ln=Y, Lu doped with rare-earth

7.5.1 Thermoluminescence of $\text{LiLuSiO}_4:\text{Ce}^{3+}, \text{Tb}^{3+}$ or Sm^{3+}

TL glow curves of LiLuSiO_4 with different activators are shown in Figure 7.9. For the samples doped with Tb^{3+} and Ce^{3+} there is a well-pronounced TL peak at 480 K. The peak position does not change with the type of activator. The emission during the TL at 480 K corresponds to Ce^{3+} emission in $\text{LiLuSiO}_4:\text{Ce}^{3+}$, typical Tb^{3+} $4f^8 \rightarrow 4f^8$ emission in $\text{LiLuSiO}_4:\text{Tb}^{3+}$ and a superposition of both in $\text{LiLuSiO}_4:\text{Ce}^{3+}, \text{Tb}^{3+}$.

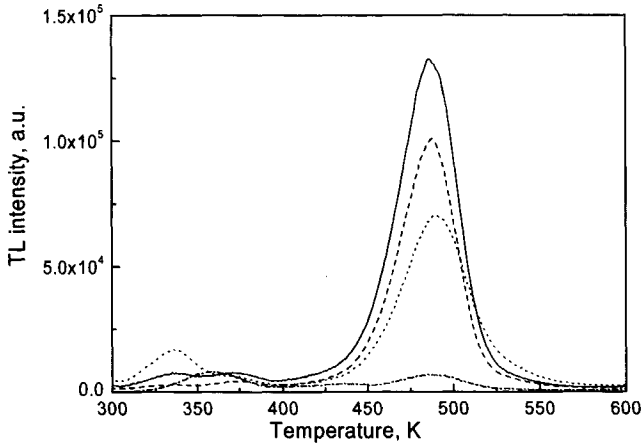


Figure 7.9: TL glow curves of $\text{LiLuSiO}_4:1\%\text{Ce}^{3+}$ (dashed curve), $\text{LiLuSiO}_4:0.5\%\text{Ce}^{3+}, 0.5\%\text{Tb}^{3+}$ (solid curve), $\text{LiLuSiO}_4:0.5\%\text{Tb}^{3+}$ (dotted curve) and $\text{LiLuSiO}_4:1\%\text{Sm}^{3+}$ (dash-dotted curve) after β -irradiation. The TL was recorded 100 s after irradiation at a heating rate of 1K/s. All the samples have the same size.

In doubly doped $\text{LiLuSiO}_4:1\%\text{Ce}^{3+}, 0.2\%\text{Sm}^{3+}$ the TL peak at 480 K has about the same intensity as in $\text{LiLuSiO}_4:1\%\text{Ce}^{3+}$, see Figure 7.10. Additionally, a strong peak appears at 340 K in the TL glow curves measured 100 seconds after irradiation. Measurements of the emission spectrum during thermal stimulation show that the emission of the peak at 340 K originates only from Ce^{3+} centres.

In Figure 7.10 the TL curves of $\text{LiLuSiO}_4:1\%\text{Ce}^{3+}, 0.2\%\text{Sm}^{3+}$ recorded at different times after irradiation are plotted. The traps responsible for the TL peak at 340 K are emptied within 5 hours.

In Figure 7.11 the TL curves of $\text{LiYSiO}_4:1\%\text{Ce}^{3+}, 0.2\%\text{Sm}^{3+}$ recorded at different times after irradiation are plotted. The low temperature peak is now positioned at 400 K and it is stable at room temperature. The high temperature TL peak in $\text{LiYSiO}_4:1\%\text{Ce}^{3+}, 0.2\%\text{Sm}^{3+}$ is

shifted 20 K to higher temperature than in $\text{LiLuSiO}_4:1\% \text{Ce}^{3+}, 0.2\% \text{Sm}^{3+}$ and it is located at 500 K. Intense TL signals were not observed in $\text{LiLuSiO}_4:\text{Ce}^{3+}, \text{Eu}^{3+}$ and $\text{LiYSiO}_4:\text{Ce}^{3+}, \text{Eu}^{3+}$ samples.

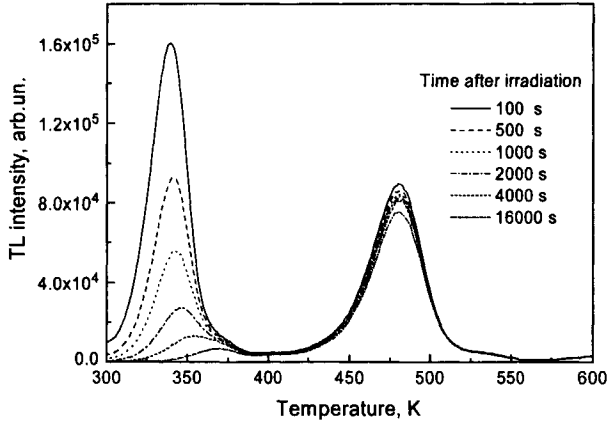


Figure 7.10: TL glow curves of $\text{LiLuSiO}_4:1\% \text{Ce}^{3+}, 0.2\% \text{Sm}^{3+}$ recorded at different times after irradiation at a heating rate of 1K/s.

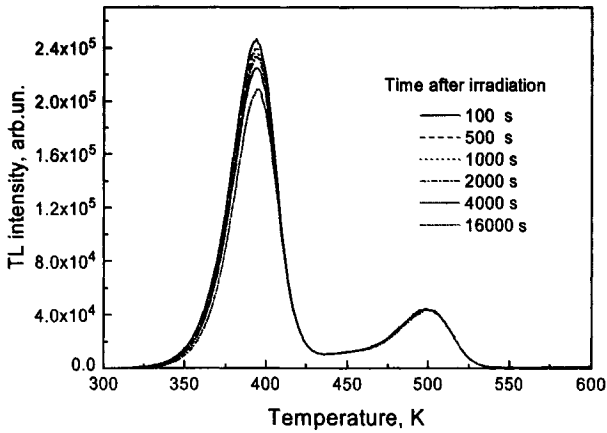


Figure 7.11: TL glow curves of $\text{LiYSiO}_4:1\% \text{Ce}^{3+}, 0.2\% \text{Sm}^{3+}$ recorded at different times after irradiation at a heating rate of 1K/s.

The TL glow curves of LiLuSiO_4 with various concentrations of Ce and Sm are shown in Figure 7.12. It is seen that $\text{LiLuSiO}_4:1\% \text{Ce}^{3+}, 0.2\% \text{Sm}^{3+}$ sample exhibits about 4 times higher TL signal than others. This sample was synthesised 1 year before the others. The other three samples were synthesised in one series. It could be that chemical properties of this sample were changed during the storing time. But it can also be because of slight difference in synthesis conditions. However this point needs further investigation.

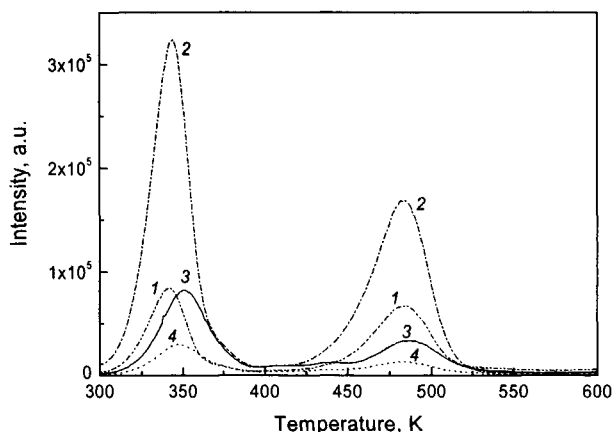


Figure 7.12: The TL glow curves of $\text{LiLuSiO}_4:1\%\text{Ce}^{3+},0.1\%\text{Sm}^{3+}$ (curve 1), $\text{LiLuSiO}_4:1\%\text{Ce}^{3+},0.2\%\text{Sm}^{3+}$ (curve 2), $\text{LiLuSiO}_4:0.1\%\text{Ce}^{3+},1\%\text{Sm}^{3+}$ (curve 3) and $\text{LiLuSiO}_4:1\%\text{Ce}^{3+},1\%\text{Sm}^{3+}$ (curve 4). The TL glow curves were recorded 300 s after irradiation at a heating rate of 1K/s. All the samples have the same size.

7.5.2 Trap-filling spectrum of LiLuSiO_4 doped with rare-earth

To study the conditions required to fill the charge traps, the samples were illuminated with photons of particular wavelength and the resulting TL curves were recorded. The area under the TL peak at 480 K was integrated and corrected for the intensity of the illumination source. The so-called trap-filling spectra of $\text{LiLuSiO}_4:1\%\text{Ce}^{3+}$ and $\text{LiLuSiO}_4:0.5\%\text{Tb}^{3+}$ are depicted in Figure 7.13. The results show that the trap-filling spectrum of $\text{LiLuSiO}_4:1\%\text{Ce}^{3+}$ is single exponential without any further structure. For the sample doped with Tb^{3+} a clear threshold at 230 nm is observed.

In the sample doubly doped with Ce^{3+} and Sm^{3+} two TL peaks are observed (Figure 7.10) that correspond to two types of trapping defects. To understand the nature of the traps, trap-filling spectra corresponding to both peaks were recorded. For $\text{LiLuSiO}_4:1\%\text{Ce}^{3+},0.2\%\text{Sm}^{3+}$ these measurements are difficult to perform due to a very fast fading of the peak at 340 K. However for $\text{LiYSiO}_4:1\%\text{Ce}^{3+},0.2\%\text{Sm}^{3+}$ the low temperature peak is stable at room temperature. The trap-filling spectra for both TL peaks in $\text{LiYSiO}_4:1\%\text{Ce}^{3+},0.2\%\text{Sm}^{3+}$ are shown in Figure 7.14. The curves are single exponential without any structure and they run parallel to each other.

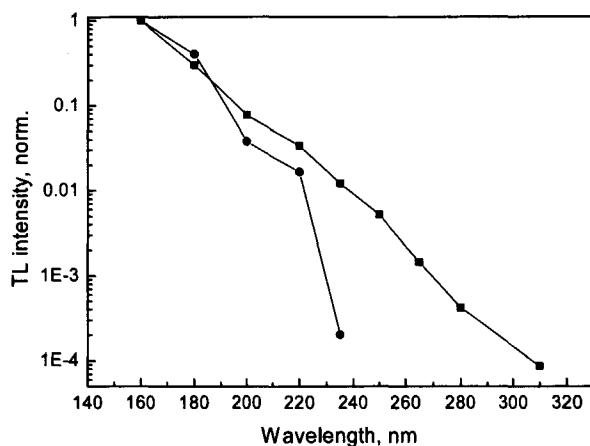


Figure 7.13: Trap-filling curve of $\text{LiLuSiO}_4:1\%\text{Ce}^3$ (squares) and $\text{LiLuSiO}_4:0.5\%\text{Tb}^3$ (circles). Each point represents the integral TL signal corresponding to the high temperature peak at 480 K after illumination with photons of certain wavelength. The curves were normalised and corrected for the spectrum of the excitation source.

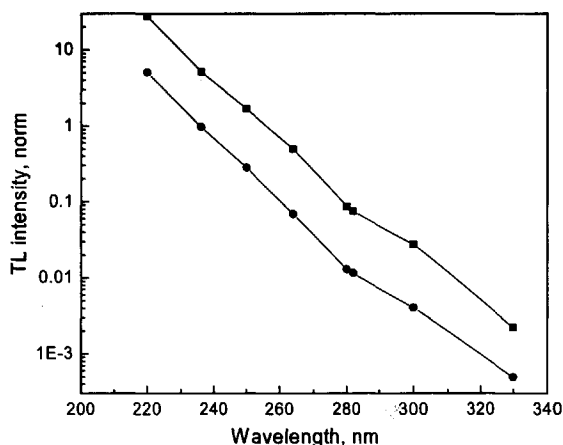


Figure 7.14: Trap filling curve of $\text{LiYSiO}_4:1\%\text{Ce}^3, 0.2\%\text{Sm}^{3+}$. Each point represents the integral TL signal corresponding to the low temperature peak at 400 K (squares) and to the high temperature peak at 500 K (circle) after illumination with photons of certain wavelength. The curves were normalised and corrected for the spectrum of the excitation source.

7.6 Photostimulated luminescence of $\text{LiLuSiO}_4:\text{Ce}^{3+},\text{Sm}^{3+}$ and $\text{LiYSiO}_4:\text{Ce}^{3+},\text{Sm}^{3+}$

7.6.1 PSL stimulation spectra of $\text{LiLuSiO}_4:\text{Ce}^{3+},\text{Sm}^{3+}$ and $\text{LiYSiO}_4:\text{Ce}^{3+},\text{Sm}^{3+}$

To study the conditions required to empty the filled traps, the irradiated samples were stimulated as a function of photon wavelength. During the photostimulation, the released charges recombine on luminescence centres and the resulting luminescence is detected. In Figure 7.15 the photostimulation spectra of $\text{LiLuSiO}_4:1\%\text{Ce}^{3+},0.2\%\text{Sm}^{3+}$ are plotted. They were recorded immediately (curve a) and two hours (curve b) after ^{60}Co -irradiation for 20 min with a dose rate of 6 kGy/hour. The photostimulation curve of $\text{LiLuSiO}_4:1\%\text{Ce}^{3+},0.1\%\text{Sm}^{3+}$ recorded immediately after irradiation represents the stimulation spectrum of the two traps corresponding to TL peaks at 340 and 480 K. This curve starts at 650 nm and monotonically increases with photon energy with a plateau at about 580 nm (curve a, Figure 7.15). The photostimulation curve recorded two hours after irradiation has a threshold at 570 nm, see curve b in Figure 7.15. As can be seen in Figure 7.10 the TL peak at 340 K completely disappears two hours after irradiation. Therefore, curve b in Fig. 11 represents the stimulation spectrum of trapped electrons corresponding to the TL peak at 480 K. Subtracting curve "b" from curve "a", see the insert of Figure 7.15 one obtains the stimulation spectrum of trapped electrons corresponding to the TL peak at 340 K.

The same type of experiments has been performed with $\text{LiYSiO}_4:1\%\text{Ce}^{3+},0.2\%\text{Sm}^{3+}$ sample, and the results are shown in Figure 7.16. Since the low TL peak at 400 K does not fade at room temperature, the sample was treated with an infra-red laser for 10 min. After this action the TL peak at 400 K disappears, and curve b represents the photostimulation spectrum of traps corresponding to the TL peak at 500 K. The resulting curve "a-b" corresponding to the TL peak at 400 K represents a broad band with a maximum between 570-580 nm and resembles the stimulation curve of $\text{LiLuSiO}_4:1\%\text{Ce}^{3+},0.2\%\text{Sm}^{3+}$.

7.6.2 PSL of $\text{LiLuSiO}_4:\text{Ce}^{3+},\text{Sm}^{3+}$ and $\text{LiYSiO}_4:\text{Ce}^{3+},\text{Sm}^{3+}$

The previous results show that photostimulation of traps corresponding to the TL peaks at 340 and 400 K in $\text{LiLuSiO}_4:\text{Ce}^{3+},\text{Sm}^{3+}$ and $\text{LiYSiO}_4:\text{Ce}^{3+},\text{Sm}^{3+}$ is most efficient at about 580 nm, or with photons of higher energy. Due to separation problems of PSL and scattered stimulation light the use of shorter stimulation wavelength becomes difficult.

A combined PSL and TL technique was applied to investigate the differences between the PSL and TL response in the studied silicates. The procedure of this technique was already presented in [6.3.1]. As a photostimulation source a red diode was used with $\lambda=630$ nm and an output power 1 mW. The results are shown in Figure 7.17.

The results in Figure 7.17 indicate that only the low temperature peak can be stimulated by the photons with $\lambda\sim 630$ nm. The low temperature peak in residual TL curves stays at the same position. No decrease of integral PSL+TL signal was observed with the increase of stimulation time, in contrast with what has been observed in haloborates (Figure 6.2).

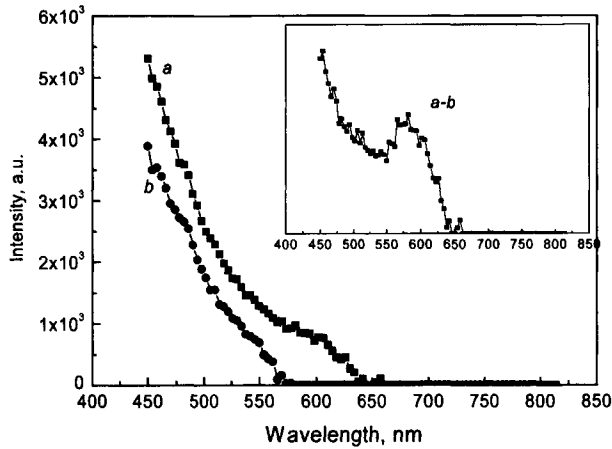


Figure 7.15: Photo stimulation spectra of $\text{LiLuSiO}_4:1\%\text{Ce}^{3+}, 0.2\%\text{Sm}^{3+}$ measured at $\lambda=390$ nm emission. Curve a) was measured just after irradiation. Curve b) was measured 2 hours after irradiation. In the inset a subtraction of curve b) from a) is presented. All the spectra are corrected for the intensity of the stimulating lamp.

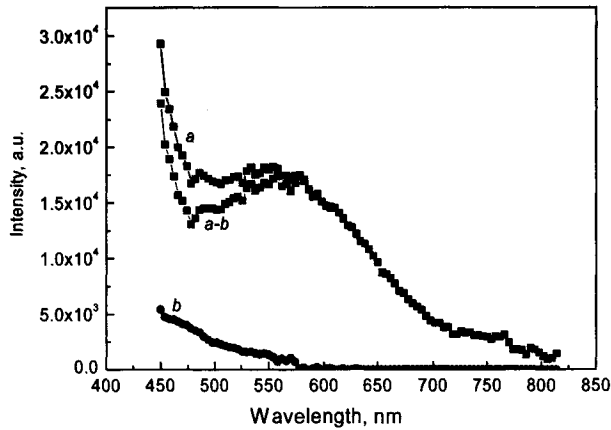


Figure 7.16: Photo stimulation spectra of $\text{LiYSiO}_4: 1\%\text{Ce}^3, 0.2\%\text{Sm}^{3+}$ measured at $\lambda=390$ nm emission. Curve a) was measured just after irradiation. Curve b) was measured after the sample had been illuminated with IR laser for 10 min. All the spectra are corrected for the intensity of the stimulating lamp.

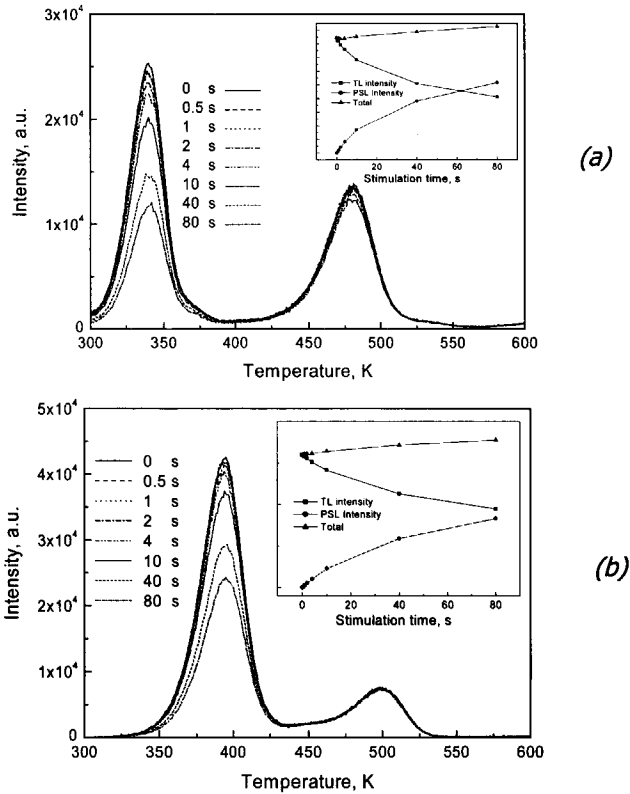


Figure 7.17: TL glow curves of β -irradiated $\text{LiLuSiO}_4:0.1\%\text{Ce}^{3+},1\%\text{Sm}^{3+}$ (a) and $\text{LiYSiO}_4:1\%\text{Ce}^{3+},0.2\%\text{Sm}^{3+}$ (b), which were recorded after photostimulation for different duration – from 0 to 100 s. Red diode ($\lambda \sim 632$ nm) with an output power ~ 1 mW was used as a stimulation source. The TL curves were recorded with a heating rate of 1 K/s. Irradiation was performed with $^{90}\text{Sr}/^{90}\text{Y}$ β -source. In the inset the integral intensity of the residual TL signal, PSL signal measured before TL measurements and the sum of both are plotted as a function of optical stimulation time are shown.

7.7 Discussions

The excitation spectrum of Ce^{3+} emission in Figure 7.4 shows a steep increase below a threshold at 171 nm, for both $\text{LiLuSiO}_4:\text{Ce}^{3+}$ and $\text{LiYSiO}_4:\text{Ce}^{3+}$ materials. We conclude that the threshold relates to the onset of fundamental absorption due to the SiO_4^{4-} silicate group. This threshold value is comparable with host absorption edges at 165 nm in $\text{Li}_2\text{CaSiO}_4$ and at 177 nm in $\text{Lu}_2\text{Si}_2\text{O}_7$ [16,17]. Therefore, silicate groups provide the bottom levels of the conduction band in the studied materials. If Y or Lu levels determine the bottom of the conduction band, then the host absorption edge in LiYSiO_4 is expected at slightly lower

energy than in LiLuSiO_4 . The slightly larger size of Y^{3+} ion as compared to Lu^{3+} reduces the negative Madelung potential at the Y-site leading to slightly reduced band gap.

The spin-orbit interaction splits the 5d configuration of free Ce^{3+} in two $^2\text{D}_{3/2}$ and $^2\text{D}_{5/2}$ levels. In a crystal on a site of low symmetry they are further split by the crystal field into five distinct 5d states [16]. Ce^{3+} centres in the studied silicates occupy a site with low C_1 symmetry. The first three bands in the excitation spectra in Figure 7.4 are certainly due to the Ce^{3+} 5d states. With increasing energy these states and bands are denoted as 5d_1 , 5d_2 and 5d_3 . The question arises where the other two 5d_4 and 5d_5 bands are located. For Ce^{3+} in a distorted octahedral coordination of 6 oxygen atoms at average distance of 232 pm splitting between the 5d_1 and 5d_5 of about 2.5 eV is expected [16,17].

This suggests that the 5d_4 and 5d_5 bands must be located in the shorter than 210 nm wavelength range. In the excitation spectra of Ce^{3+} emission shown in Figure 7.4, two broad bands at 200 and 180 nm are present that we attribute to the 5d_4 and 5d_5 bands. Decay curves of Ce^{3+} emission when excited in these bands are clearly not exponential, see Figure 7.5. A very fast component with a decay constant less than the radiative decay time of Ce^{3+} $5\text{d} \rightarrow 4\text{f}$ transitions is followed by a very slow component with a decay constant of several μs . These features indicate that the two 5d bands are located inside the conduction band. The $\text{d} \rightarrow \text{f}$ emission is thus quenched by auto-ionisation of the 5d electron to the conduction band leading to shortening of the excited Ce^{3+} life time and low intensity of these excitation bands. The presence of the slow component in the curve can be connected to re-trapping of the auto-ionised electron at longer time scale.

In Figure 7.18 the onset of fundamental absorption is drawn at 7.25 eV. At this energy bound electron hole pairs are excited near the excitonic absorption band of the host lattice. The bottom of the conduction band should be at somewhat higher energy. We conclude that 5d_4 and 5d_5 Ce^{3+} bands are above the bottom of conduction band and 5d_1 is below. 5d_3 and 5d_2 levels can also be inside the conduction band, but then the phonon relaxation from the 5d_3 and 5d_2 to 5d_1 should be much faster than auto-ionization.

In Figure 7.18 the 5d_4 band is positioned just above the conduction band and from that the Ce^{3+} ground state is at about 2 eV above the valence band. We also might have positioned the 5d_3 level close to the conduction band bottom leading to the Ce^{3+} ground state at about 4 eV. From this it follows that the ground 4f^1 state of Ce^{3+} locates above the valence band, however the exact position is still undetermined. The ground state of Tb^{3+} ions is expected to lie at about 0.83 eV lower than that of Ce^{3+} [18]. Despite the possible error, it is also located above the valence band.

The excitation spectrum of Eu^{3+} emission in Figure 7.7 is a superposition of two bands. We attributed the excitation band in Figure 7.7 fitted with Gaussian functions to the CT absorption bands of Eu^{3+} . The values of Eu^{3+} CT energies in LiLuSiO_4 and LiYSiO_4 were reported earlier by Blasse [11] at 5.34 eV (232 nm) and 5.30 eV (234 nm) respectively. However, our results reveal that CT absorption band of Eu^{3+} in LiLuSiO_4 and LiYSiO_4 are 5.61 eV (221 nm) and 5.51 eV (225 nm) respectively.

The initial stage in the CT process is a trivalent lanthanide ion in its ground state and an electron on a ligand ion, i.e. an electron on the top of the valence band [18]. In the case of oxides this is the 2p electron on oxygen. The final state, i.e., after CT is a divalent lanthanide in its ground state and a hole resized at the ligand ion. Therefore, the quantity of CT energy must determine the absolute position of the ground state of the divalent lanthanide relatively to the top of valence band.

It was argued in [18] that the CT band energy overestimates the energy of the RE^{2+} ground state by $\sim 0.5\text{--}1.0$ eV because of the relaxation that follows the CT. It was also estimated that the CT band energy underestimates the energy of the RE^{2+} ground state by $0.5\text{--}1.0$ eV because of the residual Coulomb interaction with the hole left in valence band. Therefore, the CT energy provides a good measure of RE^{2+} ground state with the error of the order of 0.5 eV. The data on CT energies of different lanthanides in a large number of compounds were collected by Dorenbos [18], and a general method to determine the CT energies of all the other lanthanides relative to that of Eu^{3+} was established.

Taking the known values of the band gap and assuming that CT energy is equalled to the energy difference between the Ln^{2+} ground state and the top of valence band, the energy level schemes of divalent lanthanides in LiLuSiO_4 or LiYSiO_4 can be drawn. The result is shown in Figure 7.18.

From Figure 7.18 two very important conclusions can be drawn. First, since the Ce^{2+} and Tb^{2+} ground states are inside the conduction band, Ce^{3+} and Tb^{3+} can not trap an electron. However, they can act as efficient hole traps, since the ground state of Ce^{3+} and Tb^{3+} are above the valence band. The second conclusion is that Eu^{3+} and Sm^{3+} are effective electron traps, since divalent states of these centres are well below the conduction band, and therefore stable.

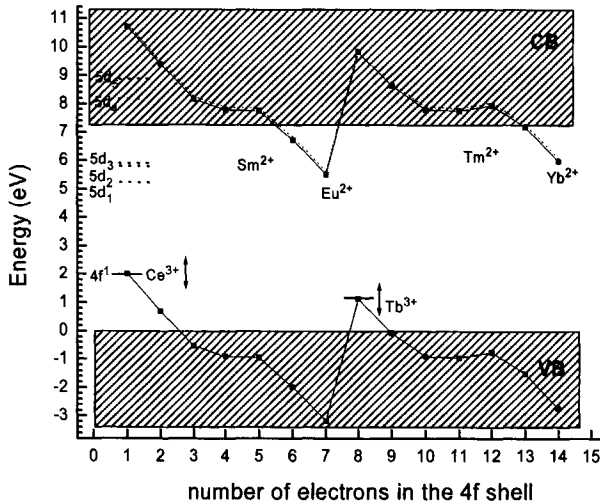


Figure 7.18: Schematic representation of the 4f ground state energy positions of lanthanides relative to the valence and conduction band in LiYSiO_4 (solid line) and LiLuSiO_4 (dotted line). The ground states of Eu^{2+} were estimated from the measured value of CT absorption energy. The extrapolation to other lanthanides was done according to [18]. The ground state of Ce^{3+} and Tb^{3+} ions is above the valence band, however the exact position is not known.

With the help of the level diagram it is possible to explain quantitatively the TL result.

LiLuSiO_4 doped with Ce^{3+} and/or Tb^{3+} shows an intense TL peak at 480. It is obvious to suggest that Ce^{3+} and Tb^{3+} ions are responsible for the hole trapping. For the charge balance a

residual electron is trapped somewhere in the lattice. The suggestion that Tb^{3+} and Ce^{3+} ions are involved in hole trapping, and no other lattice defects, is confirmed by the absence of the TL peak at 480 K in the $LiLuSiO_4:Sm^{3+}$ sample. As it follows from Figure 7.18, the Sm^{3+} ion can not be a stable hole trap. Thus, in the absence of Ce^{3+} or Tb^{3+} impurities in $LiLuSiO_4$ there are no possibilities for a hole trapping. We attributed the origin of the peak at 480 K to the release of an electron trapped at an intrinsic defect of the host and recombination at Ce^{4+} or Tb^{4+} .

In $LiLuSiO_4$ doubly doped with Ce and Sm an intense strong peak appears at 340 or 400 K in TL glow curves (Figures 7.10 and 7.11). We conclude that co-doping with Sm^{3+} ions provides an additional channel for electron trapping. After electron capture, divalent samarium is created, and its ground state is located below the conduction band. Upon thermal stimulation the electrons released from Sm^{2+} recombine with Ce^{4+} centres. The resulting Ce^{3+} luminescence gives rise to the TL peak at 340 or 400 K.

According to the considerations above, the Ce and Sm concentration determines the number of available hole and electron trapping centres. The increase of Sm^{3+} centres can lead to multiple re-trapping of the electron released from Sm^{2+} upon stimulation. Therefore, the low temperature TL peak of the sample with low content of Sm^{3+} must follow an ideal Randall-Wilkins first-order kinetics glow curve. Indeed, as it can be seen from Figure 7.12 for the $LiLuSiO_4:1\%Ce^{3+},0.1\%Sm^{3+}$ and $LiLuSiO_4:1\%Ce^{3+},0.2\%Sm^{3+}$ samples the low temperature peak resembles first-order asymmetrical shape, and for the sample with higher content of Sm^{3+} the shape becomes more like second-order kinetics. The intensity ratio between the TL peaks at 340 and 480 K in the samples with 1 mol.% of Sm^{3+} is about two times higher than that in the sample with 0.1 mol.% of Sm^{3+} . The position of the TL peaks does not depend on the activator concentration, however the intensity changes unpredictably with Ce and Sm content.

A mechanism similar to the hole trapping by Ce^{3+} or Tb^{3+} , is the ionisation of Ce^{3+} or Tb^{3+} , i.e., removing of an electron by photon excitation. In both cases, the final state is a tetravalent Ce^{4+} or Tb^{4+} centre. The threshold of the trap-filling curve in Figure 7.13 of the Ce^{3+} doped sample is at lower photon energy than of that with Tb^{3+} doping. Therefore ionisation of Tb^{3+} ions requires photons of higher energy than for Ce^{3+} , if ionisation is defined as the energy required for an electronic transition from the ground state of a rare earth ion to the conduction band. This is in agreement with the fact that the ground state of Tb^{3+} ions at about 0.83 eV below that of Ce^{3+} [18].

In the compound doubly doped with Ce^{3+} and Sm^{3+} the trap filling spectra in Figures 7.15 and 7.16 for low and high temperature TL peaks are the same. Therefore, filling of both the traps related to lattice defects and Sm^{3+} should occur via the same mechanism. This agrees with the mechanism that in both cases the trapped electron originates from Ce^{3+} .

The nature of the intrinsic lattice defects responsible for electron trapping and the high temperature peak was further investigated. We suspected that an oxygen vacancy plays the role of electron trap. An atmosphere was used during synthesis to prevent formation of tetravalent Ce. One expects that additional firing of the material in oxygen atmosphere will lead to a higher content of Ce^{4+} and lower content of oxygen vacancies. We annealed $LiLuSiO_4:Ce^{3+},Sm^{3+}$ and $LiYSiO_4:Ce^{3+},Sm^{3+}$ at 900 °C for 4 hours. As a result the high temperature peak disappears and the intensity of the low temperature peak was halved, see Figure 7.19. The absence of the high temperature peak is attributed to a complete absence of

oxygen vacancies. The decrease of the low TL peak can be caused by partial reduction of Ce^{3+} into Ce^{4+} , i.e. decrease of the number of available luminescent and hole trapping centres.

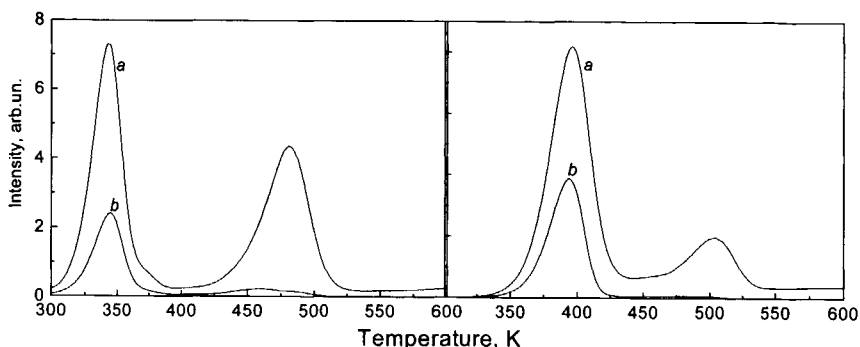


Figure 7.19: On the left: the TL glow curves of the $\text{LiLuSiO}_4:0.1\%\text{Ce}^3,1\%\text{Sm}^3$ sample recorded before (a) and after (b) annealing in air at 900°C for 4 hours. On the right: TL glow curves of the $\text{LiYSiO}_4:1\%\text{Ce}^3,0.2\%\text{Sm}^3$ sample recorded before (a) and after (b) annealing in air at 900°C for 4 hours. The samples have the same size. Heating rate 1K/s .

The TL mechanism related to the appearance of the low temperature peak was also investigated more in detail. From the results leading to the scheme in Figure 7.18, we find that the energy difference between the Sm^{2+} ground state and the bottom of the conduction band in LiLuSiO_4 is 0.48 eV against 0.57 eV in LiYSiO_4 . This implies that the samarium electron trap in LiYSiO_4 is $\Delta E_0 \sim 0.1\text{ eV}$ deeper than in LiLuSiO_4 . The prediction that samarium is a more stable electron trap in LiLuSiO_4 than in LiYSiO_4 is confirmed by the TL measurements in Figures 7.10 and 7.11. The low temperature peak is shifted by $\Delta T = 60\text{ K}$ to higher temperature in LiYSiO_4 .

The low temperature TL peaks of LiLuSiO_4 and LiYSiO_4 were fitted assuming Randall-Wilkins first order kinetics (equation 3.1). The two parameters, i.e. activation energy and frequency factor can be varied during the fit. Since the nature of the recombination mechanism is the same in $\text{LiLuSiO}_4:\text{Ce}^{3+},\text{Sm}^{3+}$ and $\text{LiYSiO}_4:\text{Ce}^{3+},\text{Sm}^{3+}$ we assumed the same frequency factor for both compounds. The results of the fitting procedure yield $s=10^8\text{ s}^{-1}$ and $E_T = 0.82\text{ eV}$ for $\text{LiLuSiO}_4:\text{Ce}^{3+},\text{Sm}^{3+}$ and $E_T = 0.95\text{ eV}$ for $\text{LiYSiO}_4:\text{Ce}^{3+},\text{Sm}^{3+}$.

In thermoluminescence, the release of charge occurs via excited states with unknown energies. Therefore, the value of the activation energy parameter itself used in thermoluminescence theory is difficult to be compared with other experimentally derived parameters. However, a difference between the E_T values in the two compounds gives the relative position of the traps, assuming the same nature of the TL mechanism in both materials. Thus the depth of samarium electron trap in LiYSiO_4 is $\Delta E_T \sim 0.1\text{ eV}$ deeper than in LiLuSiO_4 . It is seen, that the values ΔE_T and ΔE_0 are very close to each other, which is a good proof that recombination upon thermal stimulation occurs via release of an electron to conduction band.

The results show, that the trap depth difference of 0.1 eV has a significant effect on the TL peak position and consequently on fading characteristics. This can explain the absence of a TL signal in $\text{LiLuSiO}_4:\text{Ce}^{3+},\text{Eu}^{3+}$ and $\text{LiYSiO}_4:\text{Ce}^{3+},\text{Eu}^{3+}$. The position of Eu^{2+} is at ~ 1.2

eV lower energy than that of Sm^{2+} , see Figure 7.18. So, Eu^{3+} produces too deep an electron trap, and can not lead to storage effect.

Upon photostimulation two possibilities should be considered: the $4f \rightarrow 5d$ transitions in Sm^{2+} with further ionisation and ionisation of an electron directly to the conduction band. In the photostimulation spectrum the band at about 580 nm, which is at a much higher energy than the difference between the Sm^{2+} ground state and the bottom of the conduction band. The band at 580 nm is attributed to Sm^{2+} $4f \rightarrow 5d$ transitions. Thus the recombination mechanism upon photo stimulation occurs via excitation of Sm^{2+} to the 5d state with further ionisation and subsequent electron capture by Ce^{4+} .

7.8 Remarks

Other compounds with double $\text{Ce}^{3+}, \text{Sm}^{3+}$ co-doping

We have tested several other compounds, like $\text{YBO}_3: \text{Ce}^{3+}, \text{Sm}^{3+}$, $\text{Li}_6\text{Y}(\text{BO}_3)_3: \text{Ce}^{3+}, \text{Sm}^{3+}$ and $\text{Li}_2\text{CaSiO}_4: \text{Ce}^{3+}, \text{Sm}^{3+}$ on the presence of storage effects. Upon X-ray excitation Ce^{3+} and Sm^{3+} centres give rise to emission spectra, and no Sm^{2+} emission can be observed. According to [11,20] the CT absorption energies of Eu^{3+} in YBO_3 and $\text{Li}_6\text{Y}(\text{BO}_3)_3$ are 5.43 eV and 4.81 eV respectively. The band-gap of YBO_3 and $\text{Li}_6\text{Y}(\text{BO}_3)_3$ is about ~ 7 eV [21]. According to calculations done in [21] the conduction band in YBO_3 is formed by B (2p) orbitals.

Based on the considerations developed in this chapter, the ground states of Sm^{2+} in YBO_3 and in $\text{Li}_6\text{Y}(\text{BO}_3)_3$ are located at 0.58 eV and 1.06 eV below the conduction band respectively. Thus Sm^{3+} ions in these materials are expected to be stable electron traps. However, no TL signal and PSL signals upon 630 and 830 nm stimulation of irradiated $\text{YBO}_3: \text{Ce}^{3+}, \text{Sm}^{3+}$, $\text{Li}_6\text{Y}(\text{BO}_3)_3: \text{Ce}^{3+}, \text{Sm}^{3+}$ have been detected.

Even a small difference of 0.1 eV in the position of the trap depth has a significant influence on storage properties. We did not perform measurements to determine the position of CT energies as well as band gap energy for YBO_3 and $\text{Li}_6\text{Y}(\text{BO}_3)_3$. The materials doped with other potential electron trapping impurities – Tm^{3+} or Yb^{3+} should be studied for the presence of storage effects. Thus, more investigations are needed to bring clarity to this point.

In $\text{Li}_2\text{CaSiO}_4: \text{Ce}^{3+}, \text{Sm}^{3+}$ intense TL signal has been detected. However, the origin of this was established to be not due to $\text{Ce}^{3+}, \text{Sm}^{3+}$ pairs. No PSL signal signals upon 630 and 830 nm stimulation have been detected in this sample. The absence of storage effect due to $\text{Ce}^{3+}, \text{Sm}^{3+}$ pairs can be explained by a low stability of Ce^{4+} centres at a divalent Ca site.

7.9 Quantitative comparison with commercial storage phosphors

7.9.1 Comparison of $\text{LiLuSiO}_4: 1\% \text{Ce}^{3+}, 0.2\% \text{Sm}^{3+}$ with Gd-IP after cold neutron irradiation and read-out with commercial IP scanner

The conditions for the experiments are exactly the same as described in [6.2.2]. $\text{LiLuSiO}_4: \text{Ce}, \text{Sm}$ powder samples were put in a holder; a circular wells of 200 μm depth in an

aluminium plate (Figure 6.1). As a reference a commercial Fuji Neutron Image Plate (Fuji - NIP) containing a mixture of $\text{BaFBr}:\text{Eu}^{2+}$ and Gd_2O_3 was used. Samples were irradiated for 30 s with a neutron flux of about $10^8 \text{ n}\cdot\text{cm}^{-2}\cdot\text{s}^{-1}$. During irradiation the transmission of 7.6 \AA neutrons through the samples was measured. Only 19% of neutrons are absorbed in the $200 \mu\text{m}$ of $\text{LiLuSiO}_4:\text{Ce}, \text{Sm}$ phosphor layer, whereas Fuji NIP absorbs 100%.

The read-out phase was carried out 15 minutes after irradiation. The low temperature TL peak of $\text{LiLuSiO}_4:\text{Ce}, \text{Sm}$ fades by about a factor of 2 in this time interval (Figure 7.10). The Image Plate scanner is equipped with a He-Ne laser ($\lambda=635 \text{ nm}$) as a stimulation source and a band pass filter ($\lambda\sim 390 \text{ nm}$) in front of the PMT for separation of scattered laser light. The emission spectrum of $\text{LiLuSiO}_4:\text{Ce}, \text{Sm}$ has its maximum at 390 nm (Figure 7.1). Therefore read-out parameters are about optimal for $\text{LiLuSiO}_4:\text{Ce}, \text{Sm}$.

The measured PSL yield of the silicate sample is 250 counts per pixel against 40000 for the Fuji NIP. The amount of ^6Li in the sample is about 6%. When using a sample with 100% of ^6Li enrichment the PSL yield can be increased at most by a factor of 16 [6.4.2]. Thus it can reach 4000 counts per pixel. This would still be 10 times smaller than the PSL yield of commercial NIP.

The drawback of $\text{LiLuSiO}_4:\text{Ce}, \text{Sm}$ is the fast fading at room temperature. The use of $\text{LiYSiO}_4:\text{Ce}, \text{Sm}$ can overcome this problem.

7.9.2 Comparison of $\text{LiLuSiO}_4:\text{Ce}^{3+}, \text{Sm}^{3+}$ and $\text{LiYSiO}_4:\text{Ce}^{3+}, \text{Sm}^{3+}$ with $\text{BaFBr}:\text{Eu}^{2+}$ after β -irradiation and read-out with Risø-PSL single-grain reader

The stimulation spectra of $\text{BaFBr}:\text{Eu}^{2+}$ and $\text{LiYSiO}_4:\text{Ce}^{3+}, \text{Sm}^{3+}$ phosphors are compared in Figure 7.20. They were measured under similar conditions and after the same radiation dose. The aim to perform these measurements was to compare the stimulation efficiencies obtained from stimulation spectra with the values of PSL yields. It is seen in Figure 7.20 that stimulation efficiency of $\text{LiYSiO}_4:\text{Ce}^{3+}, \text{Sm}^{3+}$ is about 20 times smaller than that of $\text{BaFBr}:\text{Eu}^{2+}$ stimulating at about 550 nm .

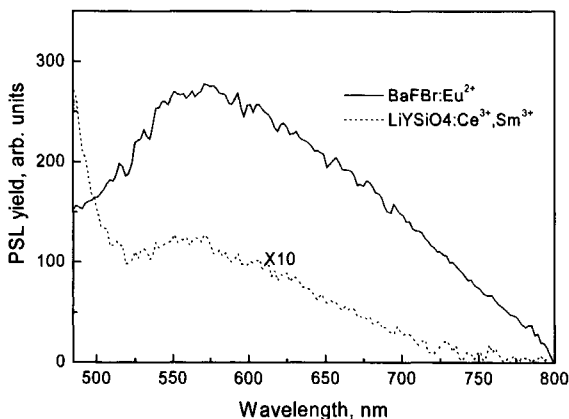


Figure 7.20: PSL stimulation spectra of $\text{LiYSiO}_4:1\%\text{Ce}^{3+}, 0.1\%\text{Sm}^{3+}$ (dotted curve) measured at $\lambda=350 \text{ nm}$ emission and of $\text{BaFBr}:\text{Eu}^{2+}$ (solid curve) measured at $\lambda=390 \text{ nm}$ emission. The spectra were corrected for the intensity of the xenon lamp. Sample size and irradiation doses are the same for both samples.

The read-out of storage phosphors with the help of the Risø-PSL single-grain reader was already described in Chapter 6. The read out parameters of this system are equally optimal for BaFBr:Eu²⁺ as for the studied silicates. The typical PSL curves of BaFBr:Eu²⁺, LiLuSiO₄:Ce³⁺, Sm³⁺ and LiYSiO₄:Ce³⁺, Sm³⁺ upon continuous laser stimulation after β-irradiation are shown in Figure 7.21. The measurements were carried out 15 minutes after irradiation. The results show that the PSL yield of the silicates in the first 20 ms of laser stimulation is about 30 times smaller than that of BaFBr:Eu²⁺.

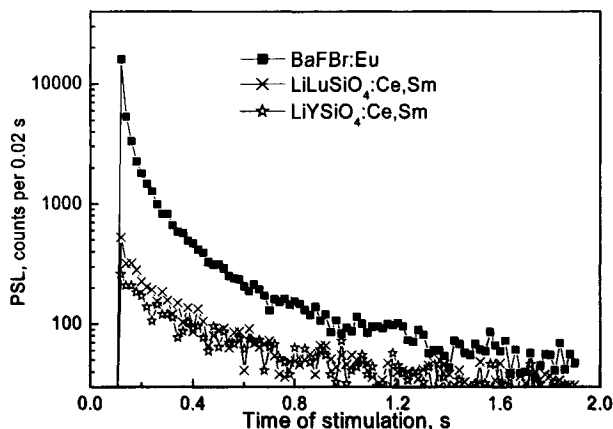


Figure 7.21: The PSL curves of BaFBr:Eu²⁺, LiLuSiO₄:1%Ce³⁺,0.2%Sm³⁺ and LiYSiO₄:1%Ce³⁺, 0.1%Sm³⁺ under continuous stimulation by means of Nd:YVO₄ laser ($\lambda=532$ nm). Laser power is 10 mW and the beam diameter approximately 120 μm on the sample surface.

7.10 Conclusions

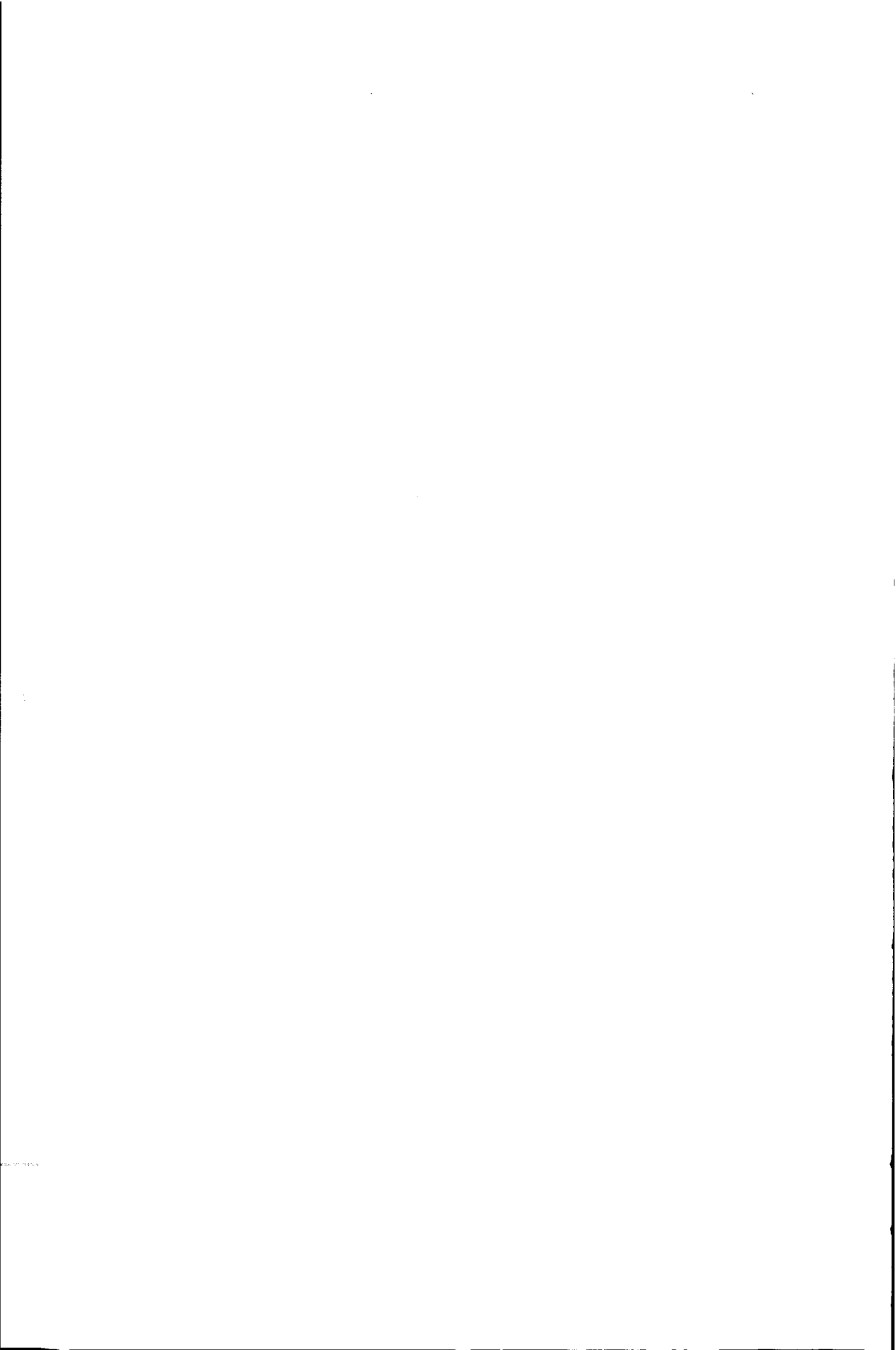
The possibility of controlled creation of electron and hole-trapping centres by activation of an inorganic material with appropriate Ln³⁺ ions was demonstrated. The depth of the electron trap can be derived from charge transfer absorption energy of any lanthanide and the value of the band gap energy. As an example, the storage and recombination mechanism in lithium lutetium and lithium yttrium silicates doped with Ce³⁺ and Sm³⁺ was investigated. The derived values of electron trap depth energies obtained from spectroscopic and thermoluminescence experiments are in a good agreement. It was established that changing of the electron trap energy by 0.1 eV has a significant effect on TL peak position and fading properties.

Concerning practical application, the PSL yield of the silicates can be optimised by using starting materials with 100% of ⁶Li enrichment. In that case, the PSL yield upon neutron

irradiation of the silicates can reach up to one tenth of that of the commercial Gd-IP. Note that the quantitative results were obtained for the test-grown samples, i.e. by optimising the synthesis procedure, better performance of silicates can be achieved.

References

- [1] Chakrabarti K., Mathur V. K. and Rhodes J. F., *J. Appl. Phys.* **64** (1988) 1363-1366
- [2] Tamura Y. and Shibukawa A., *Jpn. J. Appl. Phys.* **32** (1993) 3187-3196
- [3] Tamura Y., *Jpn. J. Appl. Phys.* **33** (1994) 4640-4646
- [4] Zhang J. G., Eklund P C and Hua Z L, *J. Mater. Res.* **7** (2) (1992) 411-417
- [5] Zhi yi H., Yong-sheng W. and Li S., *J. Phys. Condens. Matter* **13** (2001) 3665-3675
- [6] Wu J., Newman D. and Viney I., *J. Lumin.*, **99** (2001) 237-245
- [7] Chakrabarti K., Mathur V. K. and Thomas L. A., *J. Appl. Phys.* **65** (1989) 2021-2023
- [8] Keller S. P., Mapes J. E. and Cheroff G., *Phys. Rev.* **108** (3) (1957) 663-676
- [9] Keller S. P. and Pettit G. D., *Phys. Rev.* **111** (6) (1958) 1533-1539
- [10] Robins L. and Tuchman J. A., *Phys. Rev. B* **57** (19) 12094-12103
- [11] Blasse G. and Brill A., *J. Inorg. Nucl. Chem.*, **29** (1967) 2231-2241
- [12] Nakayama S. and Sakamoto M., *J. Ceram. Soc. Jpn.*, **100** (6) (1992) 867-71
- [13] El'yashevich M. A., *Spectra of rare-earth elements*, Gosudarstvennoe izdatel'stvo tehnikeskoi literatury, Moscow, 1953 (in Russian)
- [14] Shannon R. D., *Acta Cryst. A* **32** (1976) 751-767
- [15] Dorenbos P., *J. Lumin.* **91**(3-4) (2000) 155-76
- [16] Dorenbos P., *Phys. Rev. B.* **64** (12) (2001) 125117/1-12
- [17] Dorenbos P., Pierron L, Dinca L et al., *J. Phys.: Condens. Matter* **15** (3) (2003) 511-520
- [18] Dorenbos P., *J. Phys.: Condens. Matter* **15**, 8417 (2003).
- [19] Chen R. and McKeever S. W. S., *Theory of thermoluminescence and related phenomena*, World Scientific Publishing, 1997
- [20] van Pieterse L., *Charge transfer and $4^n-4^{n-1}5d$ luminescence of lanthanide ions*, PhD thesis, Universitet Utrecht, 2001
- [21] Dotsenko V. P., *Borates of elements in I-II groups: synthesis – structure – spectroscopic properties*, dissertation for the 2nd habilitation, Odessa 2002



Concluding remarks

The most common and general approach to the development of new X-ray storage phosphors is a search among alkali-halide materials activated with different rare earth or mercury-like ions. The scenario of the storage mechanism is a well-known pair mechanism: upon X-irradiation F centres are generated as electron traps and the activator itself acts as a complementary hole trap.

The routine way to optimise neutron storage phosphors is to take one of the known X-ray phosphors and mix it with a neutron converter. In spite of the large number of activities in this field the mixture of $\text{BaFBr:Eu}^{2+} \times \text{Gd}_2\text{O}_3$ is essentially the only one applied.

The goal to find a neutron storage phosphor among borates or lithium containing materials, competitive with $\text{BaFBr:Eu}^{2+} \times \text{Gd}_2\text{O}_3$ mixture represents a formidable problem. In the beginning we assumed the following storage mechanism in borates. It was suggested that the storage effect in borates could be realised only at a certain structure of the anion borate skeleton, namely a network of BO_3 and BO_4 groups. A similar anion skeleton structure exists in efficient TLD materials, like $\text{MgB}_2\text{O}_4:\text{Dy}^{3+}$ or $\text{Li}_2\text{B}_4\text{O}_7:\text{Cu}$. Unfortunately, these materials exhibit only TL signals. The observation of PSL is obscured by the location of the emissions in the long wavelength region.

We also supposed that if the basis of the anion sublattice consists of isolated BO_3 triangles (this is the case of $\text{Li}_6\text{Y}(\text{BO}_3)_3$ or YBO_3 and in series of other borates investigated by M. Knitel [1]) or a rigid network of BO_4 tetrahedra (like in SrB_4O_7), the observation of storage effect at any activator is impossible. We became more convinced of this hypothesis, after establishing the absence of storage effect in $\text{SrB}_4\text{O}_7:\text{Ce}^{3+}$, $\text{Sr}_2\text{B}_5\text{O}_{15}:\text{Ce}^{3+}$, $\text{SrB}_6\text{O}_{10}:\text{Ce}^{3+}$, $\text{Li}_6\text{Y}(\text{BO}_3)_3:\text{Ce}^{3+}$ and $\text{YBO}_3:\text{Ce}^{3+}$ materials, which exhibit efficient prompt luminescence.

A systematic study of TL properties of a number of non-isostructural borates with BO_3 and BO_4 groups is needed in order to provide a definitive answer to the question of the influence of a borate network structure on the storage properties. Due to the difficulty of the synthesis procedure of borates and the absence of predictability of results the decision was made to stop activities in that direction.

The borate network of $\text{Sr}(\text{Ca})_2\text{B}_5\text{O}_9\text{Br}(\text{Cl})$ haloborates studied in this work represents two BO_3 triangles connected with three BO_4 tetrahedra. Therefore, according to our previous suggestion the observed storage effect in haloborates is related to the structure of the borate skeleton. From more detailed investigations of the storage mechanism in haloborates presented in chapter 5, we came to the conclusion that the room temperature stable defects are not due to charge trapping in the borate network. The storage effects in haloborates are due to the presence of halogen anions, as was quite consistently proven. Therefore, again F-centres take part in the storage process.

The number of matrixes that include halogen ions and borate groups in their crystal structure is limited. There is probably only one structure left - $\text{Li}_4\text{B}_7\text{O}_{12}\text{Cl}$, which activated with a mercury-like ion, might exhibit storage effect. However, we did not manage to synthesise this material or to get it from elsewhere. Therefore our further activities were concentrated on search and development of yet another storage mechanism.

The first idea to use a phosphor, doubly doped with lanthanide ions comes from the late 60s. Storage properties of sulphides doped with Eu^{2+} and Sm^{3+} ions have been intensively studied. However, except for sulphides and $\text{Y}_2\text{Si}_2\text{O}_5:\text{Ce}^{3+},\text{Sm}^{3+}$ no compounds doubly doped with lanthanides and exhibiting desired storage properties have been found.

The results and discussion presented in chapter 7 on LiLu(Y)SiO_4 doped with Ce^{3+} and Sm^{3+} confirms that this pair could be used for creation of electron and hole trapping centres in inorganic materials. Moreover, the parameters of electron trapping centres such as the activation energy can be estimated and even predicted, if the position of the charge transfer absorption band of any lanthanide and the band gap of the material are known.

As for application, it was shown that haloborates enriched with ^{10}B can compete with $\text{BaFBr}:\text{Eu}^{2+}\times\text{Gd}_2\text{O}_3$ when utilised in environments with a high gamma-background. The presented lithium silicates could be promising not only for neutron but also for X-ray detection. The results of the study of the lithium silicates are most important for further development of neutron and X-ray storage phosphors for various applications.

As a conclusion, the most success for future development of storage phosphors is anticipated in compounds doubly doped with lanthanide ions. The matrix could be chosen depending on the application requirements.

Reference

- [1] Knitel M. J., Dorenbos P., van Eijk C. W. E., Nucl. Instr. And Meth. A 443 (2000) 364-374
"Photoluminescence, and scintillation/thermoluminescence yields of several Ce^{3+} and Eu^{2+} activated borates"

Summary

The aim of the work presented in this thesis is the development and improvement of neutron storage phosphors with low sensitivity to γ -ray background. In order to reach the main goal the following problems had to be solved:

- i. To define the optimal parameters of neutron storage phosphors.
- ii. The search and selection of a host matrix and activators for potential neutron storage phosphors. This step required the in-depth study of the known physical processes occurring in scintillators and storage phosphors.
- iii. Investigation of luminescence and storage properties of chosen phosphors, elucidation of the nature of luminescence centres and radiation induced defects. Further optimisation of storage phosphor performance based on obtained results and developed hypotheses.

The requirements for neutron storage phosphors are established in Chapter 2. The known X-ray storage phosphors, their properties and performances are reviewed. Special attention is devoted to the elucidation of the storage mechanism, using existing data on the nature of electron and hole trapping centres. Despite the large number of publications on this topic the trapping and recombination mechanisms occurring in most storage phosphors are still not clear.

The techniques used to study the storage properties of materials are described in Chapter 3. In Table 1, the materials studied or just checked on the presence of storage effect are listed.

Table 1: *Materials studied in this work. In the last column the yields of X-ray excited luminescence, thermoluminescence (TL) or photostimulated luminescence (PSL) are indicated as "high" or "low". The integral yield of X-ray excited luminescence is defined as "high" if it is of the same order of magnitude as that of BaF₂. The integral TL or PSL yield is defined as "low" if it is lower than 1% from that of BaFBr:Eu²⁺. The materials indicated in bold are described in separate chapters of the thesis. Others were just checked on the presence of a TL or PSL signal.*

Compound	Activator	X-ray/TL/PSL "+" – high "–" – low
YBO ₃	Ce ³⁺ ; Ce ³⁺ , Sm ³⁺	+ / - / -
SrB ₄ O ₇	Ce ³⁺ ; Ce ³⁺ , Sm ^{2+/3+}	+ / - / -
Sr ₂ B ₂ O ₅	Ce ³⁺	+ / - / -
SrB ₆ O ₁₀	Ce ³⁺ ; Ce ³⁺ , Sm ^{2+/3+}	+ / - / -
SrBPO ₅	Ce ³⁺ , Ce ³⁺ , Na ⁺	+ / - / -
Sr(Ca)₂B₅O₉Br(Cl)	Ce³⁺; Ce³⁺, Na⁺	+ / + / +
Li ₆ Y(BO ₃) ₃	Ce ³⁺ ; Ce ³⁺ , Sm ³⁺	+ / - / -
Li ₂ CaSiO ₄	Ce ³⁺ ; Ce ³⁺ , Sm ³⁺	+ / + / -
LiLnSiO₄, Ln=Y, Lu	Ce³⁺; Ce³⁺, Sm³⁺	+ / + / +

Three chapters of the thesis are devoted to the haloborate phosphors doped with Ce^{3+} .

In Chapter 4 we performed an extended spectroscopic study of series of $\text{Sr}_2\text{B}_5\text{O}_9\text{X}:\text{Ce}^{3+},\text{A}^+$ ($\text{X}=\text{Cl},\text{Br}$, $\text{A}=\text{Na}^+,\text{K}^+$) phosphors by means of optical and EPR techniques.

The two strontium sites in $\text{Sr}_2\text{B}_5\text{O}_9\text{Br}$ have very similar anion coordination polyhedra. Using optical spectroscopy we could not distinguish two Ce^{3+} sites. At the same time the EPR lines from Ce^{3+} centres in two crystallographic positions are very well distinguishable.

In the luminescence spectra two types of Ce^{3+} centres have been detected in $\text{Sr}_2\text{B}_5\text{O}_9(\text{Br},\text{Cl}):\text{Ce}^{3+}$ and they can be associated with isolated Ce_1^{3+} and charge compensated Ce_2^{3+} centres. Based on EPR results we concluded that several kinds of charge compensation defects are responsible for the Ce_2^{3+} emission. Only one type of Ce^{3+} emission centre was detected in the samples co-doped with Na^+ or K^+ . Optical and EPR characteristics of this centre coincide with isolated Ce_1^{3+} centres. The thermoluminescence properties of these materials and the contributions of different Ce^{3+} centres in the TL emission spectra are discussed.

Chapter 5 is dedicated to elucidation of the nature of the trapping centres in haloborates. The EPR study of irradiated pure $\text{Sr}_2\text{B}_5\text{O}_9\text{Br}$ revealed a room-temperature stable defect, which was attributed to an O_{Br}^- centre. The EPR signal from $\text{F}(\text{Br}^-)$ centres can be observed at temperatures below 120 K. The $1s \rightarrow 2p$ transitions of these $\text{F}(\text{Br}^-)$ centres cause the optical absorption band at 560 nm. The optical absorption band at 365 nm was attributed to O^- centres. Thus electron and hole trapping in pure $\text{Sr}_2\text{B}_5\text{O}_9\text{Br}$ occurs in V_{Br} and $\text{O}_{\text{Br}}^{2-}$ aggregates, which are created during the synthesis.

The EPR and radiation induced absorption measurements on Ce^{3+} doped $\text{Sr}_2\text{B}_5\text{O}_9\text{Br}$ revealed the same defects as in pure material. It is very likely that the same defects take part in the thermoluminescence corresponding to the high temperature peak. The nature of charge trapping defects in haloborates seems to be the same as in the well known stoichiometric $\text{BaFBr}:\text{Eu}^{2+}$ storage phosphor.

In Chapter 6 the suitability for practical application was checked of haloborate phosphors with the general formula $\text{M}_2\text{B}_5\text{O}_9\text{X}:\text{Ce}^{3+}$ ($\text{M}=\text{Sr}$ or Ca ; $\text{X}=\text{Br}$ or Cl). The TL and PSL properties were studied. The results of this study led to the conclusion that the $\text{Ca}_2\text{B}_5\text{O}_9\text{Cl}:\text{Ce}^{3+}, \text{Na}^+$ compound is the most promising of the whole studied series for detection of thermal neutrons, with reduced sensitivity to gamma rays, since it has the lowest Z_{eff} number and, at the same time, a relatively high PSL yield.

The read-out parameters, i.e. stimulation wavelength and band-pass filter of commercial image plate scanners are highly inefficient for haloborates. When optimised read-out parameters are implied, the PSL light yield of $\text{Ca}_2^{10}\text{B}_5\text{O}_9\text{Cl}:\text{Ce},\text{Na}$ (1%) after neutron irradiation with $\lambda \sim 1.8 \text{ \AA}$ is 16 times less than that of $\text{BaFBr}:\text{Eu}^{2+},\text{xGd}_2\text{O}_3$. However the neutron to gamma discrimination of $\text{Ca}_2^{10}\text{B}_5\text{O}_9\text{Cl}:\text{Ce},\text{Na}$ (1%) is almost an order of magnitude better than that of $\text{BaFBr}:\text{Eu}^{2+},\text{xGd}_2\text{O}_3$. Therefore haloborate phosphors could be more attractive when utilised in environments with a high gamma -background.

The part of the work devoted to the understanding and model development of the storage mechanism based on double doping of inorganic compounds with two types of lanthanide ions is presented in Chapter 7.

A strong storage effect has been observed in $\text{LiLnSiO}_4:\text{Ce}^{3+},\text{Sm}^{3+}$, $\text{Ln}=\text{Y},\text{Lu}$. We presented strong arguments that in the studied materials the Ce^{3+} ions play the role of hole trapping defects and the Sm^{3+} ions of electron trapping centres. Additionally, oxygen vacancies are also involved in electron trapping, however they can be removed by appropriate thermal treatment.

We showed that the depth of the electron trap associated with the Ln^{3+} impurity could be derived from the charge transfer absorption energy of any lanthanide and the value of the band gap energy. From the spectroscopic studies we established that the samarium electron trap in LiYSiO_4 is located 0.1 eV deeper relative to the bottom of conduction band than in LiLuSiO_4 .

During thermal stimulation in irradiated $\text{LiLnSiO}_4:\text{Ce}^{3+},\text{Sm}^{3+}$, $\text{Ln}=\text{Y},\text{Lu}$ an electron of Sm^{2+} is released to the lower energy states of the conduction band, formed by SiO_4 , and migrates further to Ce^{4+} centres. This causes the TL peaks at 340 K in $\text{LiLuSiO}_4:\text{Ce}^{3+},\text{Sm}^{3+}$ and at 400 K in $\text{LiYSiO}_4:\text{Ce}^{3+},\text{Sm}^{3+}$. Thus, the difference in the trap depth energy of 0.1 eV has a significant effect on the TL peak position ($\Delta T \sim 60$ K) and consequently on fading characteristics.

Concerning the practical application, the PSL yield of silicates can be optimised by using starting materials with 100% of ^6Li enrichment. In this case, the PSL yield upon neutron irradiation of silicates can reach up to one tenth of that of a commercial Gd-IP. This is a first study of silicates with double rare earth doping and improvements can be expected when further synthesis optimisation be performed. The $\text{LiYSiO}_4:\text{Ce}^{3+},\text{Sm}^{3+}$ material seems to be more suitable for application because of its very slow fading.

Future developments of storage phosphors should be performed using double co-doping with lanthanide ions. The matrix could be chosen depending on the application requirements.



Samenvatting

Het doel van het werk dat in dit proefschrift wordt beschreven is de ontwikkeling en de verbetering van neutron-opslagfosforen met een lage gevoeligheid voor γ -achtergrondstraling. Om dit doel te bereiken moesten de volgende problemen worden opgelost:

- ◆ Het bepalen van de optimale parameters van neutron opslagfosforen.
- ◆ Het onderzoek en de selectie van een gastheermatrix en activatoren voor potentiële neutron-opslagfosforen. Deze stap vereiste een diepgaande studie van de fysische processen die in scintillatoren en opslagfosforen voorkomen.
- ◆ Onderzoek van luminescentie en opslageigenschappen van gekozen fosforen, opheldering van de aard van luminescentiecentra en door straling veroorzaakte materiaal-defecten. De verdere optimalisering van de prestaties van de opslagfosforen wordt gebaseerd op de verkregen resultaten en ontwikkelde hypothesen.

De eisen ten aanzien van neutron-opslagfosforen worden bepaald in Hoofdstuk 2. De eigenschappen en prestaties van bekende röntgenopslagfosforen worden samengevat. Speciale aandacht is geschonken aan de opheldering van het opslagmechanisme en het gebruik van de bestaande gegevens over de aard van de elektronen en gaten-vangst centra. Ondanks het grote aantal publicaties over dit onderwerp, zijn de opslag en recombinatiemechanismen die in de meeste opslagfosforen voorkomen nog niet duidelijk.

Tabel 1: Materialen die in dit werk zijn bestudeerd. In de laatste kolom zijn de opbrengsten van direct met röntgenstraling opgewekte luminescentie, thermoluminescentie (TL) of met fotonen gestimuleerde luminescentie (PSL) vermeld als "hoog" of "laag". De integrale opbrengst van met röntgenstraling opgewekte luminescentie is aangeduid als "hoog" indien deze van dezelfde grootte orde is als die van BaF_2 . De integrale opbrengst van TL of PSL wordt gedefinieerd als "laag" indien deze lager is dan 1% van die van BaFBr:Eu^{2+} . De materialen die in vette letters vermeld, worden beschreven in afzonderlijke hoofdstukken van dit proefschrift. De andere materialen werden enkel gecontroleerd op de aanwezigheid van een TL of PSL signaal.

Verbinding	Activator	Röntgen/TL/PSL “+” – hoog ; “-” – laag
YBO ₃	Ce ³⁺ ; Ce ³⁺ , Sm ³⁺	+ / - / -
SrB ₄ O ₇	Ce ³⁺ ; Ce ³⁺ , Sm ^{2+/3+}	+ / - / -
Sr ₂ B ₂ O ₅	Ce ³⁺	+ / - / -
SrB ₆ O ₁₀	Ce ³⁺ ; Ce ³⁺ , Sm ^{2+/3+}	+ / - / -
SrBPO ₅	Ce ³⁺ , Ce ³⁺ , Na ⁺	+ / - / -
Sr(Ca)₂B₅O₉Br(Cl)	Ce³⁺; Ce³⁺, Na⁺	+ / + / +
Li ₆ Y(BO ₃) ₃	Ce ³⁺ ; Ce ³⁺ , Sm ³⁺	+ / - / -
Li ₂ CaSiO ₄	Ce ³⁺ ; Ce ³⁺ , Sm ³⁺	+ / + / -
LiLnSiO₄, Ln=Y, Lu	Ce³⁺; Ce³⁺, Sm³⁺	+ / + / +

De technieken die worden gebruikt om de opslageigenschappen van materialen te bestuderen worden beschreven in Hoofdstuk 3. In Tabel 1, worden de materialen die op de aanwezigheid van opslageffect zijn bestudeerd of enkel zijn gecontroleerd, vermeld.

Drie hoofdstukken van dit proefschrift zijn gewijd aan de haloboraatefosforen gedoteerd met Ce^{3+} ionen.

In Hoofdstuk 4 beschrijven we een uitgebreide spectroscopische studie van de reeks van $Sr_2B_5O_9X:Ce^{3+}$, A^+ ($X=Cl, Br$, $A=Na^+$, K^+) fosforen door middel van optische en EPR technieken.

De twee strontiumplaatsen in $Sr_2B_5O_9Br$ hebben gelijksoortige anioncoördinatie in de vorm van regelmatige veelvlakken. Gebruik makend van optische spectroscopie konden wij de twee Ce^{3+} plaatsen niet onderscheiden. Tezeldertijd waren de EPR lijnen van de Ce^{3+} centra in de twee kristallografische posities zeer goed te onderscheiden.

In de luminescentiespectra zijn twee types van Ce^{3+} centra ontdekt in $Sr_2B_5O_9(Br, Cl):Ce^{3+}$; zij kunnen met geïsoleerde Ce_1^{3+} en lading-gecompenseerde Ce_2^{3+} centra worden geassocieerd. Gebaseerd op EPR resultaten besloten wij dat verscheidene soorten van de ladingscompensatie defecten verantwoordelijk zijn voor Ce_2^{3+} emissie. Slechts één type van Ce^{3+} emissiecentrum werd gedetecteerd in de samples met Na^+ of K^+ . De optische en EPR kenmerken van dit centrum vallen samen met die van geïsoleerde Ce_1^{3+} centra. De thermoluminescentie eigenschappen van deze materialen en de bijdragen van de verschillende Ce^{3+} centra in TL emissiespectra worden besproken.

Hoofdstuk 5 is gewijd aan opheldering van de aard van de vangst centra in de haloboraten. De EPR studie van bestraald zuiver $Sr_2B_5O_9Br$ openbaarde een stabiel defect bij kamer-temperatuur, dat werd toegeschreven aan een O_{Br^-} centrum. Het EPR signaal van $F(Br^-)$ centra kan worden waargenomen bij temperaturen onder 120 K. De $1s \rightarrow 2p$ overgangen van deze $F(Br^-)$ centra veroorzaken de optische absorptieband bij 560 nm. De optische absorptieband bij 365 nm werd toegeschreven aan O^- centra. We concluderen dat elektronen en gaten in zuiver $Sr_2B_5O_9Br$ worden ingevangen in $V_{Br^-} - O_{Br^{2-}}$ complexen, welke tijdens de synthese zijn gecreëerd. EPR en de door straling geïnduceerde absorptiometingen aan Ce^{3+} gedoteerd $Sr_2B_5O_9Br$ toonden dezelfde defecten als in het zuivere materiaal. Het is zeer waarschijnlijk dat dezelfde defecten aan de thermoluminescentie deelnemen die aan de piek bij hoge temperatuur beantwoordt. De aard van de ladingsvangst-defecten in haloboraten lijkt hetzelfde als die in het bekende stoichiometrische $BaFBr:Eu^{2+}$ opslagfosfor.

In Hoofdstuk 6 werd de geschiktheid voor praktische toepassing gecontroleerd van haloboraatfosforen met de algemene formule $M_2B_5O_9X:Ce^{3+}$ ($M=Sr$ of Ca ; $X=Br$ of Cl). De TL en PSL eigenschappen werden bestudeerd. De resultaten van deze studie leidden tot de conclusie dat de $Ca_2B_5O_9Cl:Ce^{3+}$, Na^+ samenstelling het veelbelovendst is van de hele bestudeerde reeks voor detectie van thermische neutronen met verminderde gevoeligheid voor γ -stralen, vanwege het laagste Z_{eff} getal en tegelijkertijd een vrij hoge PSL opbrengst.

De uitleesparameters, d.w.z. de stimulatie golflengte en het doorlaatfilter van de commerciële scanners van de beeldplaat zijn zeer inefficiënt voor haloboraten. Wanneer geoptimaliseerde uitleesparameters worden gebruikt is het PSL signaal van $Ca_2^{10}B_5O_9Cl:Ce, Na$ (1%) voor neutronenbestraling bij $\lambda \sim 1.8 \text{ \AA}$ 16 keer kleiner dan dat van $BaFBr:Eu^{2+} \times Gd_2O_3$. Nochtans is het onderscheidend vermogen tussen neutronen en γ -straling

van $\text{Ca}_2^{10}\text{B}_5\text{O}_9\text{Cl}:\text{Ce},\text{Na}$ (1%) bijna een grootte orde beter dan dat van $\text{BaFBr}:\text{Eu}^{2+}x\text{Gd}_2\text{O}_3$. Daarom zou het haloboraat fosfor aantrekkelijker kunnen zijn voor gebruik in een omgeving met hoge γ -achtergrond.

Het deel dat is gewijd aan het begrip en de modelontwikkeling van het opslagmechanisme dat bij dotering van anorganische materialen met twee typen van lanthanide ionen optreedt, wordt besproken in Hoofdstuk 7.

Een sterk opslageffect is waargenomen in $\text{LiLnSiO}_4:\text{Ce}^{3+},\text{Sm}^{3+}$, $\text{Ln}=\text{Y},\text{Lu}$. Wij vonden sterke argumenten dat Ce^{3+} -ionen de rol van gatenvangstcentra spelen en Sm^{3+} -ionen de elektronenvangst centra zijn in de bestudeerde materialen. Daarnaast zijn ook zuurstof vacatures betrokken bij elektronenvangstcentra. Deze kunnen eventueel door een geschikte thermische behandeling worden verwijderd.

Wij hebben aangetoond dat de diepte van het elektronvangstcentrum verbonden aan Ln^{3+} ionen, kan worden afgeleid uit de absorptieenergie van de ladingsoverdracht van de lanthaniden en de breedte van de verboden band. Uit de spectroscopische studies hebben wij vastgesteld dat de samarium niveau in LiYSiO_4 0.1 eV dieper t.o.v. de bodem van de geleidingsband ligt vergeleken met LiLuSiO_4 .

Tijdens thermische stimulatie van bestraald $\text{LiLnSiO}_4:\text{Ce}^{3+},\text{Sm}^{3+}$, $\text{Ln}=\text{Y},\text{Lu}$ wordt een elektron van uit Sm^{2+} afgegeven aan de lagere energietoestanden van de geleidingsband, gevormd door SiO_4 groepen, en het migreert verder naar Ce^{4+} centra. Dit veroorzaakt een TL piek bij 340 K in $\text{LiLuSiO}_4:\text{Ce}^{3+},\text{Sm}^{3+}$ en bij 400 K in $\text{LiYSiO}_4:\text{Ce}^{3+},\text{Sm}^{3+}$. Het verschil in de energie van de valdiepte van 0.1 eV heeft dus een significant effect op de TL piekpositie ($\Delta T \sim 60$ K) en daardoor ook op de "fading".

Betreffende de praktische toepassing kan de PSL opbrengst van silicaten worden geoptimaliseerd door startmaterialen met 100% verrijkt ^6Li te gebruiken. In dat geval zal de PSL opbrengst van silicaten eentiende van dat van commercieel $\text{BaFBr}x\text{Gd}_2\text{O}_3$ bedragen. Dit is een eerste studie van silicaten met dubbele doping met Ln ionen. Verbeteringen kunnen worden verwacht wanneer een verdere syntheseoptimalisering wordt uitgevoerd. $\text{LiYSiO}_4:\text{Ce}^{3+},\text{Sm}^{3+}$ lijkt geschikter voor toepassing te zijn omdat dit materiaal een zeer langzame "fading" heeft.

De toekomstige ontwikkelingen van opslagfosforen zouden moeten worden gericht op gebruikmaking van materialen die dubbel gedoteerd zijn met lanthanide ionen. De matrix kan afhankelijk van de toepassingsvereisten worden gekozen.



List of publications

1. Storage phosphors for thermal neutron detection // Sidorenko A.V., Bos A.J.J., Dorenbos P., Le Masson N.J.M., van Eijk C.W.E., Rodnyi P.A., Berezovskaya I.V., Dotsenko V.P., NIM-A **486** (1-2) (2002) 160-163, *Chapter 2*
2. Luminescence and thermoluminescence of $\text{Sr}_2\text{B}_5\text{O}_9\text{X}:\text{Ce}^{3+}, \text{A}^+$ (X = Cl, Br, A= Na^+, K^+) phosphors // Sidorenko A.V., Bos A.J.J., Dorenbos P., van Eijk C.W.E., Rodnyi P.A., Berezovskaya I.V., Dotsenko V.P., J. Phys. Cond. Matter **15** (20) (2003) 3471-3480, *Chapter 4*
3. Study of ESR spectra of Ce^{3+} ions in polycrystalline $\text{Sr}_2\text{B}_5\text{O}_9\text{Br}$ // Sidorenko A.V., van Eijk C.W.E., Rodnyi P.A., Guillot-Noel O., Gourier D., Phys. Solid State **45** (9) (2003) 1676-1678, *Chapter 4*
4. Radiation induced defects in $\text{Sr}_2\text{B}_5\text{O}_9\text{Br}:\text{Ce}^{3+}$ storage phosphor // Sidorenko A.V., Bos A.J.J., Dorenbos P., van Eijk C.W.E., Rodnyi P.A., Berezovskaya I.V., Dotsenko V.P., Guillot-Noel O., Gourier D., J. Phys. Cond. Matter **16** (2004) 4131-4138, *Chapter 5*
5. Storage properties of Ce^{3+} doped haloborate phosphors enriched with ^{10}B isotope // Sidorenko A.V., Bos A.J.J., Dorenbos P., van Eijk C.W.E., Rodnyi P.A., Berezovskaya I.V., Dotsenko V.P., Popov A.I., J. of Appl. Physics **95** (11) (2004) 7898-7902, *Chapter 6*
6. Storage effect in $\text{LiRESiO}_4:\text{Ce}^{3+}, \text{Sm}^{3+}$, RE=Y, Lu phosphor // Sidorenko A.V., Bos A.J.J., Dorenbos P., van Eijk C.W.E., Kahn-Harari A., Rodnyi P.A. and Viana B., NIM-A, (2003) accepted, *Chapter 7*
7. Charge trapping mechanism in $\text{LiLnSiO}_4:\text{Ce}^{3+}, \text{Sm}^{3+}$, Ln=Y or Lu storage phosphor // Sidorenko A.V., Dorenbos P., Bos A.J.J., van Eijk C.W.E., Rodnyi P.A., Phys. Rev. B, (2004) submitted, *Chapter 7*
8. Small-size pulsed X-ray source for measurements of scintillator decay time constants // Rodnyi P.A., Mikhlin S.B., Mishin A.N., Sidorenko A.V., IEEE Transactions on Nuclear Science **48** (6) pt. 2 (2001) 2340-3
9. Valence states and luminescence properties of ytterbium ions in strontium haloborates // Dotsenko V.P., Berezovskaya I.V., Efryushina N.P., Pyrogenko P.V., Rodnyi P.A., van Eijk C.W.E., Sidorenko A.V., J. Solid State Chem. **166** (2002) 271



Curriculum Vitae

The author of this thesis was born in a beautiful northern city in the north-west of Russia on the 24th of June 1977. In 1992 he passed a competitive entrance examination to a specialised physics-mathematical school, where he had been obliged to perceive the basics of physics and mathematics in an extremely intensive way during two years. After obtaining a high school diploma in 1994 he continued his study of physics at St.-Petersburg State Technical University. He was lucky to perform his graduation work in the collaboration between the Experimental Nuclear Physics group of his home University and the Radiation Technology group of Delft Technical University.

Directly after obtaining his masters degree in June 2000, he moved to the Netherlands and started working as a PhD-student in the Interfaculty Reactor Institute of Delft Technical University, under supervision of prof.dr.ir. C.W.E. van Eijk. The research principally consisted of in-depth study of physical processes occurring in irradiated borate and silicate solid solutions using various spectroscopic techniques. The results of the research are presented in the book you are enjoying reading.



Acknowledgements

Four years in the Netherlands are behind me. It's surprisingly how fast time flights and how many things it gives us to be understood and to be done. I'm writing the last page of this book, and now it's a y time to look behind, look to the past to say great thank to all people who were close to me over all this time.

First of all, I want to thank my promoter C.W.E. van Eijk for giving me the possibility to perform the PhD study in his research group and his care for the project and me.

My hearty thanks to my first direct research supervisor in Delft during my Master thesis and afterwards my co-promoter Pieter Dorenbos, for his guiding support and his inexhaustible ideas concerning experiments and physics.

I am heartily grateful to my direct supervisor in Russia, Prof. Piotr Aleksandrovich Rodnyi, for sharing his almost infinite knowledge of physics with me.

I would like to express a gratitude to two persons: Dr. Irina Berezovskaya and Prof. Pavel Dotsenko for the synthesis of the borates. Without their work this thesis would not have existed. Also, special thanks to Andrée Kahn-Harari for her assistance and guidance on my chemical synthesis of silicates in Paris.

My gratefulness to Dr. Adrie Bos for his assistance, constructive critics and supervisory tact.

No experimental work would be successful without skilled technical support. Thanks to Johan de Haas for providing it and always being patient, even if I had many questions and requests.

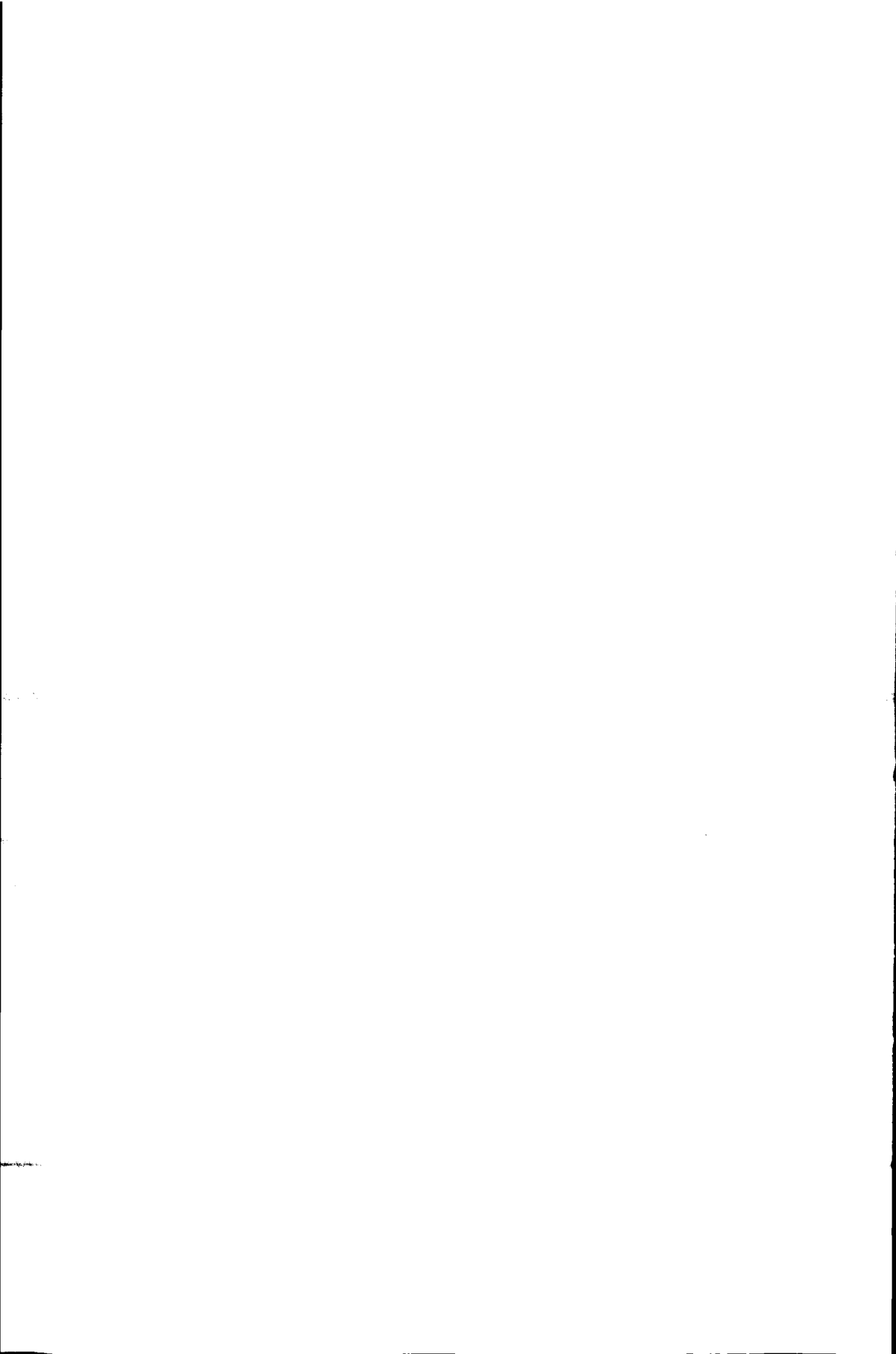
Thanks to Nicolas for being a great colleague and friend. Mirko, Ivan, Marnix and Jan: I wish you all the best and a lot of success for the remaining parts of your PhD studies.

Thanks to all people, who crossed over my life in the Netherlands.

Finally I am infinitely thankful to my parents, my brother, and my sweetheart wife Yulia for their wisdom, patience and love.











Delft University Press